A DEHUMIDIFIER FOR DEHUMIDIFICATION SYSTEM OF THAILAND CLIMATE CONDITION COOPERATED DESICCANT COATING TECHNICAL WITH THERMOELECTRIC

CHANCHIRA CHANNOY

A Thesis Submitted to the Graduate School of Naresuan University
in Partial Fulfillment of the Requirements
for the Doctor of Philosophy in Applied Physics
2021

A DEHUMIDIFIER FOR DEHUMIDIFICATION SYSTEM OF THAILAND CLIMATE CONDITION COOPERATED DESICCANT COATING TECHNICAL WITH THERMOELECTRIC

CHANCHIRA CHANNOY

A Thesis Submitted to the Graduate School of Naresuan University
in Partial Fulfillment of the Requirements
for the Doctor of Philosophy in Applied Physics
2021

Thesis entitled "A dehumidifier for dehumidification system of Thailand climate condition cooperated desiccant coating technical with thermoelectric"
By CHANCHIRA CHANNOY

has been approved by the Graduate School as partial fulfillment of the requirements

for the Doctor of Philosophy in Applied Physics of Naresuan University

Oral Defense Committee

.... Chair
(Professor Surapong Chirarattananon, Ph.D.)

.... Advisor
(Assistant Professor Somchai Maneewan, Ph.D.)

.... Internal Examiner
(Assistant Professor Chantana Punlek, Ph.D.)

.... External Examiner
(Assistant Professor Pattana Rakkwamsuk, Ph.D.)

.... External Examiner
(Professor Tanakorn Wongwuttanasatian, Ph.D.)

Approved

....
(Associate Professor Krongkarn Chootip, Ph.D.)

Dean of the Graduate School

Title	A DEHUMIDIFIER FOR DEHUMIDIFICATION SYSTEM OF THAILAND CLIMATE CONDITION COOPERATED DESICCANT COATING TECHNICAL WITH THERMOELECTRIC
Author	CHANCHIRA CHANNOY
Advisor	Assistant Professor Somchai Maneewan, Ph.D.
Academic Paper	Ph.D. Dissertation in Applied Physics, Naresuan University, 2021
Keywords	Mesoporous silica, Composite desiccant, Silica gel, Thermoelectric dehumidifier, Adsorption kinetics, Adsorption isotherms, Nitrogen sorption

ABSTRACT

Bagasse ash is an agricultural waste product of sugar cane and a natural silica source that is highly available, safe to humans, and cost-effective. We choose to use bagasse ash as the primary material in this study. The objectives of this study were to prepare mesoporous silica from bagasse ash (MS-BA). Nitrogen sorption findings revealed that the specific surface area and pore volume of prepared MS-BA increased with increasing NaOH concentration, peaking at 2.0 N and decreasing afterward. The specific surface area, pore volume, and pore size of the MS-BA with 2.0 N NaOH concentration are 525 $m^2 g^{-1}$, 0.61 $cm^3 g^{-1}$, and 15 nm, respectively. The obtained MS-BA particles were spherical-shaped nanoparticles ranging 50 to 100 nm in diameter.

Aqueous salt solutions (LiCl) were impregnated into a porous host matrix to create composite desiccant materials (silica gel). The authors of this paper fabricated and analyzed composite desiccant-coated aluminum sheets (DCAS) with varying LiCl mass concentrations. Nitrogen sorption results revealed that the Brunauer-Emmett-Teller (BET) surface area and pore volume of the composite desiccant-coated aluminum sheets decreased. Furthermore, composite DCAS had lower nitrogen sorption than silica gel-coated aluminum sheets (SGCAS). According to the results, the composite DCAS had the highest thermal conductivity, measuring 6.1 $Wm^{-1} K^{-1}$, doubling that of the SGCAS. For evaluating sorption kinetics, the linear driving force model (LDF) was used, and composite DCAS showed greater dynamic sorption quantities and sorption rate coefficients than SGCAS. Furthermore, three different moisture sorption isotherm models were used to fit the experimental results: the Brunauer-Emmett-Teller (BET) model, the Guggenheim-Anderson-Boer (GAB) model, and the double log polynomial (DLP) model. The DLP model was shown to be the best model for predicting the moisture sorption isotherms of DCAS. Additionally, the composite desiccant-coated heat sink (DCHS) of the thermoelectric dehumidifier (TED) was evaluated and compared to silica gel in terms of dehumidification capacity. According to the findings, the outlet air humidity ratio of the composite DCHS reached a minimum of 10.23 g kg^{-1}, and the dehumidification capacity was 0.117 kg h^{-1} when the input electrical voltage was kept at 9 V.

The purpose of this study was to investigate the application of thermoelectric (TE) technology to a dehumidifying device as a method of decreasing the heat load on conventional vapor-compression refrigeration systems. The experimental prototype of the thermoelectric dehumidifier (TED) was constructed and its working performance was evaluated experimentally with and without a composite coated heat sink. Experiments were conducted to investigate the effects of input electrical voltage on the TE modules and the air flow rate through the heat sink. The cooling capacity increased with the increase in electrical voltage, reaching a maximum of 100.78 W and the corresponding COP is 0.79 at 12 V. On the other hand, the cooling capacity, decreased as the air flow rate increased. At all electrical voltages supplied to the TE modules, the dehumidification capacity of the TED with the composite desiccant was higher than without the composite desiccant (34.44%). As a result, it is anticipated that the suggested TED with the composite desiccant concept will contribute to the reduction in room humidity.

ACKNOWLEDGEMENTS

I would like to express the deepest gratitude to my advisor, Assistant Professor Somchai Maneewan, Ph.D, and Professor Surapong Chirarattananon, Ph.D for his initial idea, guidance, and encouragement which enable me to carry out my study successfully. I consider it as a great opportunity to do my doctoral program under his advice and to learn from his research expertise.

My sincere gratitude also goes to my thesis committee, Professor Tanakorn Wongwuttanasatian, Ph.D, Assistant Professor Pattana Rakkwamsuk, Ph.D and Assistant Professor Chantana Punlek, Ph.D for their helpful advice, comments and suggestions.

My profound thanks to Department of Physics, Faculty of Science, Naresuan University for being warmest places to study since the researcher studied a Bachelor’s degree and Doctoral degree here. I feel love and commitment with here. I would like to thank Science Lab Center and Miss Thanita Sutthatang for XRD and BET analysis, Mr. Seangphet Boonpang and Miss Prakaithip Kitikhunfor from for SEM analysis for their assistance in the part of instrument. In addition, I gratefully acknowledge the bachelor of food science and nutrition, faculty of science and technology, Prince of Songkla University, for the facilities to perform sorption isotherm analysis.

I would like to acknowledge the Science Achievement Scholarships of the International Research Network Program (IRN) under project number IRN5703PHDW01, The Thailand Research Fund (TRF) to Miss Chanchira Channoy all financial support during this study.

Finally, I would like to thank my family for their love and their understanding. They have been constantly providing me with encouragement, enjoyment during my life and enabled me to complete this thesis.

CHANCHIRA CHANNOY

TABLE OF CONTENTS

Page

LIST OF TABLES

Page

LIST OF FIGURES

Page

CHAPTER I

INTRODUCTION

The rationale for the study

Indoor comfort plays a significant role in human activities in both residential areas and commercial places. Humidity control plays a vital role in providing better comfort conditions; because sticky or humid air is not pleasing and can cause molds, common colds, and skin allergies (1). Similarly, indoor areas have small openings that allow dust particles, toxic gases, and dust mites to enter and serve as shoddy air quality (2, 3). Other than openings, there is often an obnoxious smell in closed spaces, which is quite disturbing. Thus, control over the indoors' relative humidity has vast potential for providing gratifying comfort conditions and better air quality.

Thailand is located in a tropical region and is subject to a hot and humid climate. The ambient temperature range is between 25 to 35 ^{o}C, and the relative humidity is high for the whole year. Air-conditioning for thermal comfort has reached saturation in large commercial buildings. For residential buildings in urban and suburban areas, air-conditioning is also widely used. When air-conditioning is used, it contributes 70% to total electricity consumption in a household, which is a cause for concern because air-conditioning is highly energy-intensive. Electricity is generated at a very high rate. Since the fuel cost has been increasing, we must find a way to reduce electricity use or conserve the energy used for air-conditioning to achieve thermal comfort.

Most Thai offices are currently air-conditioned using forced-air systems, and cooling is solely based on convection. Human comfort is the main objective of an air-conditioning system. Traditionally, air-conditioning systems are designed conventionally; i.e., air conditioning is used to perform thermal space conditioning and maintain indoor air quality. Fans that cool transport air consumes part of the energy used to cool buildings. This energy heats the conditioned air and therefore adds to the internal thermal cooling load. The Department of Alternative Energy Development and Efficiency (DEDE) of Thailand collected information from 1995 to

2001 from more than 1,600 samples of an energy audit at commercial buildings. The data reveals that of the electricity used in a building, 60% is used for air-conditioning systems, 20% for lighting, and 20% for other usages. The breakdown of electricity used in office buildings is shown in **Table 1**. Because a significant share of the energy used in buildings is for the air conditioning system, developing alternative low-energy means of achieving thermal comfort is desirable.

Table 1 Breakdown of electricity use in a typical office building in Thailand

Element end-use	**Economic low energy design**		**Typical range**
	kWh/m²/Y	**Percent**	**kWh/m²/Y**
Cooling and dehumidification	114	60	110-160
Lighting	38	20	25-50
Ventilation	10	5	8-15
Office equipment	10	5	1-5
Lifts	11	6	10-20
Auxiliary	17	4	6-20
Total	190	100	160-270

In a tropical climate, air-conditioning (AC) systems remove sensible and latent heat from building spaces. Conventionally, mechanical dehumidification uses a cooling coil to cool down the ambient air below its dew-point temperature to release its moisture. However, a cooling coil of an air-conditioning (AC) system can handle the sensible and latent loads by condensation dehumidification. Still, the system's coefficient of performance (COP) is limited to very low. It is energy-inefficient to use this system for dehumidification.

Nowadays, there are many solutions to this problem, such as using a rotating desiccant wheel to absorb moisture from the air. A reheating process is needed to raise the overcooled air temperature before supplying air into the building space. The novel desiccant dehumidification method has been proposed. Various types of desiccant dehumidifiers, such as liquid desiccant and solid desiccant, have been developed and widely adopted for dehumidification systems. For using desiccant, the problem is that moisture has to be extracted from the air desiccant. When used for a while, however, the temperature will rise. Therefore, the use of thermoelectric to control the air. The resulting air will have a lower temperature and humidity by dehumidifying the air through the thermoelectric's cold side. Moreover, use the hot side of the thermoelectric to regenerate the desiccant so that the desiccant can resume. During the last two decades, thermoelectric devices have been widely investigated.

Dehumidifiers can facilitate humidity control and prevent these multiple causes of discomfort (4-6). In recent years, dehumidifiers are also developed from moist atmospheric air, known as atmospheric water generators (7, 8). At present, most of the dehumidifiers are refrigerant-based, working on the principle of the vapor compression cycle, which has a tremendous negative impact on the green and clean environment as they use an extensive amount of chlorofluorocarbons (CFCs) or hydrochlorofluorocarbons (HCFCs) (9, 10). Further, they are pretty heavy, noisy, and have strong compressor vibration (11). Thermoelectric dehumidifiers (TEDs) can be a viable alternative to these refrigerant-based dehumidifiers and cope with all these glitches as they are environment-friendly, quiet, and compact. The most unbeatable characteristic of thermoelectric in dehumidifiers is portability (12). That is because of thermoelectric modules (TEMs), which are very light in weight and compact in size compared to other techniques (13, 14). In thermoelectric dehumidifier (TED), the dehumidification process is noticeably clear since the moist atmospheric air directly interacts with the cold side of TEMs for its dehumidification. Hence, providing a smooth and clean operation of the dehumidification process.

On the other hand, another primary application of thermoelectric dehumidifiers (TEDs) is water generators (15, 16). TEMs in TED provide it the applicability for small-scale portable water generation from the atmosphere in high humid areas. Drinking water scarcity is inevitable in humid regions that could adopt TED for usage in multiple applications (17-19). These water generators can be solar-assisted devices and work as self-sustainable portable water generators (20). The TEMs and heat sink fans used in TED can be directly powered by DC power input. Thus, the system can be quickly and directly associated with solar power. Hence, other than solar-assisted water generators, general thermoelectric dehumidifiers (TEDs) have also been introduced to solar energy (21). However, the only thing that sets TED back in the current scenario is thermoelectric technology's inefficient performance over vapor compression. They have a low coefficient of performance (COP) compared to the traditional vapor compression-based dehumidifier (22). Therefore, they are considered a viable option only for small and portable dehumidifiers and not large-scale applications.

Thermoelectric technology is a viable option for various applications in the form of thermoelectric coolers (TECs) and thermoelectric generators (TEGs), which has been keenly well-reviewed for its major applications (13, 23-28). Likewise, various recent TED studies are performed in the current scenario for their practical applicability (29-34). Furthermore, studies are also committed to improving depending on the parameters of TED (35-39). In desiccant-based dehumidifiers, moisture-absorbing materials are used. In the adsorption-based desiccant, the moisture content from the moist air passed through the desiccants is trapped on its surface, and the dry air is obtained. The most commonly used desiccant for this process is silica gel (40). In the case of absorption desiccants, liquid desiccant such as LiCl is used. The dry air obtained in the cases of desiccants has a higher temperature value; hence it needs to be passed through a cooling element or cooling agent before supplying to the thermal comfort sensible range (41).

Recently, a new family of composite sorbents known as Selective Water Sorbents (SWSS) or Novel Composites Salt inside Porous Matrix (CSPMs) was introduced for dehumidification systems, which are two-phase systems composed of a porous host matrix (silica gels, activated alumina, porous carbons, zeolite, expanded vermiculite, etc.) and a hygroscopic substance (LiCl (42), $CaCl_2$ (43), LiBr (44), $MgCl_2$ (45), $MgSO_4$, $Ca(NO_3)_2$ (46), Na_2S, $SrBr_2$, $LiNO_3$ (47), $MgSO_4$, etc.). Due to their physical structure, the materials take an intermediate position between solid adsorbents and pure hygroscopic salts and are organized to demonstrate both systems' best features. Ge et al. (48) developed compound desiccant (silica gel–haloids) was adopted in an inter-cooling rotary wheel dehumidification system to remove part of adsorption heat. Results revealed that the system could be driven by low regeneration temperature (60 to 90 ^{o}C) with the coefficient of performance (COP) higher than 1.0.

Jeong et al. (49) examined the performance of four dehumidification systems using previously validated simulation models. The result showed that a batch-type system with an internal heat exchanger could be driven at the lowest temperature of about 33 ^{o}C. Hu et al. (50) compared dehumidification performance of fin-tube heat exchangers coated by silica gel and silica gel-lithium chloride composite desiccant. The experiment results showed that composite desiccant has a higher dehumidification capacity than silica gel (increased by 107%) under the same experimental conditions. Chua (51) studied three kinds of composite desiccants-silica gel-calcium chloride, silica gel-lithium chloride, and silica gel-polyvinyl alcohol. The composite desiccant materials combine more silica gel and halides or polymers and exhibit high moisture removal capacity. High regeneration capacity results have indicated that the moisture removal capacity, regeneration rates, and the associated pressure drops of composite desiccants outperformed pure silica gel by at least 11%.

This study proposes and investigates experimentally under natural hot and humid climate conditions a thermoelectric dehumidifier for the dehumidification system of Thailand's climate cooperated composite desiccant (LiCl+silica gel) desiccant coating. The system was installed at a laboratory building at Naresuan University, Phitsanulok, Thailand. A series of dehumidifiers can continuously work in dehumidification and regeneration at the same time. The hot side of the thermoelectric works the regeneration process, and the cool side of the thermoelectric works the dehumidification process. The performance of the system is also discussed.

Objectives of this study

The objectives of this research are as follow:

1. To prepared the mesoporous silica using sodium silicate by the alkali extraction method. The effect of sodium hydroxide (NaOH) concentration on synthesized mesoporous silica's microstructure, morphology, and pore characteristics was investigated.

2. To determine the effect of using lithium chloride (LiCl) on the performance of moisture absorption.

3. To improve the physical and mechanical properties of a composite desiccant such as texture property, thermal conductivity, sorption kinetics, and moisture sorption isotherms.

4. To build a thermoelectric dehumidifier (TED) for Thailand's climate, a composite desiccant coating technical collaborated with thermoelectric.

5. To investigate the effects of the flow rate and the ventilation air temperature on thermal comfort

6. To study the possibility and optimization of a thermoelectric dehumidifier (TED) such as electric voltage and current produce thermoelectric temperature, fan unit relation, and addicting fresh air.

The hypothesis of the study

1. The mesoporous silica was prepared using sodium silicate by the alkali extraction method to reduce the mesoporous silica preparation cost by using bagasse ash as the silica source. Bagasse ash conversion to mesoporous silica exemplifies the concept of "waste to treasure." Due to its low cost and simplicity of synthesis, mesoporous silica from bagasse ash is valuable.

2. Lithium chloride (LiCl) as a component of composite desiccant can improve the physical properties of this desiccant and consequently enhance the performance of moisture adsorption.

3. The thermoelectric dehumidifier (TED) as a component of thermoelectric, composite desiccant, heat sink, fans, and monitoring sensor can decrease the heat transfer from the outside of buildings to the interior, and thereby reduce the cooling load of air conditioning equipment.

Scope of the study

1. The mesoporous silica was prepared using sodium silicate by the alkali extraction method. The effect of sodium hydroxide (NaOH) concentration on synthesized mesoporous silica's microstructure, morphology, and pore characteristics was investigated.

2. Develop the physical and mechanical properties of composite desiccant (lithium chloride (LiCl) with silica gel).

3. Examine the physical properties, for example:

  3.1 Textural and morphological characterization.

  3.2 Thermal conductivity.

4. Study the moisture sorption isotherms and sorption kinetics of the composite desiccant by a constant temperature and humidity chamber and Vapor Sorption Analyzer (VSA).

5. Design the structure and improvement of thermoelectric dehumidifier (TED) with the improved composite desiccant under monitoring sensor control.

6. Test the thermoelectric dehumidifier (TED) with the improved composite desiccant.

7. Examine the system

  7.1 Numerical analysis of TED

  7.2 Electrical power and thermoelectric optimization module (TE)

  7.3 Humidity analysis.

  7.4 Dehumidification-Regeneration of the composite desiccant unit.

CHAPTER II

THEORY AND RELATED LITTERATURE REVIEW

This chapter proposes suggestions for preparing knowledge and necessary ideas in thermal comfort, moist air properties, dehumidification principle and techniques, desiccant, thermoelectric, and thermoelectric dehumidifier. However, the literature evaluation of earlier work on the thermoelectric dehumidifier, synthesized desiccants, and other related topics is given.

1. Thermal comfort

1.1 Thermal comfort considerations

Thermal comfort is the evaluation by each human of an environment and feeling either satisfied or unsatisfied. Experiments under various conditions in each environment with a comfort sensation indicator called the predicted mean vote (PMV) were first carried by Fanger, P. O (52). PMV has seven levels indicating a thermal sensation scale as **Table 2**:

Table 2 Seven levels indicating a thermal sensation scale

+3 hot	O neutral	-1 slightly
+2 warm		-2 cool
+1 slightly warm		-3 cool

When PMV is zero, thermal comfort is maintained, and the condition can be accepted when PMV falls within a 10.5 range (53). The most important factors that influence thermal comfort are the indoor air velocity, mean radiant temperature, occupant activity levels, and clothing levels, in addition to air temperature and relative humidity. This thermal comfort condition is based on the methodology presented in the ASHRAE 55 (1992) (54). All six factors contribute to indoor climate conditions. One of the interesting parameters is the mean radiant temperature that takes the environment temperature and effect of the position of each human in the room into account. For example, a person who works closely to a high-temperature window will be uncomfortable and hot on the part of the body next to a heat-absorbing window. At the same time, another part of the body that faces other walls will experience a lower temperature. Facing both, the window and wall simultaneously will make a human uncomfortable. Thus, the room air temperature alone does not indicate thermal comfort; mean radiant temperature is another significant factor of concern.

1.2 Measurement and calculation of thermal comfort parameters

Radiant Temperature of a Surface (T_i) To measure the surface temperature, one can resort to using a contact thermometer-a resistance or thermocouple one-and an infrared sensor.

Air Temperature (T_a) There are many kinds of sensors deployed for the measurement of air temperature. Among them, the resistance thermometer, the thermocouple, and the bimetallic thermometer are common examples. To reduce the relative influence of thermal radiation during the use of these sensors, however, any observations to be derived ought to shield the sensor from other sources of thermal radiation, e.g., sunlight, windows, and walls (54).

Mean Radiant Temperature (T_{mrt}) In light of the PMV evaluation and the variable mean radiant temperature is required, apart from the other three physical variables. The globe thermometer and two-sphere radiometers are some examples of measuring it (54). According to Fanger, P. O., this parameter can be defined as the uniform surface temperature of imaginary black surroundings that produce radiant heat, loss of an amount identical to that from a person who is in a given body posture and clothing, and at a given point in a room (52). As such, its calculation can approximately be obtained from measured surface temperatures in a room and the corresponding view factors to a person:

$$T_{mrt}^4 = \sum_j F_j T_j^4 \tag{1}$$

Air Motion A few examples of sensors used in measuring this parameter are the hot-wire anemometer, heated sphere anemometer, and vane anemometer. They should be omnidirectional or else must be directed very carefully to show the reading of actual air speed at a particular test position (54).

Operative Temperature (T_o) The operative temperature is the uniform temperature of an imaginary black enclosure. A person exchanges heat by radiation and convection with an equal one in an actual non-uniform environment. Accordingly, it can be assessed numerically as the average air temperature and mean radiant temperature, weighted by their respective heat transfer coefficients (h_c and h_r, respectively). It should be noted that a globe thermometer, which is 5-10 centimeters in diameter, can also be used to measure it directly (54). The following is the model used to calculate the temperature under discussion (55):

$$T_0 = \frac{\left(h_c T_a + h_r T_{mrt}\right)}{\left(h_c + T_{mrt}\right)} \tag{2a}$$

Where

T_0 is operative temperature, °C

h_c is coefficient of convection heat transfer, W K^{-1} m^{-2}

T_a is air temperature (dry bulb), °C

h_r is coefficient of radiation heat transfer, W K^{-1} m^{-2}

T_{mrt} is mean radiant temperature, °C

The convective heat transfer coefficient "h_c" can be assessed at atmospheric pressure and calculated for a seated person surrounded by moving air using the following equation (55),

$$h_c = 8.3\left(v^{0.6}\right)\left(For 0.2 \langle v \langle 4.0\right) \tag{2b}$$

The linearized radiative heat transfer coefficient "h_r" can be computed by means of the equation below:

$$h_r = 4\varepsilon\sigma \frac{A_r}{A_d}\left[273.2 + \frac{T_{cl} + T_{mrt}}{2}\right]^3 \tag{3}$$

As asserted above, the operative temperature can be estimated from the air temperature and the mean radiant temperature; therefore, it can additionally be calculated by the following formula:

$$T_0 = aT_a + (1-a)T_{mrt} \tag{4}$$

Where the weighting factor (a) depends upon the air speed (υ) in approximately the **Table 3**:

Table 3 Weighting factor depends upon the air speed in approximately

$\upsilon\left(ms^{-1}\right)$	0-0.2	0.2-0.6	0.6-1.0
a	0.5	0.6	0.7

Humidity: Some instances of instruments in aid of air humidity measurement include the electrical conductivity or capacity hydrometer. Calibrating the humidity level in the air can be measured in a variety of ways-for example, via dew point, relative humidity, wet bulb, or vapor pressure, and converted into other measurements utilizing comparison tables or specific psychrometric charts (54).

Physical/Personal Variables There are two categories to be discussed under this designation. The first is the metabolic rate (M); the other is clothing insulation (I_{cl}). The metabolic rate denotes the energy-production rate of a body. **Table 4** shows some typical metabolic rates. Under this standard, metabolism, which is subject to a type of activity, is incorporated. If a person is seated and immobile, the metabolic rate of a unit surface area will amount to 58.2 W m^{-2}, based on an overall surface area of a person at 1.8 m^2 (54).

Table 4 Metabolic rates of different activities

Activity	Met	W m^{-2}	W (average)
Sleeping	0.7	40.4	70
Reclining	0.8	46.6	80
Seated and quiet	1.0	58.2	100
Sedentary activity (office, lab, school)	1.2	69.8	120
Standing, relaxed	1.2	69.8	120
Light activity, standing (shopping, laboratory experiment, light industry)	1.6	93.1	160
Medium activity, standing (shop assistant, domestic work, machine work)	2.0	114.4	200
High activity (heavy machine work, garage work, if sustained)	3.0	174.6	300

"Note" Typically, rest breaks (schedule or hidden) or other operational factors (get parts, product, etc.) combine to limit individual work to the time-weighted average level of about two met.

The latter relating to clothing insulation refers to the variable governed by increased resistance to sensible heat transfer resulting from putting an individual piece of clothing over an undressed body. The resistance equals the effective increase in total insulation characterized by that particular garment and is usually rated in clo units (54). **Table 5** gives the clo-values of various pieces of garments.

Table 5 Insulation value of clothing elements

Item	$\left(I_{clo}\right)$ (clo)
Garment	
T-shirt	0.08
Men's briefs	0.04
Ankle length sock	0.02
Shoes	0.02
Long sleeve dress shirt	0.19
Thin trouser	0.15
Thick trouser	0.24
Single-breasted jacket (thin)	0.36
Single-breasted jacket (thick)	0.42
Ensemble	
Brief, long-sleeve shirt, thin trousers, socks, shoes	0.60
Brief, T-shirt, long sleeve shirt, single-breasted jacket, trousers, socks	1.20

1.3 ISO 7730: moderate thermal environments-determination of the PMV and PPD indices and specification of the conditions for thermal comfort

The comfort standard for the International Standards Organization (ISO) is entitled, "Moderate thermal environments-determination of the PMV and PPD indices and specification of the conditions for thermal comfort." This standard is used by most of the world outside the U.S. and incorporates the PMV-PPD model.

PMV is an empirical function derived from the physics of heat transfer and the thermal responses of people in climate chamber tests. PMV establishes a thermal strain based on environmental conditions and attaches a comfort vote to that amount of strain. Suppose the environmental conditions combined with the activity and clothing of the person, you are modeling produce a PMV within the range of -0.5 to +0.5. In that case, the condition meets the ISO comfort sensation recommendation (56).

The PMV equation for thermal comfort is a steady-state model. It is an empirical equation for predicting the mean vote on an ordinal category rating scale of the thermal comfort of a population of people. The equation uses a steady-state heat balance for the human body. It postulates a link between the deviation from the minimum load on heat balance effector mechanisms, e.g., sweating, vaso-constriction, vaso-dilation, and thermal comfort vote. The PMV equation only applies to humans exposed to constant conditions at a constant metabolic rate for a long period. It is written as:

$$PMV = f\left(M, L\right) \tag{5}$$

$$L = H - E - E_d - E_{sw} - I - R - C \tag{6}$$

Where

L is the thermal load on the body

H is the internal heat production

E_d is heat loss due to water vapor diffusion through the skin

E_{sw} is heat loss due to sweating

I is dry respiration heat loss

R is heat loss by radiation from the surface of the clothed body

C is heat loss by convection from the surface of the clothed body

The equation is expanded by substituting each component with a function derivable from fundamental physics. All functions have measurable values except clothing surface temperature and the convective heat transfer coefficient, which are functions of each other. To solve the equation, an initial value of clothing temperature is estimated, the convective heat transfer coefficient computed, a new clothing temperature calculated, etc., by iteration until both are known to a satisfactory degree (56).

1.4 Indoor air quality-thermal comfort and health

Air conditioning is used to the central temperature, humidity, air circulation, and air quality within indoor environment control. The recent comfort zone has necessary for HVAC designers responding to building construction. Commonly the environment's comfort zone has been healthy, but an indoor environment may be without the healthy. However, some overzealous attempts to energy saving and reduction of outdoor air have influenced occupant health. Therefore, the current health and comfort zone are both concerns when humans spend their time more than the other activity, especially indoor space.

The impact of the indoor environment on quality and efficiency are additional significant parameters in the building settings. This chapter concerns several conditions that suitable thermal comfort and healthful indoor for humans. Air contaminant is started by outdoor air that is a primary means of appropriate indoor air quality. Increasing the building's intensity and realizing energy conservation has caused a decrease in the outdoor air entrance. Furthermore, the building has risks from equipment, furniture, gas emission from various materials, and volatile organic compounds (VOCs). So, the overall impact of harming human health. That is called "sick build syndrome." The HVAC is becoming for their problem’s management and advanced research.

However, giving attended economics, safety, and health increases, but an indoor environment's comfort zone is still essential for HVAC technology. Various factors or parameters influence the comfort zone but still have primary air temperature, humidity, and some equipment's thermal radiation. Nevertheless, the smell, dust, lighting, and noise are the factor that may be effective not to feel "comfortable". This chapter focuses on the background of ASHRAE 62.2, "Ventilation for Acceptable Indoor air quality", understanding process ventilation and HVAC system.

ASHRAE standard defines indoor air quality as air without contaminant harmful as calculated by the methodology that component a substantial majority, approximately 80% of people. Acceptable IAQ, not only the indoor comfort zone but also environmental odor and harmful contaminant level. Therefore, central considers the thermal comfort, which consists of essential control of humidity, temperature, air circulation, and recovery air. However, many cases have a direct impact on human health or building occupants.

The contaminants include carbon dioxide, carbon monoxide, other gas and radiation materials, viruses, and bacteria that live in the air or small particle. Thus, indoor space management depends on ventilation, HVAC, or DOAS system that resolve air contaminants caused by human and animal occupancy. Therefore, high indoor air quality usually economics and costs force sometimes saving for initial and carry out.

In the part of thermal comfort was considered, and studied research that using different methodology depending on climate or conception such as thermal comfort in office (57-60), thermal comfort by using air-condition (61-63), schools (64), industrials ventilation (65), dormitory (66, 67), occupant impacted (68-71), designed building construction (72, 73), designed and modified system ventilation (74, 75) and application of HVAC-DOAS (76-79).

1.5 Previous studies of thermal comfort in Thailand

There are many cases of thermal comfort studies in Thailand. In the early field studies, a questionnaire survey following the rating scales of ASHRAE with simultaneous physical measurements was the norm. For example, 1,100 employees were investigated in a comfort condition case study in air-conditioned and non-air-conditioned buildings in Bangkok. The results showed that the thermal acceptability existed across a broad range of temperatures, pushing the summer comfort outward by a few degrees Celsius (4 °C (80), 5.5 °C (81)). According to the Busch, J.F. study, 80% of Thai workers were satisfied at an upper limit temperature of 28 °C in air-conditioned buildings and 31 °C in naturally ventilated buildings (80).

In another case study, Khedari, J. tested thermal comfort with an air velocity range of 0.2 and 3 m s^{-1} from commercial electric fans in ventilated "non-conditioned" spaces occupied by Thai college students (183 males and 105 females) who wore normal clothes (0.54 to 0.55 clo) under sedentary activity (1 met) (82). The room temperature extended from 26 to 36 °C (dry bulb temperature) with 50 to 80% relative humidity. The data were recorded by questionnaire, and the indoor neutral temperature was analyzed with PMV. The results indicated that thermal comfort was obtained at an air velocity of 0.5 m s^{-1} (60% RH <70%) and a mean neutral temperature of 28.30 °C. Increasing the air velocity to 1 m s^{-1} in the same relative humidity range allowed the mean neutral temperature to be increased to 30.15 °C with comfort maintained.

In an environmental chamber at Chulalongkorn University, Srivajana investigated the effect of air velocity on thermal comfort for 128 college students (0.48 clo, 1.2 met). The air velocity sensation and preference vote resulted in 80% of volunteers being satisfied, not feeling draughty, but disturbed with an air velocity not more significant than approximately 0.9 m s^{-1} (83). According to research by Tantasavasdi, C., Srebric, J., and Chen, Q., natural ventilation was found to be usable in creating a thermal comfort indoor environment in houses based on the thermal comfort requirements for Thai people with the climate condition in Bangkok suburbs during a few months of the year (84).

2. Moist air properties

The study of desiccant dehumidifiers requires knowing the properties of process airs under different states. The following summarizes a set of formulas that can be applied to determine the air's acceptable accurate level properties when two other properties are known. An alternative approach to using a Psychometric chart is presented next.

The atmosphere is a mixture of air and water vapor. Atmospheric air contains nitrogen, oxygen, carbon dioxide, water vapor, other gasses, and various contaminants. Dry air is defined as contaminants and water vapor removed from atmospheric air; by contrast, moist air is the moisture of dry air and water vapor. Air properties are important for living activities, ventilating a livestock-housing unit, drying grains, or determining relative humidity at a given place. Since the moisture-holding capacity of air varies with increasing temperature in the home, moisture can either be added to or removed from the air to change the relative humidity.

Air temperature measures the heat content of air with three measurements, i.e., dry bulb, wet bulb, and dew point temperatures. Dry bulb temperature is usually simply air temperature that can be measured using a standard thermometer or more sophisticated sensor. Wet-bulb temperature represents how much moisture the air can evaporate. A thermometer enclosed in a wet wick and a known air velocity passing over it usually measures it. The amount of evaporation is a direct indication of dew point is the moisture carrying capacity of the atmospheric air at that temperature. The temperature at which water vapor starts to condense.

2.1 Calculation of moist air properties

Moist air in the atmosphere is a binary mixture of dry air and a small amount of water vapor in equilibrium at a given temperature and pressure. The pressure is relatively low so that the behavior of dry air, water vapor, or the mixture can all be examined under ideal gas law.

2.1.1 Pressure

According to Dalton's law, the total pressure exerted by a gas mixture is the sum of the partial vapor pressure of each component:

$$p = p_a + p_w \tag{7}$$

Where

p is the total pressure exerted by the mixture

p_a and p_w are partial pressure exerted by dry air and water vapor, respectively

In the given volume V (m³) of the binary mixture at absolute temperature T_{abs} (K), the following relationships are obtained according to the ideal gas law:

$$p_a V = \frac{m_a R T_{abs}}{M_a} \tag{8}$$

And,

$$p_w V = \frac{m_w R T_{abs}}{M_w} \tag{9}$$

Where

m_a is the mass of the dry air in the volume, kg

m_w is the mass of the water vapor in the volume, kg

R is the universal gas constant, 8.315 kJ (k mol K)$^{-1}$

M_a is the molecular weight of dry air, 28.9645 kg k^{-1} mol^{-1}

M_w is the molecular weight of water vapor, 18.0153 kg k^{-1}mol^{-1}

2.1.2 Humidity ratio

The humidity ratio or the absolute humidity (W) of moist air at a given condition is the ratio of the mass of water vapor to the mass of dry air contained in the same volume. The equation can calculate the humidity ratio

$$W = \frac{m_w\left(kg\ water\ vapor\ in\ the\ mixture\right)}{m_a\left(kg\ dry\ air\ in\ the\ mixture\right)} \tag{10}$$

From Equations (8) and (9), we obtain

$$W = \frac{M_w}{M_a} \times \frac{p_w}{p_a} \tag{11}$$

$$W = \frac{18.01528}{28.9645} \times \frac{p_w}{p_a} \tag{12}$$

$$W = \frac{0.62198 p_w}{p - p_a} \tag{13}$$

The relationship between the humidity ratio and the relative humidity is expressed as

$$W = \frac{0.62198\phi_w p_{ws}}{p - \phi_w p_{ws}} \tag{14}$$

Where p =101.325 kPa at standard condition, m_w is the weight of moist air, m_a is the weight of dry air, P is the atmospheric pressure, and P_w is the water vapor partial pressure.

2.1.3 Specific volume

The specific volume (v), m^3 kg^{-1} dry air of a moist air mixture is the volume of that mixture per unit mass of dry air:

$$v = \frac{V}{m_a} \tag{15}$$

From Equation (8), this can also be expressed as

$$v = \frac{RT_{abs}}{p_a M_a} \tag{16}$$

Writing $p_a = p - p_v$ and substituting $M_a = 28.9645$ in the last expression gives

$$v = \frac{RT_{abs}}{(28.966)(p - p_w)} \tag{17}$$

Substituting the value for the universal gas constant R, and the last expression is reduced to

$$v = \frac{0.2871T_{abs}}{(p - p_w)}, m^3 / kg\ dry\ air \tag{18}$$

2.1.4 Relative humidity

The relative humidity $\left(\phi_w\right)$ of moist air at a given temperature and pressure is the ratio of the existing partial vapor pressure $\left(p_v\right)$ to the saturation pressure at the same temperature and pressure $\left(p_{vs}\right)$. In practice, relative humidity indicates the moisture level of the air compared to the moisture-holding capacity. The relative humidity can be calculated with the equation

$$\phi_w = \frac{p_w}{p_{ws}} \tag{19}$$

This quantity has no unit and is often expressed in terms of percentage.

2.1.5 Saturation vapor pressure

Under a given pressure, the maximum vapor pressure, or saturation vapor pressure, is related to the temperature. From ideal gas law, this relationship is given as:

$$p_{ws}\left(T_{abs}\right) = \exp\left[53.5224 - \frac{6834.27}{T_{abs}} - 5.17\ln\left(T_{abs}\right)\right], kPa \tag{20}$$

A similar relationship is given by ASHARE (ASHARE, 2009) for the temperature range of 0 to 200 °C as:

$$p_{ws}\left(T_{abs}\right) = \exp\left[\frac{C_1}{T_{abs}} + C_2 + C_3T_{abs} + C_4T_{abs}^2 + C_5T_{abs}^3 + C_6\ln\left(T_{abs}\right)\right], kPa \tag{21}$$

Where

$$C_1 = -5.8002206 \times 10^{3}$$
$$C_2 = -5.516256$$
$$C_3 = -4.8640239 \times 10^{-2}$$
$$C_4 = 4.1764768 \times 10^{-5}$$
$$C_5 = -1.4452093 \times 10^{-8}$$
$$C_6 = 6.5459673$$

2.1.6 Wet bulb temperature

The air's wet-bulb temperature is measured by a thermometer whose bulb is covered by a muslin sleeve, which is kept moist with distilled and clean water, freely exposed to the air, and free from radiation.

2.1.7 Enthalpy of moist air

The enthalpy of moist air is the sum of the enthalpy of each constituent. The enthalpy of dry air (h_a) is given as

$$h_a = C_a\left(T - T_R\right), \frac{kJ}{kg} \tag{22}$$

Where

C_a is the specific heat capacity, kJ (kg K)$^{-1}$ of dry air

T is (dry bulb) temperature

T_R is the reference temperature

In SI UNIT, T_R is at 0 °C. For the normal temperature range (0 to 100 °C), the value of C_a is 1.006 kJ (kg K)$^{-1}$. Therefore, the enthalpy of dry air can be expressed as

$$h_a = 1.006T, \frac{kJ}{kg} \tag{23}$$

The enthalpy of water vapor (h_v) comprises the enthalpy of water vapor at the reference temperature h_g =2501 kJ (kg K)$^{-1}$, and the enthalpy of superheated vapor at T :

$$h_v = h_g + C_{pv}T, \frac{kJ}{kg} \tag{24}$$

Where C_{pv} is the specific heat capacity of the superheated vapor. Its value is given as 1.805 kJ (kg K)$^{-1}$. The enthalpy of moist air (h) is then given as

$$h = h_a + Wh_v \tag{25}$$

$$h = 1.006T + W\left(2501 + 1.805T\right), kJ / kg\ dry\ air \tag{26}$$

2.1.8 Dew-point temperature

The dew point temperature of moist air is the saturation temperature reached when it is cooled down without moisture added or extracted from it. The dew-point temperature can be calculated from the partial vapor pressure p, of the given moist air using the following relationship (ASHARE, 2009): Between dew points of 0 and 93 °C,

$$T_{dp} = 6.54 + 14.526 ln\left(p_w\right) + 0.7389\left[\ln\left(p_w\right)\right]^2 + 0.09486\left[\ln\left(p_w\right)\right]^3 + 0.4569\left(p_w\right)^{0.1984}, {}^{o}C \tag{27}$$

2.2 Psychrometric chart and psychrometric process

Psychometrics is the science involving the thermodynamic properties of moist air and the effect of atmospheric moisture on materials and human comfort. A psychrometric chart represents the thermodynamic properties of moist air by a point that gives the dry bulb, wet bulb, relative humidity, specific volume, and saturation temperatures of the atmosphere, as shown in **Figure 1**. The chart is convenient for solving numerous process problems involving moist air and its components (85).

Dry bulb temperature is shown along the bottom axis of the psychrometric chart, and it is constant in the vertical line upward. The slope lines moving upward to the left, which is read at the saturation line, indicate wet-bulb temperature. The following horizontal line from the state-point to the saturation line reads the dew-point temperature. The humidity ratio is indicated along the right-hand axis of the chart, while the relative humidity lines are shown as curved lines that move upward to the left in 10% increments. The line representing saturated air (RH 100%) is the uppermost curved line on the chart.

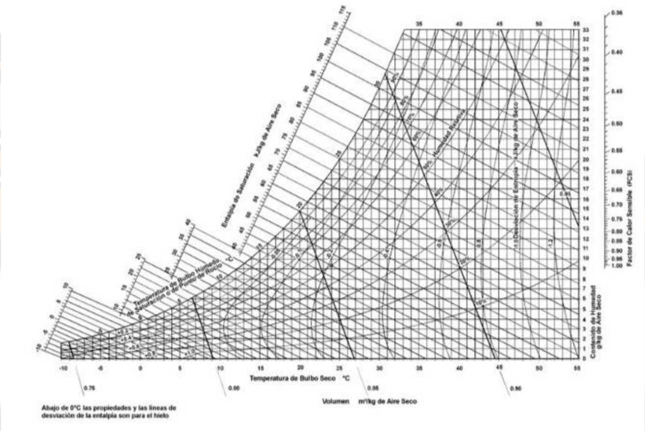

Figure 1 Psychometrics chart indicates the dry bulb and wet bulb temperature, humidity ratio, and relative humidity

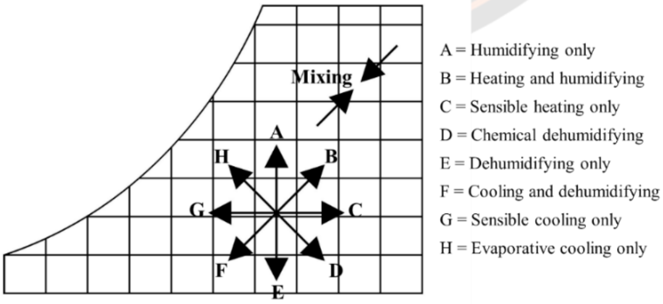

Figure 2 The Psychrometric process

The movement of the state point on the chart can represent the psychrometric process, i.e., any changes in the condition of the atmosphere. The typical process includes:

1. Heating or cooling: The addition or removal of heat without any change in the moisture content, but it is a change in dry bulb temperature. The processes are shown in **Figure 2**, in which direction C represents heating and direction G means cooling.

2. Humidifying or dehumidifying only: The state changes in humidity ratio with no change in dry bulb temperature. For the latent heat process, the moisture content of the air is changed but not the temperature (direction A or E).

3. Cooling and dehumidifying result in a reduction of both the dry bulb temperature and humidity ratio. Cooling coils generally perform this type of process (direction F).

4. Heating and humidifying increase both the dry bulb temperature and the humidity ratio (direction B).

5. Chemical dehumidifying is when moisture from the air is adsorbed or absorbed by a hygroscopic material. Generally, the process occurs at constant enthalpy (direction D).

6. Evaporative cooling is an adiabatic heat transfer process in which the wet-bulb temperature drops as the humidity rises (direction H).

Adiabatic mixing of the air at one condition with air at another condition is represented on the chart by a straight line drawn between the points representing the two air conditions.

As shown in **Figure 3**, the process air entering the solar air heater (point 1) is near ambient temperature and has high relative humidity. After passing through the collector, the process air was at a higher temperature and the same humidity ratio but low relative humidity. The hot air at point 2, passing upwards through the silica gel beds, removes the water content of silica gel grains due to its low relative humidity. At point 3, the outlet air has a higher humidity ratio and a lower temperature than the air at point 2 due to the desorption of water from the silica gel, implying a reduction of water content from the silica gel during the process of regeneration.

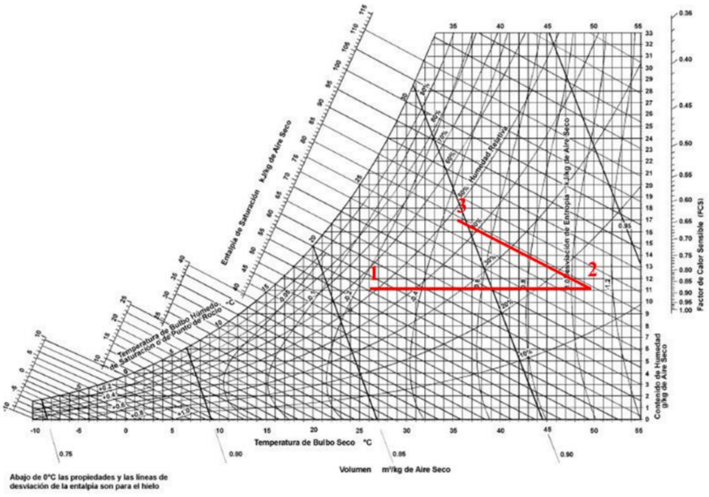

Figure 3 Psychrometric chart shows the properties of the process air at three points

The humidity ratio (W) between points 1 and 2 is constant, but at point 3, it is increased. T_1, T_2 and T_3 are the process air temperatures and h_1, h_2, and h_3; are the enthalpies of the moist air at points 1, 2, and 3, respectively. In the heating process (points 1 and 2), the temperature rise is different by $T_2 - T_1$, and the enthalpies are h_1 and h_2. The heating rate (Q_h) can be written as an equation

$$Q_h = G\left(h_2 - h_1\right) \tag{28}$$

Where G is the mass flow rate (kg s^{-1}). Substituting Equation (26) into Equation (28), the energy balance equation for heating the process air is expressed as

$$Q_h = G\left[\left(T_2 - T_1\right) + 1.86W\left(T_2 - T_1\right)\right] \tag{29}$$

For the regeneration process (points 2 and 3), the heat for regeneration Q_R is determined by the change of enthalpy of the air at points 3 and 2 as follows:

$$Q_R = G\left(h_3 - h_2\right) \tag{30}$$

$$Q_R = G\left[\left(T_3 - T_2\right) + \left(w_3 - w_2\right)2501.3 + 1.86\left(w_3T_3 - w_2T_2\right)\right] \tag{31}$$

Where $T_3 - T_2$ is the temperature difference and $w_3 - w_2$ is the humidity ratio difference between points 3 and 2, respectively.

3. Dehumidification principle and techniques

A dehumidifier is a device that controls the moisture content in a closed space. It can maintain the air comfort level or dehumidify the moist air and collect the condensed water. Dehumidifiers have many applications, from the recovery of structure materials affected by moisture to indoor thermal comfort for human activities (5). There is a range of small/large scale and portable techniques where dehumidification plays a vital role. Dehumidification can be attained either by cooling the air or by heating it. In cooling and dehumidification, the moist air needs to be dehumidified, passing over a cold surface for moisture condensation. However, heating and dehumidification are done by using hygroscopic materials (86). Dehumidification of air in the cooling and dehumidification process occurs when it is cooled below its dew point temperature (T_{dew}). Hence, the cooled surface is maintained at a temperature below the dew point temperature of the air. Therefore, when moist air passes over, the dry bulb temperature (T_{DBT}) starts reducing, and at a certain point, it reaches its dew point temperature, as shown in **Figure 4(a)**. From this point, moisture in the air starts converting into dew particles leftover at the cooled surface. In the heating and dehumidification process, the moist air is passed through a vessel containing hygroscopic material. The hygroscopic material tends to absorb moisture and emits heat. This leads to dehumidification of air, and the dry bulb temperature of the air increases. Meanwhile, its dew point temperature and wet bulb temperature (T_{WBT}) decrease, as illustrated in the psychometric chart schematic **Figure 4(b)**.

Dehumidification can be broadly classified in two ways, namely cooling and heating-based dehumidification, as shown in **Figure 5** (15). The most common dehumidification techniques are vapor compression and desiccants. The vapor compression technique simply operates the vapor compression refrigeration cycle to cool incoming moist air (87). The incoming moist air is passed over the cooling coils in which the refrigerant circulates, and then the moisture content of air condenses over the coils and drips down from its surface to the water collector. Therefore, the coolant used in cooling coils is the evaporator part of the vapor compression refrigeration cycle (88).

Conversely, in desiccant-based dehumidifiers, moisture-absorbing materials are used. In the adsorption-based desiccant, the moisture content from the moist air passed through the desiccants is trapped on its surface, and the dry air is obtained. The most commonly used desiccant for this process is silica gel (40). In the case of absorption desiccants, liquid desiccant such as LiCl is used. The dry air obtained in both the cases of desiccants has a higher value of temperature; hence it needs to be passed through a cooling element or cooling agent before supplying to the thermal comfort sensible range (41).

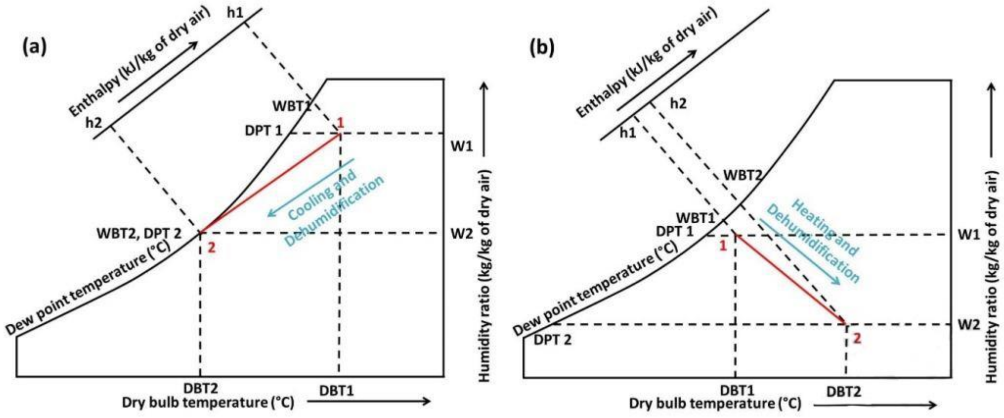

Figure 4 Cooling and dehumidification process (a), and heating and dehumidification (b) on psychometric chart

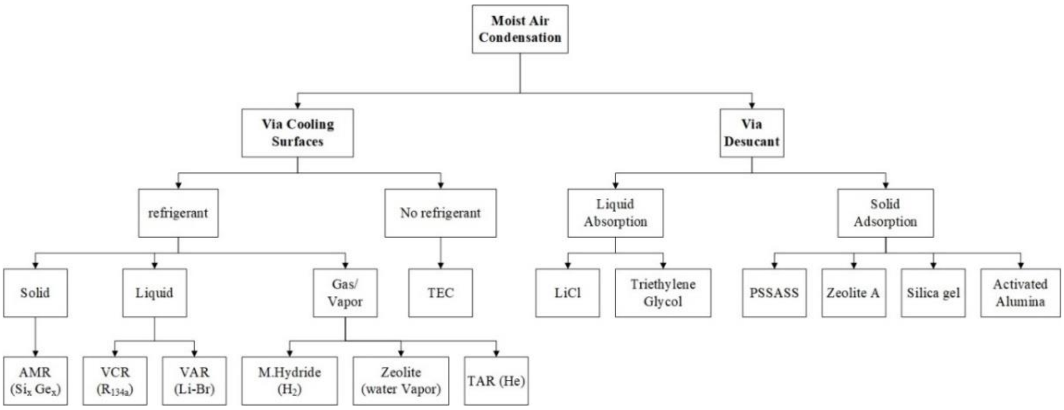

Figure 5 Classification of air dehumidification. (AMR-active magnetic regenerator, M.Hyd-metal hydride systems, TAR-thermoacoustic refrigeration, TEC-thermoelectric cooler, VAR-vapor absorption refrigeration, VCR-vapor compression refrigeration, PSSASS-polystyrene sulfonic acid sodium salt)

3.1 Desiccant dehumidification systems

Desiccant cooling principles were introduced more than 80 years back in the 1930s by Hausen. Desiccants are chemicals that can absorb or release moisture from the surrounding air. The driving parameter for this exchange is the difference in vapor pressure between the desiccant surface and the surrounding air (89). As long as the desiccant surface vapor pressure is lower than the surrounding air, moisture would transfer from air to desiccant material. The moist exchange process stops once the desiccant material is saturated and reaches equilibrium in moist content with the surrounding air. To reuse the desiccant, it has to be regenerated by extracting the moist content out of it. The regeneration of the desiccant material can be done through an absorption process that includes chemical and physical transformation or through an adsorption process, which does not have any chemical or physical exchanges. Desiccant materials can be of two types: solid or liquid desiccants, as shown in **Figure 6**. Solid desiccants work with adsorption processes, whereas liquid desiccants absorb moisture through chemical and physical processes (89).

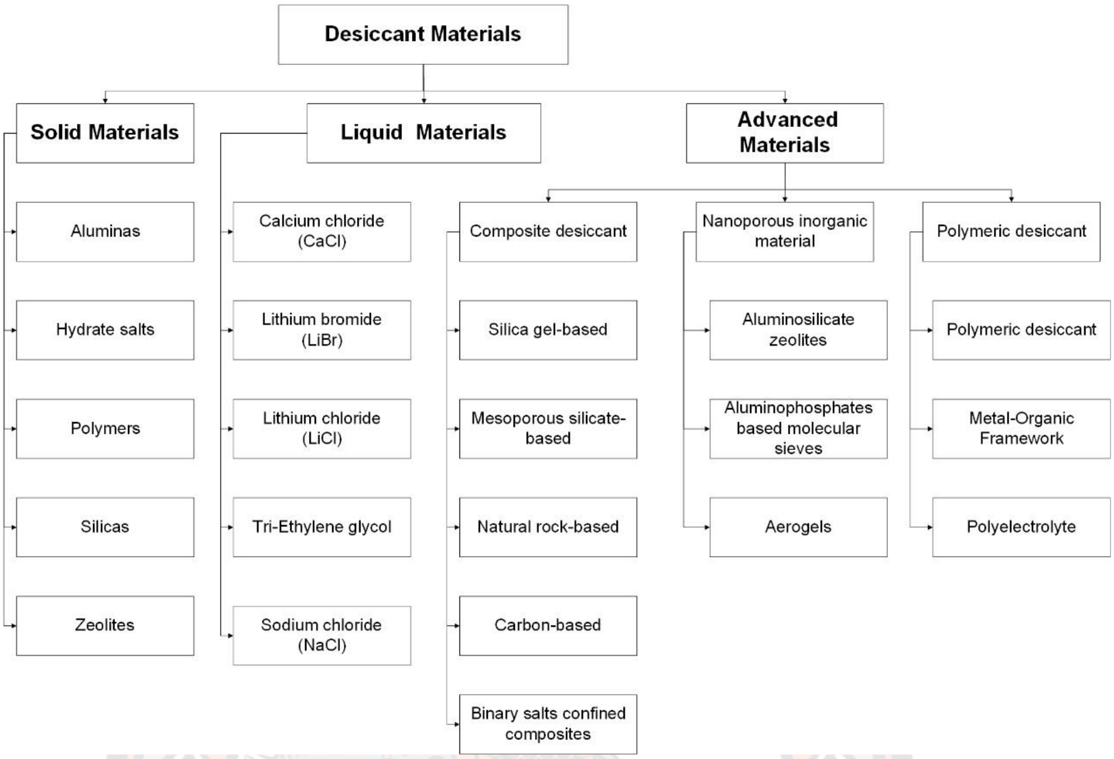

Figure 6 Common solid, liquid advanced desiccant materials

3.2 Desiccant dehumidification applications

Desiccant systems are advantageous when the latent load is high (i.e., when the latent-to-sensible heat ratio is high) because they remove moisture more economically than they remove sensible heat. Another desirable situation is when dehumidification with a desiccant is lower than the cost of dehumidification with a refrigeration system; this is where thermal energy appears: there are instances where desiccant regeneration done by waste heat, natural gas, or off-peak electricity is more economical than regular electric refrigeration. Because there is no need for reheating with desiccant dehumidification systems, another appropriate use is when conditioned air must be reheated after coming out of a coil to reach a comfortable dry-bulb temperature. Finally, using a desiccant is well suited to the case where dehumidification is required at levels below freezing dew-point temperatures. For example, an ice arena has is a great deal of humidity, but the cooling coil has to cool below the freezing point. In such an environment, dehumidification with desiccants can play a significant role.

Generally, all desiccants function by the same mechanism transferring moisture because of a difference between the water vapor pressure at their surface and that of the surrounding air. When the vapor pressure at the desiccant surface is lower than that of the air, the desiccant attracts moisture, and at the contrary state, it releases moisture. When the vapor pressure of the desiccant and the surroundings are the same, it stops attracting or releasing moisture. The process of moisture leaving the surface of the desiccant is called regeneration. An ideal desiccant for the space-conditioning application depends on the range of water vapor pressure that is likely to occur in the air, the temperature level of the regeneration heat source, and the moisture sorption and desorption characteristics of the desiccant within those constraints.

A solid desiccant has a large surface area to attract moisture from the surroundings. It attracts moisture because of the electrical field at the surface. The field is not uniform in force or charge, so it attracts water molecules with a net opposite charge from specific sites on its surface. When the complete surface is covered, the adsorbent can hold still more moisture as vapor condenses into the first water layer and fills the capillaries throughout the material. The adsorption behavior of solid absorbents depends on their total surface area, the total volume of their capillaries, and the range of their capillary diameters. A large surface area gives the absorbents a large capacity at low relative humidity. Large capillaries provide a high capacity for condensed water, which gives the absorbent a high capacity at high relative humidity. A narrow range of capillary diameters makes an adsorbent more selective in the vapor molecules it can hold (90).

The desiccant media is a natural or synthetic substance capable of absorbing or adsorbing water vapor due to the difference in water vapor pressure between the surrounding air and the desiccant surface. Many desiccant materials are available, such as silica gel, activated alumina, synthetic zeolites (molecular sieve), or alumina gel. All desiccants behave similarly to attract moisture until reaching an equilibrium state in the adsorption process. The moisture is usually removed from the desiccant by heating with temperatures between 50 and 260 °C in the desorption process to attract moisture once again. The adsorption process always generates the sensible heat equal to the latent heat of the water vapor taken up by the desiccant plus an additional heat of the sorption that varies between 5 and 25% of the latent heat of water vapor (90).

Silica gel is a suitable adsorbent at a relative humidity between 50 to 80%, so it is ideal as a solid desiccant for air conditioning. The adsorption isotherm of water vapor on silica gel is shown in **Figure 7**. The water content in silica gel depends on the relative humidity of the moist air (85).

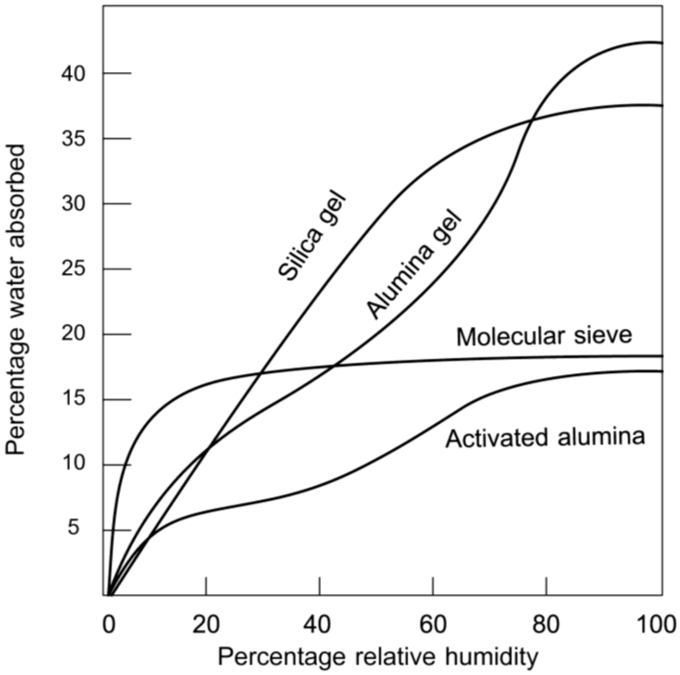

Figure 7 The adsorption isotherms of water vapor for different solid desiccants

Silica gel is a partially dehydrated polymeric form of colloidal silicic acid with the formula ($xSio_2 \cdot yH_2O$). This amorphous material comprises spherical particles 2 to 10 nm in size, which aggregate to form the adsorbent with pore sizes in the range of 6 to 25 nm. Silica gels are porous and granular forms of amorphous silica developed by a complex net of microscopic pores that attract and retain water or organic solvents through physical adsorption. Porous silica has a sponge structure, resulting in a very high specific surface area that varies significantly with a pore size (from 20 to 750 m^2 g^{-1}). This surface area is essentially the internal area of the pore walls. Surface area measurements can obtain the average pore size because even the smaller pores are larger than most molecules. However, of the same order of magnitude, it is not a surprise that mobility restrictions do occur for adsorbed molecules. Porous silica surface contains both silanol (Si-OH) and siloxane groups (Si-O-Si). Silanols are considered to be strong sites for adsorption, while siloxanes are hydrophobic sites. Silanols may be isolated, vicinal, or geminate and linked by hydrogen bonds to the surface water.

Figure 8 schematically shows the silica surface. In the pioneering study of Snyder and Ward, H-bonded silanols form pairs, and these pairs were considered to be the more active sites on a surface (due to an enhanced acidity of the proton not engaged in the H-bond), responsible for probe adsorption at the silica surface. We now know (by temperature-programmed desorption studies) that isolated silanols are the more reactive sites on the silica surface. H-bonded silanols have desorption energy of 50 to 60 kcal mo1^{-1} and the isolated silanols ~90 kcal mo1^{-1}. Moderate heating of silica in a vacuum (100 to 120 ^{o}C) ensures a quasi-complete removal of the physically adsorbed water. However, the final water monolayer is removed at activation temperatures of 200 ^{o}C. Higher temperatures (200 to 1000 ^{o}C) promote the removal of chemisorbed water (91).

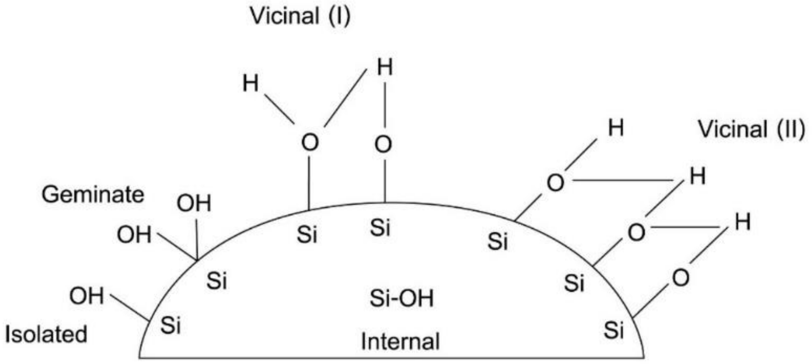

Figure 8 Schematic representation of silica surface

Nowadays, there is various dehumidification for the dehumidified humidity of the air before supplying it to the space. Some researchers conducted investigations on different desiccant components, desiccant wheels, etc., for dehumidification. However, there are consumed more energy for regenerated desiccant before dehumidifier. However, many researchers developed desiccants coated on heat exchangers (DCHE) to solve this problem.

3.2.1 Performance of cross-flow and counter-flow regenerators

Liu et al. studied the effects of air and desiccant inlet parameters on the regenerator performance and comparisons between present cross-flow regenerators and other counter-flow ones. The comparison results show moisture removal rate increases with increasing airflow rate, desiccant flow rate, and desiccant inlet temperature decreases with air inlet humidity ratio and desiccant inlet concentration and changes little with air inlet temperature. Regenerator effectiveness increases with desiccant flow rate, and inlet concentration decreases with airflow rate and desiccant inlet temperature and is affected little by air inlet temperature and humidity ratio. The impacts of air and desiccant inlet parameters are similar to those previously reported for counter-flow regenerators. Dimensionless mass transfer correlation is calculated in the present study, which is correlated by Reynolds number, Schmidt number, flow rate ratio of desiccant to air, and water content of the desiccant. A good agreement is shown between the predicted values and experimental data with a correlation coefficient of 0.962 (92).

3.2.2 Effect of various parameter indices

Abdalla et al. studied the performance of an internally cooled dehumidifier using Triethylene Glycol as a desiccant. During the experimental investigation, the dehumidifier inlet parameters, including airflow rate, humidity ratio, temperature, desiccant flow rate, and temperature, vary. The effect of these variables on the moisture condensation rate and dehumidifier effectiveness was studied. It is found that the moisture condensation rate increases with increasing the inlet airflow rate, inlet air humidity ratio, desiccant flow rate, and desiccant solution concentration. In contrast, the dehumidifier effectiveness increases with increasing desiccant flow rate and concentration. The dehumidifier effectiveness decreases with increasing inlet air flow rate and humidity ratios (93).

Jia et al. experimented on the dehumidification performances of the composite desiccant wheel and compared them with those of the silica gel wheel. The test results indicate that the moisture removal capacity of the new composite desiccant wheel, on average, is more significant than that of the traditional silica gel wheel by 50%. High hygroscopic LiCl is embedded in the pore channels of the silica gel improves its moisture adsorption capacity. The moisture removal capacity and COP are affected by the inlet air humidity. They increase with an increase in inlet air humidity. Especially the composite desiccant wheel possesses evident dominance at low relative humidity higher regeneration temperature results in more moisture removal capacity for the two desiccant wheels. However, there are different optimal regeneration temperatures for them. The optimal regeneration temperature of the composite desiccant wheel is lower than that of the silica gel wheel (94).

3.2.3 Desiccant coated on heat exchanger

Dehumidification processes are essential operation in various applications to remove water vapor from the air, gases, or other fluids. Drying gases under pressure are normally used to eliminate condensation and subsequent corrosion, maintain a dry atmosphere in a closed space or container, and control humidity in warehouses and caves for storage, and dry process and industrial gases. In common practice, dehumidification usually refers to equipment operating at essentially atmospheric pressures and built to standards similar to other types of air handling equipment. The solid desiccant dehumidifiers usually employ stationary beds or rotary wheel beds for packing desiccant media, namely desiccant column and desiccant wheel, respectively. In the former case, two or more desiccant columns are constructed with controlled valves to work alternatively in the adsorption and regeneration process. Secondly, dehumidifier, moist air is dried through one side of the wheel, while a heated air stream dries the wet desiccant on the other side of the wheel at the same time.

In addition, Ge et al. used desiccant dehumidifiers as desiccant-coated heat exchangers, which are fin-tube heat exchanging devices coated with silica-gel and polymer materials. An experimental setup is designed and built to test the performance unit. The result shows that this desiccant-coated unit overcomes the side effect of adsorption heat, which occurs in the dehumidification process, and achieves good dehumidification performance under given conditions. Moreover, the silica-gel coated heat exchanger behaves better than the polymer materials (95).

Ge et al. conducted research based on the whole desiccant cooling system utilizing two DCHEs by simulation. It is found the operation time in the dehumidification process is a crucial factor for the cooling capacity of the DCHE system, which can be enhanced by eliminating the initial period with higher outlet air temperature, the most significant cooling power of the DCHE system increase from 2.6 to 3.5 kW by eliminating first 50 s of operation time under ARI summer condition. Also, the DCHE system can only provide cooling power after a short operating duration from the initial dehumidification process (96).

Ge et al. studied solar-powered desiccant coated heat exchanger cooling systems which can provide satisfying supply air to the conditioned indoor space from 8:00 to 17:00 in June and July, the highest cooling powers are 2.9 kW and 3.5 kW, and corresponding solar COP are 0.22 and 0.24, respectively (97).

Zhao et al. has experimentally set up a desiccant dehumidification unit in which a silica gel coated fin-tube heat exchanger is installed and investigated. In this unit, two silica gel coated heat exchangers (SCHE) are adopted and switched to provide continuous dehumidification capacity. Meanwhile, hot water from the vacuum tube solar collector is used to regenerate silica gel. System performance is evaluated in terms of moisture removal mass and thermal COP. Influences of major parameters on system performance are tested and analyzed under Shanghai summer conditions. It was found that system performance is affected significantly by cycle time between dehumidification and regeneration, and optimal cycle time is 600 sec under test conditions (98).

Y. Jiang et al. have been experimentally set up built to test and compare the dynamic performance of SGCHE and CCHE. Influences of main operation parameters, including water temperatures and inlet air conditions, on system performance are analyzed in terms of average dehumidification capacity (D_{avg}) and thermal coefficient of performance (COP_{th}). Experimental results show that CCHE has better dehumidification performance compared with SGCHE. In addition, precooling before dehumidification is advantageous to both D_{avg} and COP_{th} (99).

In a humid tropical climate, Techajunta et al. presented the performance of a desiccant dehumidification system. The silica gel is used in an integrated desiccant collector with light bulbs to simulate solar radiation and forced airflow through a bed dehumidifier. Experimental results indicated that the solid desiccant could operate for the air dehumidification (adsorption process) at night and the regeneration (desorption process) in the daytime. The desiccant column is also widely used in the process of dehumidification (100).

The design analysis of a two-tower, silica-gel dehydration unit in the drying process of natural gas was presented by Gandhidasan et al. The effects of various operating parameters on dehumidification are discussed. The operating pressure of the dehumidification system increases, the silica-gel mass required decreases. The higher the regeneration temperature, the smaller are the required quantities of the hot gas (101).

Moreover, the theoretical and experimental study of a solid desiccant-packed bed dehumidifier on the transient adsorption characteristics was described by Hamed. The adsorption rate is a high value for the first time and decreases continually until the saturated equilibrium condition is reached. Several desiccant column configurations have been used, including solid packed bed, multiple vertical beds, radial bed, and inclined beds (102).

Kabeel investigated the performance of a multilayer (eight-layer) packed bed dehumidifier with the effect of design and operating parameters by theoretically and experimentally studied. The result of inlet air humidity and velocity on the adsorption process for each bed layer is analyzed. Moreover, the effect of inlet temperature on the desorption process is also examined. Increasing a bed length decreases the humidity of the exit air but increases the pressure drop (more power consumption). The adsorption model can be used to predict the optimum bed length (103).

Furthermore, Awad et al. reported the radial flow bed of the solid desiccant dehumidifier. The bed under investigation is radial flow with a cylindrical shape. Five experimental test units of hollow cylindrical beds with different values of diameter ratio (outside/inside) are used. Results show that the pressure drop in the radial bed is too small compared with the vertical bed. Moreover, the increase in diameter ratio increases the pressure drop within the bed and increases the adsorption capacity for short operation periods (104).

Ahmed et al. reported the evaluation and optimization of the desiccant wheel performance. A numerical model is developed to study the effect of the design parameters, such as wheel thickness, wheel speed, regeneration to adsorption area ratio, or wheel porosity, and the operating parameters, such as airflow rate, inlet humidity ratio the air, of regeneration air temperature.

Moreover, Nia et al. presented the modeling of a desiccant wheel using for dehumidifying the ventilation air of an air-conditioning system. MATLAB Simulink calculates the simulation of the combined heat and mass transfer processes to predict the temperature and humidity of outlet air and optimize the speed of the wheel dehumidifier. The temperature, humidity ratio, and airflow rate are the significant effect parameters on the performance of the desiccant dehumidification processes (105).

Hamed et al. studied the transient adsorption-desorption characteristics of silica-gel particles in fluidized beds experimentally. A simplified analytical model with isothermal adsorption assumption is developed. The experimental measurements evaluated the transient values of the mass of adsorbed water in the bed, rate of adsorption, and water content in silica-gel particles. The maximum decrease in air humidity occurs at the beginning of operating time, and the adsorption rate increases with the increase in the inlet air humidity (106).

3.3 Performances of desiccant dehumidification

A clear understanding of the variables that affect the performance is essential to maximize the desiccant system performance and proper sizing. Eight key parameters affect the performance of the desiccant. The air expected to dehumidify before entering the room is called process air. Reactivation air is used to regenerate desiccant after the surface is humid from adsorbing a lot of water. These parameters include:

- Process air moisture
- Process air temperature
- Process air velocity through the desiccant
- Reactivation air temperature
- Reactivation air moisture
- Reactivation air velocity through the desiccant
- Amount of desiccant presented to the reactivation and process airstreams
- Desiccant sorption-desorption characteristics

In any system, these variables change because of weather and variations in moisture load; moreover, each parameter's exact effect depends on the type of desiccant dehumidifier. Discussing desiccant dehumidifier performance must be made on the fundamental assumption at the start that the dehumidifier is operating at equilibrium. In other words, the total energy on the process side is balanced by the energy on the regeneration side. If the system is not in equilibrium, desiccant dehumidification will not perform in an easily predictable manner. Uncontrolled airflows and temperatures tend to the system are not in equilibrium.

4. History and development of thermoelectric devices

In 1822-1823, scientist Thomas Seebeck first discovered the phenomena that are the basis for today's thermoelectric industry. Seebeck found that a temperature gradient across the junctions of two dissimilar conductors produced an electrical current that would flow through these conductors. He continued this work investigating numerous materials, including some that we now call semiconductors, and arranged them to produce their electrical conductivity and what would become known as the Seebeck coefficient. Today, the Seebeck coefficient is expressed in microvolts per Kelvin. It is now known that what Seebeck observed was due to an electric current flowing in the circuit that he created, not a magnetic effect. Seebeck was the first to discover the thermoelectric effect.

In 1843, Jean C. A. Peltier discovered that the passing of electrical current through two dissimilar electrical conductors caused heat emitted or absorbed at the materials' junction. It was only after mid-20th Century advancements in semiconductor technology that practical applications for thermoelectric devices became feasible. We can now produce thermoelectric "modules" that deliver efficient solid-state heat-pumping for cooling and heating (see **Figure 9** and **Figure 10**). Many of these units can also generate direct power in particular circumstances (e.g., conversion of waste heat). New and often elegant uses for thermoelectric units continue to be developed each day (107).

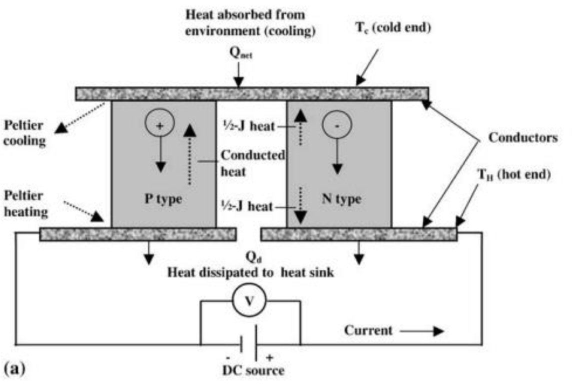

Figure 9 Schematic diagram of thermoelectric module operation in cooling mode

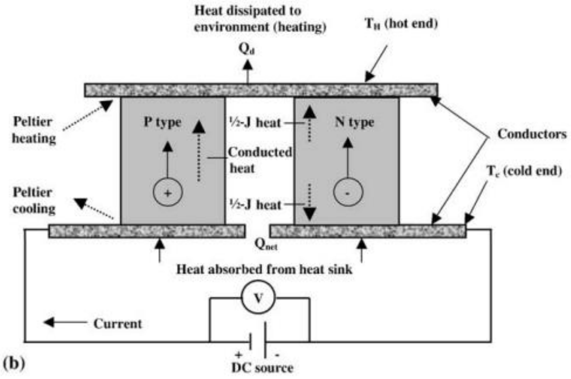

Figure 10 Schematic diagram of thermoelectric module operation in heating mode

In 1851 Lord Kelvin (William Thomson) found a relationship between the Seebeck and Peltier findings. Lord Kelvin predicted the existence of a third thermoelectric effect, which he observed experimentally.

In 1909 and 1911, Altenkirch (108) presented a TE power generation and TE refrigeration theory. He further showed that suitable TE materials should have a large Seebeck coefficient (S), low thermal conductivity (kTe), and high electrical conductivity (σ). These properties were combined into a value called the figure of merit (Z), defined as follows

$$Z = \frac{S^2\sigma}{\lambda} \qquad (32)$$

Although TE materials' favorable properties were well known, Seebeck's work with mineral semiconductors was overlooked while the emphasis of research remained on metals and metal alloys. In metals, the ratio of thermal conductivity to electrical conductivity is essentially a constant. This limits the potential for advances in the performance of metals as TE materials.

The advent of synthetic semiconductors in the late 1930s launched a renewed interest in TE. Maria Telkes at the Westinghouse Research Laboratories made a thorough study of the PbS-ZnSb couple and constructed a TE generator that operated with a thermal efficiency of about 5 percent. These new synthetic semiconductors possessed a Seebeck coefficient of 100 uV K^{-1}, 10 uV $K^{-1,}$ or less for metals. Then around 1949, Ioffe developed a list of semiconductor thermoelements (107).

Research into compound semiconductors for transistor applications in the 1950s resulted in materials with improved thermoelectric properties. In 1956, Ioffe showed that the ratio of thermal to electrical conductivity could be reduced if the TE material is alloyed with an isomorphous element. Research laboratories in the U.S. undertook a tremendous survey of materials that discovered materials with an even higher merit figure.

It was not clear that the ratio of thermal to electrical conductivity is more significant than that in metals in semiconductors. Soviet interest in the subject continued. Research in compound semiconductors resulted in new materials with improved TE properties. Around 1960, over one hundred companies were active in TE research and were trying for results in cooling performance equal to that of the Freon compression cycle development. In 1959 Zener predicted TE materials would be developed for such systems. This prediction was incorrect, and although there has been a gradual increase in TE material properties, it has fallen well short of Zener's expectation.

4.1 Thermoelectric introduction process

The details of Seebeck were described by using the discovered name. Moreover, the theory was improved by scientists and engineering. However, the thermoelectric is divided into two operations depending on workflows, such as thermoelectric power-producing and thermoelectric cooling. Both the power and the cooling module were usefully considered based on the physical structure.

Thermoelectric cooling is used for temperature production that is mainly required. However, the operation was not different from the thermoelectric module but reversed working. The power module used different temperatures on each side, transforming to current electric. This research used thermoelectric cooling type for the experimental that suited in designation and requirement.

The thermoelectric cooling modules had processing shown in **Figure 11**. The first section gave electric current from the power supply into positive and negative of thermoelectric. Inside thermoelectric consisted of P-N junction that actioned with electric current obtaining. Thus, the temperature difference occurred on both sides (Hot side and cold side). Therefore, the current electricity had necessary for the thermoelectric cooling type. High electric current density affected the temperature difference between both sides.

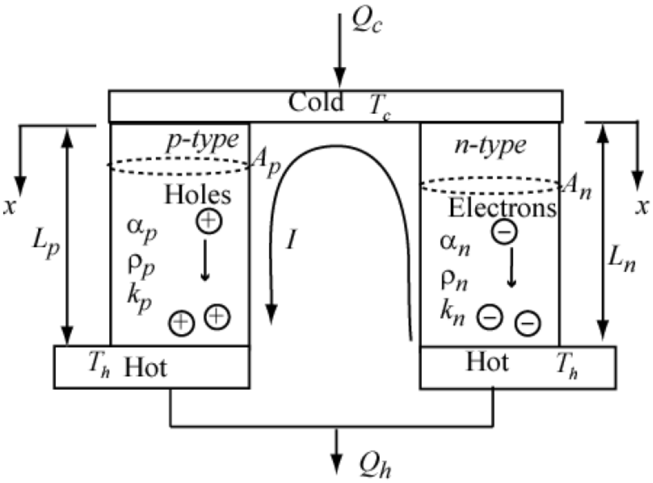

Figure 11 Thermoelectric cooling inside with P-N type

4.2 Benefits of thermoelectric devices

The choice of a cooling technology will depend heavily on the unique requirements of any given application. However, thermoelectric (TE) coolers offer several distinct advantages over other technologies, as; (107)

- Thermoelectric devices have no moving parts and, therefore, need substantially less maintenance.
- Life testing has shown the capability of thermoelectric devices to exceed 100,000 h of steady-state operation.
- Thermoelectric devices contain no chlorofluorocarbons or other materials that may require periodic replenishment.
- The direction of heart-pumping in a thermoelectric system is fully reversible. Changing the DC power supply's polarity causes heat to be pumped in the opposite direction-a cooler can then become a heater.
- Precise temperature control to within ±0.1 °C can be maintained using thermoelectric devices and the appropriate support circuitry.
- Thermoelectric devices can function in environments that are too severe, too sensitive, or too small for conventional refrigeration.
- Thermoelectric devices are not position-dependent.

Due to all the above advantages, thermoelectric devices have found very extensive applications in wide areas, such as military, aerospace, instrument, and industrial or commercial products, in the past decade. According to the working modes, these applications can be classified into three categories: coolers (or heaters), power generators, and thermal energy sensors. The details are in the literature review.

5. Thermoelectric dehumidifier

Thermoelectric dehumidifiers come under the category of dehumidification via cooling surfaces without the use of any refrigerant. The thermoelectric effect is well known for generating electricity using temperature difference as a driving force (109). Thomas Seebeck, in 1821 discovered that whenever there is a temperature difference between the two dissimilar semiconductor materials, an electric current is generated due to the electromotive force by the movements of electrons and holes in that material. A few years after this, Jean Peltier explained that when the same process is reversed, we can produce a temperature difference by applying a voltage across the junction of two dissimilar semiconductors. In short, whenever a current is supplied to the junction of the two different semiconductor materials, one side of the junction starts absorbing heat while the other side rejects heat. Later, William Thomson (Lord Kelvin) reported the Thomson effect quite similar to the Peltier effect. Thomson effect was related to the electromotive force between two parts of the single metal at different temperatures. This explains that whenever a thermoelectric element fulfills both of these requirements along its length depending upon the direction of the current, heat is either absorbed or rejected from the thermoelectric element (110). The thermoelectric module enables the practical applicability of thermoelectric technology in dehumidifiers. It consists of several p-type and n-type semiconductors known as thermoelectric pairs, connected electrically in series and thermally in parallel (111). It contains copper (used as a conductor) to connect the semiconductors and ceramic plates to cover the overall thermoelectric pairs. Bismuth Telluride semiconductors are used in general for this purpose. However, in recent years various new materials with better performance have been reported (112). There are two majorly reported applications of the thermoelectric module, the thermoelectric coolers which are based on the Peltier effect, and thermoelectric generators (Seebeck effect) (113). Many prototypes based on both applications have been reported. The thermoelectric dehumidifier is based on thermoelectric cooling. It uses the TEC's cold surface for condensing the moisture present in the moist air for either humidity control for human comfort or water generation from the atmosphere, as shown in **Figure 12**.

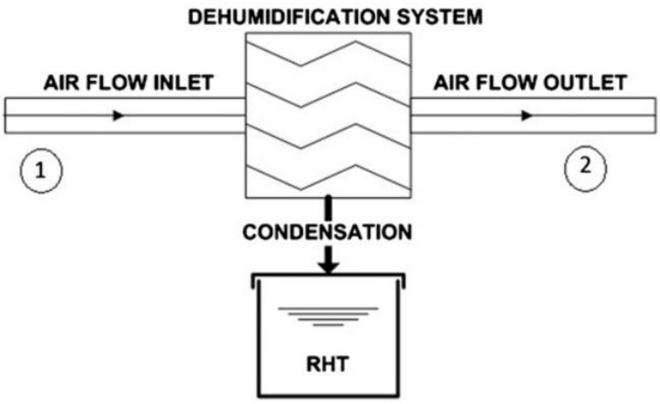

Figure 12 Principle of thermoelectric dehumidification

5.1 Thermoelectric dehumidifier prototypes

The prototype of the thermoelectric dehumidifier was reported in the year 2002. The year-wise discussion of the prototypes is presented in this section. In 2002, J.G. Vian designed and built a TED prototype for an alternative to the conventional vapor compression cycle-based dehumidifier (114). A comparison of the thermoelectric-based dehumidifier and the traditional dehumidifiers was presented. The low power (100 W) prototype consists of two stages for dehumidification as shown in **Figure 13(a)** with two TEC modules, one in the first stage and another in the second (**Figure 13(b)**). Heat sinks were used at the TEC modules' hot and cold sides, and axial fans were present at the system's inlet and outlet. The final dehumidified air before the outlet is passed through the second stage's heat sink to enhance heat transfer from the system and improve the prototype's overall performance. The detailed schematic with a specification of every part and stage is shown in **Figure 13(b)**. The air passage at different thermal stages is explained in **Table 6**.

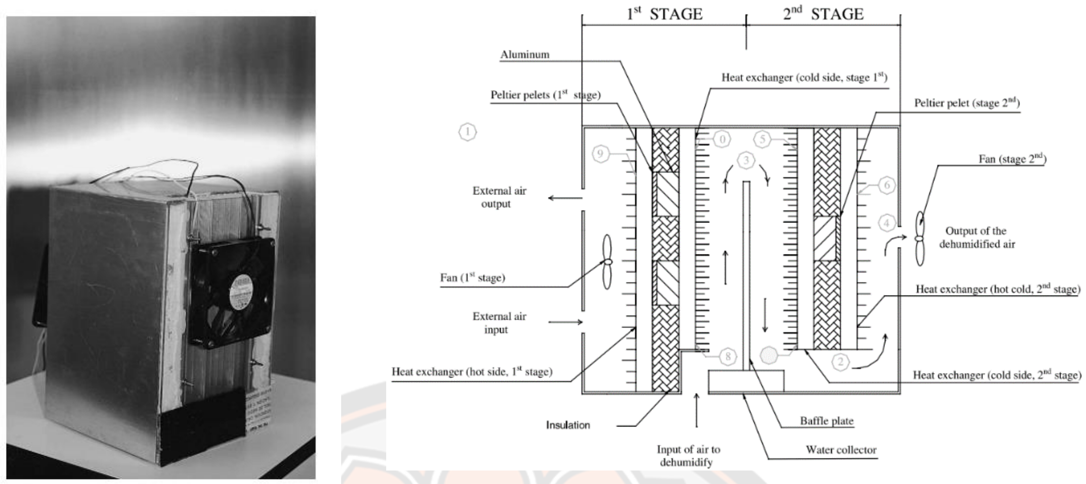

(a) **(b)**

Figure 13 TED prototype (a) and its schematic (b)

Table 6 Different thermal stages of air inside the dehumidifier

Sensor no.	Temperature	Sensor no.	Temperature
0	Cold dissipation 1st stage, top	5	Cold dissipation 2nd stage, top
1	Ambient	6	Hot dissipation 2nd stage
2	The air passing through 2nd stage	7	Cold dissipation 2nd stage, bottom
3	The air passing through 1st stage	8	Cold dissipation 1st stage, bottom
4	Exit	9	Hot dissipation 1st stage

The prototype was built and optimized by considering the heat transfer. The temperature changes in the system were evaluated through an electrical analogy. The system optimization was based on the predicted values of the parameter by the simulation. It was compared with the experimental values and was found to be very similar. Hence, the obtained results were compared with the simulation results for both stages separately. It was found out that the first stage results were similar;

however, due to phase change occurrence, results for the second stage had substantial differences. The COP and mass flow rate were plotted with different inlet air conditions, i.e., different values of humidity and ambient temperature. Thus, the optimized computational COP obtained was 0.8, which lies in the lower range of COP (0.7 to 1.3) offered by vapor compression-based dehumidifiers. This research gives a new direction to applications of thermoelectric technology. However, the prototype faces challenges in design aspects. There are no specific reasons for having two prototypes; however, it increases the prototype's size and results in less contact time between the moist air and cold surface.

Moreover, analysis related to water produced due to dehumidification could have been related to TED parameters. Heat rejection is a very important factor for TEC systems, for which the use of an extended surface is preferable. However, not much attention was given to the extended surfaces on the hot side by the authors, which negatively impacts the prototype's performance. After a few years, Charnwit Udomsakdigool et al. considered that the heat sink directly affects the thermoelectric module's cooling capacity (115). A new heat sink design with a rectangular fin array was proposed, and experiments were performed to obtain an optimized distance between the fin and fans. This work was broadly divided into two parts. In the first part, the pre-experimentation was performed to optimize the heat sink parameters, and the fan was used for heat rejection at the hot side. In the second part, the designing and performance evaluation of the prototype with varying ambient conditions was done. The pre-experimentation setup is shown in **Figure 14**, where a rectangular fins' array, vertical duct with the ventilation fan, and the plate heater connected with the voltage regulator are present. Here, the plate heater was acting as the hot side of the thermoelectric module. The various operating/testing conditions, such as distance between fan and fins, the fan speed, and voltage variation for the plate heater, were analyzed. The optimized distance between the fan and the fins was 30 mm for 200 W power input and 12 V of fan voltage. However, for the 40 mm distance between fan and fins, 300 W power input and 24 V of fan voltage were required. It shows that the hot side's maximum heat dissipation was obtained when the distance between fan and fins was 40 mm. Further, optimized values of Nusselt number (N_u) and Reynolds number (R_e) were found maximum at this point. Plots for every case were plotted for

5 min of the time interval, and they showed similar patterns of decrease in the temperature of the hot side with an increase in distance. With this optimization, fin efficiency was obtained as 95%.

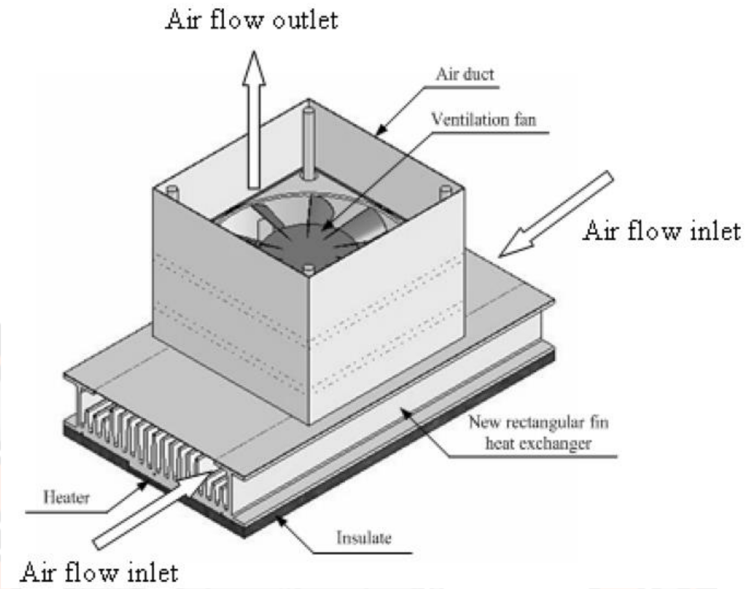

Figure 14 Pre-experimentation setup of rectangular fins array and fan over a plate heater

Based on the results obtained by the pre-experiments, a small TED prototype was built. It had a vertical rectangular fins arrangement with two thermoelectric modules shown in **Figure 15(a)**. Likewise, it can be seen in **Figure 15(b)** that there is free convection on the cold side, and the water condensate can be collected in the water tray at the bottom. The results for TED showed that the hot side and cold side temperatures get constant after 20 minutes. The dehumidification rate and COP obtained by the prototype's tests were 18.9 g and 0.88, respectively. Thus, this article only prioritized heat rejection from the hot side and explained performance aspects relating to that. However, the report also explained fan and hot side fins for any TED prototype. Other depending parameters relating to the cold side of thermoelectric modules were lacking in results and discussion. One of the significant parameters is the input power given to the thermoelectric modules, which was not mentioned in the article (115).

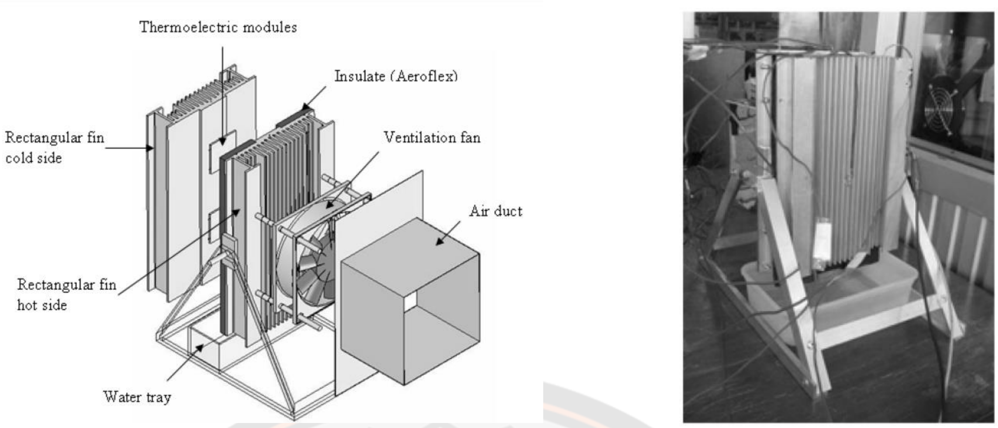

(a) **(b)**

Figure 15 (a) Prototype design depicting each part and (b) proposed TED

A small-scale low powered TED was built, and its performance was experimentally evaluated in 2010 by Wang Huajun and Qi Chengying. The authors gave profuse attention to the studies related to input power variation (116). An essential part of their work showed the relationship between the input power to the TED and its COP. **Figure 16(a)** and **Figure 16(b)** shows the experimental arrangement of the TED unit. The experimental unit is made of organic glass plates of dimensions 400×400×400 mm to serve as a small cube-shaped cabinet for tests. A TEC-12706 with two rectangular fins on both sides was mounted and had variations in input power. A cooling fan was attached along with the fins on the hot side for sufficient heat rejection and thereby efficient operation of TEMs. The results showed variation in cabinet temperature and relative humidity. Since pre-humidified air was supplied in the cabinet, relative humidity showed a significant drop during dehumidification from its initial values over time. The hot and cold side fin temperatures reached a steady state in the module after 10 to 12 minutes.

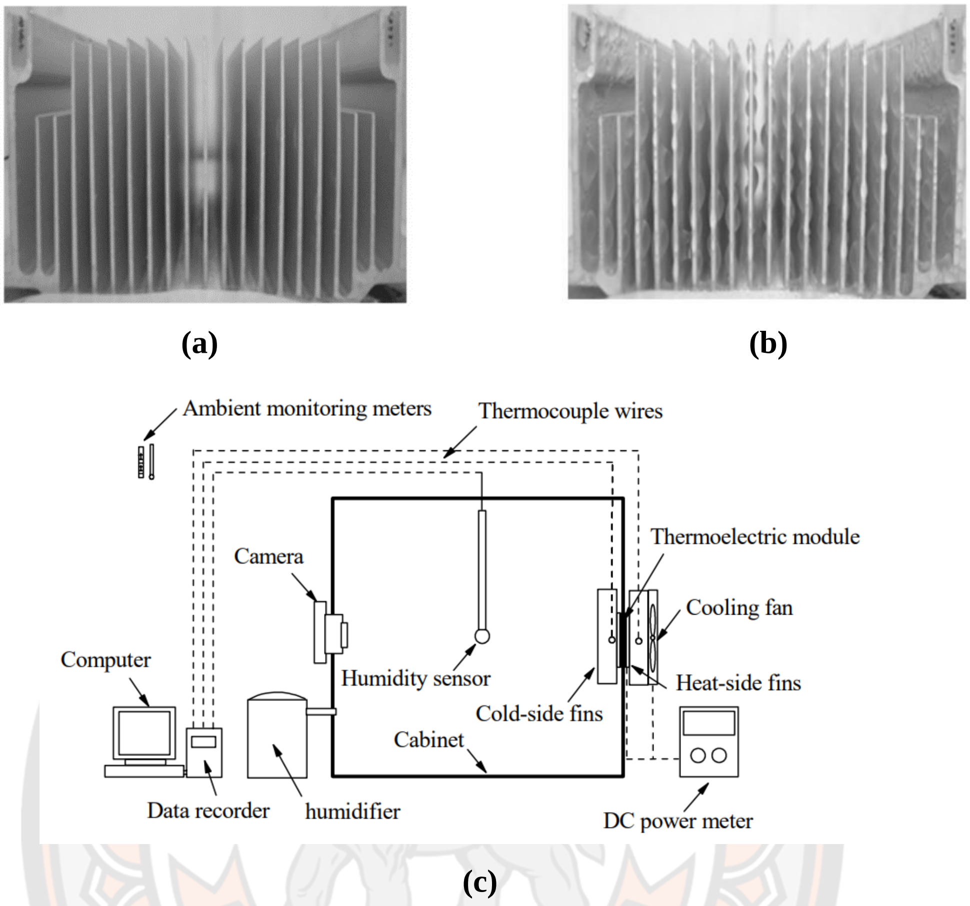

(a) **(b)**

(c)

Figure 16 Cold side fins (a) before, (b) after dehumidification process, and (c) schematic for the experimental setup of TED

The study described the dehumidification processes with an enthalpy-humidity diagram (**Figure 17(a)**). In **Figure 17(a)**, the process A to B for cooling and dehumidification for a time period of 44 min showed a very little drop of relative humidity from 98 to 90%. However, process B to C was for the isothermal dehumidification process. Strong dehumidification was experienced for 144 min, which led to relative humidity dropping from 90 to 40%. The variation of COP with an input power of the thermoelectric module in **Figure 17(b)** shows a rapid increase initially. It attains a peak value after 100 to 120 min and then drops quickly to almost the same level. The highest peak for the COP (0.32) was obtained at an input power of 6 W in a minimum time for dehumidification. Thus, stating the optimum value for input power as 6 W for the prototype. The average COP and dehumidification rate for the prototype at input power 6 W was 0.17 and 0.005 g min^{-1}, respectively, higher than the values for prototypes reported earlier.

Although the research claimed a low input power for TED, the prototype's final output performance was still inferior to conventional dehumidifiers. One of the intriguing points that set them back is the adhesion forces between water and cold side fins, which the authors mention. Therefore, the cold fins have a layer of water over the fins, as shown in **Figure 16(a)**. This layer of water causes a decrease in heat transfer between the moist air and cold side fins. Optimization of the design of the prototype was implemented to enhance the performance of the TED. The number of thermoelectric modules present in the prototype limits the dehumidifier's cooling surface, which eventually lowers the cooling potential. Some of the possibilities for further improvement can be dwelled by appropriate material selection for extended surfaces.

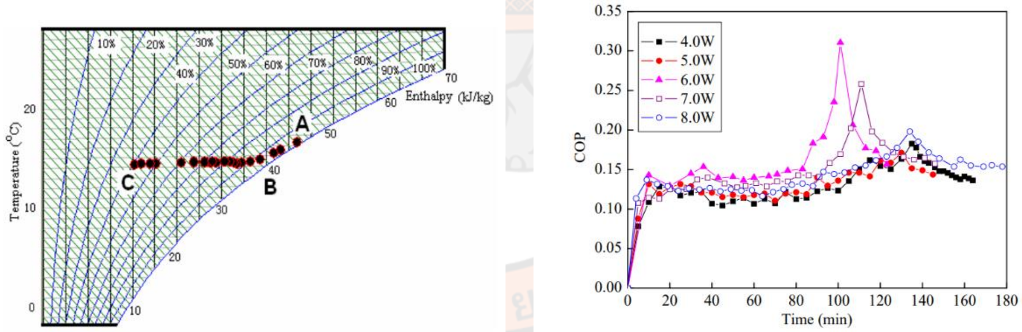

(a) **(b)**

Figure 17 The dehumidification process described in an enthalpy-humidity diagram (a) and variation of COP with time (b) for different input power supplied to TEM

An attempt for the same was made by Raghied Mohammed Atta, who introduced a solar-powered prototype and used thermoelectric technology for dehumidification (117). The system consisted of a solar cell unit worth of power up to 120 W, used to power three thermoelectric modules. Furthermore, storage batteries can store the excess amount of solar energy, and the system could be used after daylight. A fan first pumped the moist air to TEM's hot side to increase its temperature before going to the cold side. There are very nominal heat sinks of aluminum used on both sides, and it helps in heat rejection from the hot side. The condensed water from the bottom of the system (**Figure 18(a)**) was collected for further use. No such relevant studies have been performed for the performance or any depending parameters of TED. The article has been given attention, as a prototype was proposed and built for solar-assisted TED, as shown in **Figure 18(b)**, which could produce 1 L of water in the daytime.

(a) **(b)**

Figure 18 Schematic (a) and prototype (b) of proposed TED

Another solar-assisted TED for air dehumidification and freshwater generation was reported in the same year (118). The proposed system was integrated with a solar distiller for the enhancement of freshwater production. The performance-related analysis was performed for an amount of water condensed for current given to TEM. A case study at different locations with a variety of parameters was presented on a different note.

Consequently, based on the principle of thermoelectric humidification and dehumidification, a portable desalination unit was fabricated. The portability of the system was conceivable, as TEM offers a small size and less weight. Further, TEC was assimilated to provide a cold surface for condensation and a hot surface for heating feed water for humidification (119). The system consists of a cellulose pad humidifier, dehumidifier (cold side of TEC), aluminum water block at the hot side of

TEC for heat rejection, and a fan at the exit of the dehumidifier (**Figure 19(a)**). The detail of the data measurement system and humidifier is shown in **Figure 19(b)** and **Figure 19(c)**.

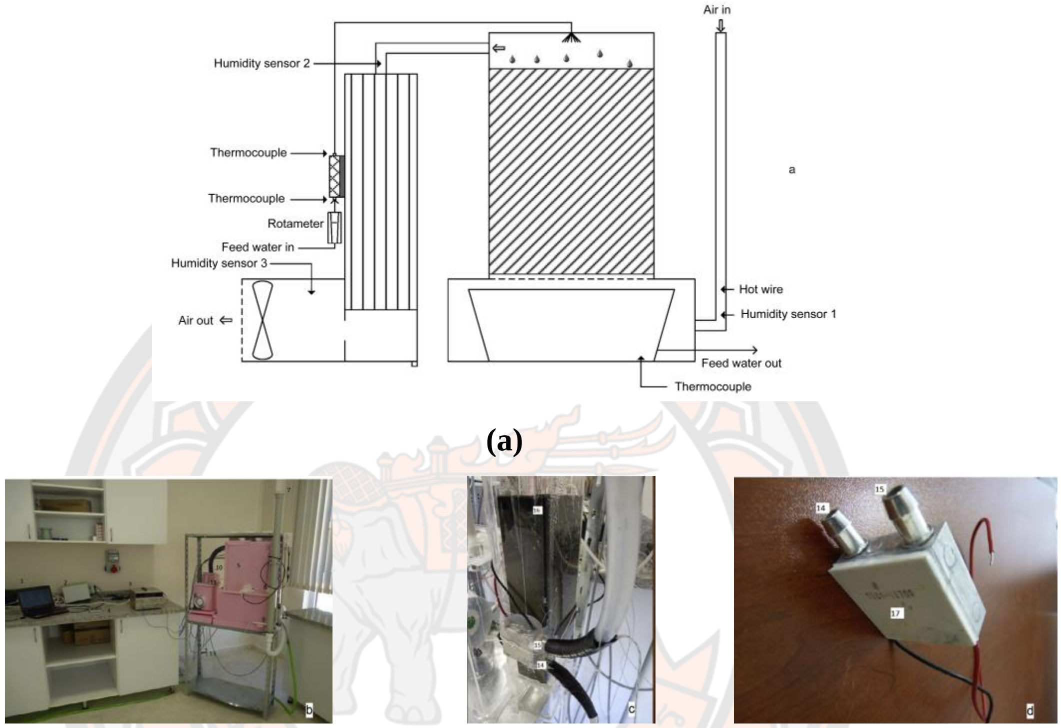

(a)

(b) **(c)** **(d)**

Figure 19 Experimental setup system

The feed water was first used for the heat rejection from the hot side of TEC. This added an ample amount of heat to the heated water, then spread over the cellulose pad humidifier by a spreader. The air was then forcefully injected into the system due to the fan and flowed from cellulose for humidification. The air and warm water were thoroughly mixed over the cellulose. Finally, the mixed air was passed through a TEC cold surface (dehumidification unit), and the water condensed was collected.

Further, the water block with inlet and outlet attached to the TEC, as shown in **Figure 19(d)**, was used to remove waste heat from TEC's hot side. Subsequently, the brine collected was drained out from the bottom of the humidifier.

The feed water mass flow rate and air velocity were varied from 0.5 to 2 L min^{-1} and 0.28 to 0.84 m s^{-1}, respectively. The TEC was supplied DC power of 110.26 W. As per these inputs, six sets of different experimental tests were performed. Initial results were plotted with a time duration of 9:00 AM to 5:00 PM for the inlet air conditions such as water temperature, air temperature, and relative humidity. Therefore, the relative humidity exhibited substantial variation.

In contrast, others showed minor variation. Successively, results for the same time duration were plotted for outlet conditions that are outlet air from the humidifier, dehumidifier, and water leaving water block. The highest COP attained was 0.78 when airflow velocity was at maximum (0.84 m s^{-1}) and the water flow rate at its minimum (0.5 L min^{-1}). The maximum clean water produced at different airflow velocities was 143.6 g. The research gave a novel way for the desalination unit's portability with thermoelectric technology but could not produce enough water for daily use. However, it showed the feasibility of the thermoelectric-based desalination unit for a freshwater generation. Various factors responsible for low COP and water production were mainly because of the smaller condensation area. However, using multiple TECs enhances both the cold side surface area for dehumidification and cooling capacity. Further, some more prototypes of TED are discussed, which were developed for water production from moist ambient air.

Joshi et al., designed a prototype of 10.6 kg and performed an experimental investigation for the portable thermoelectric cooler-based freshwater generator (120). Ten thermoelectric modules were used in a linear arrangement, making one side of the water generator's cuboidal structure. In contrast, the other three sides were made up of acrylic, making it a closed channel, as shown in **Figure 20(b)**. The modules of dimension 40×40 mm^2 were kept at a distance of 20 mm from each other. Internal and external heat sinks of surface areas 0.2 m^2 and 0.7 m^2 were placed on the thermoelectric module's hot and cold sides for efficient heat transfer at both sides. The Cooling fans and an extended surface are attached to the external heat sinks for better heat rejection. An axial fan was placed at the top end of the closed channel, where the moist air was sucked into the system. The arrangements of all these parts are orderly shown in **Figure 20(a)**. The moist air comes in contact with internal heat sinks in the 0.7 m long-closed cooling channel. The moist air gets dehumidified, and the water condensate obtained over the internal heat sink was collected at the bottom of the closed channel. The dehumidified air outlet was from the bottom. The actual TED prototype built by the authors is shown in **Figure 21(a)**.

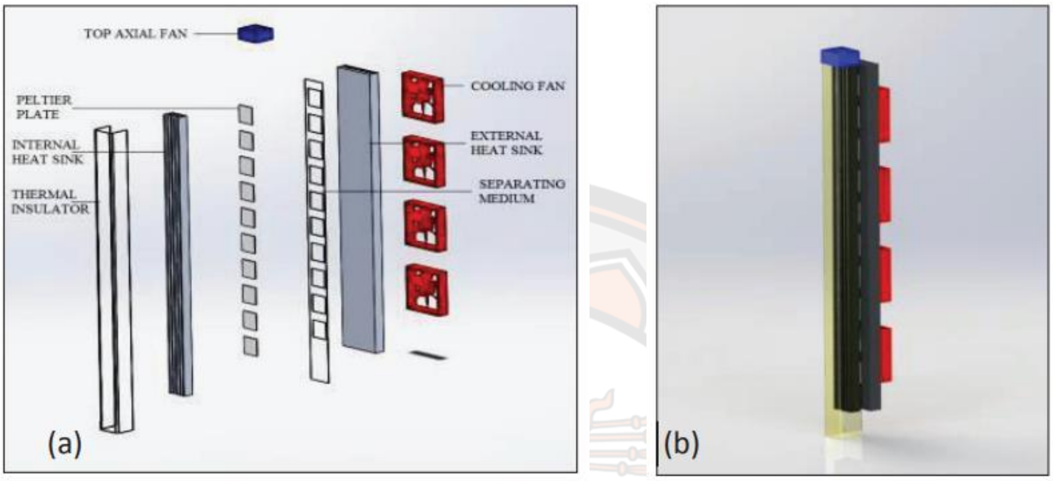

(a) **(b)**

Figure 20 Computer-based model of system (a) and schematic (b)

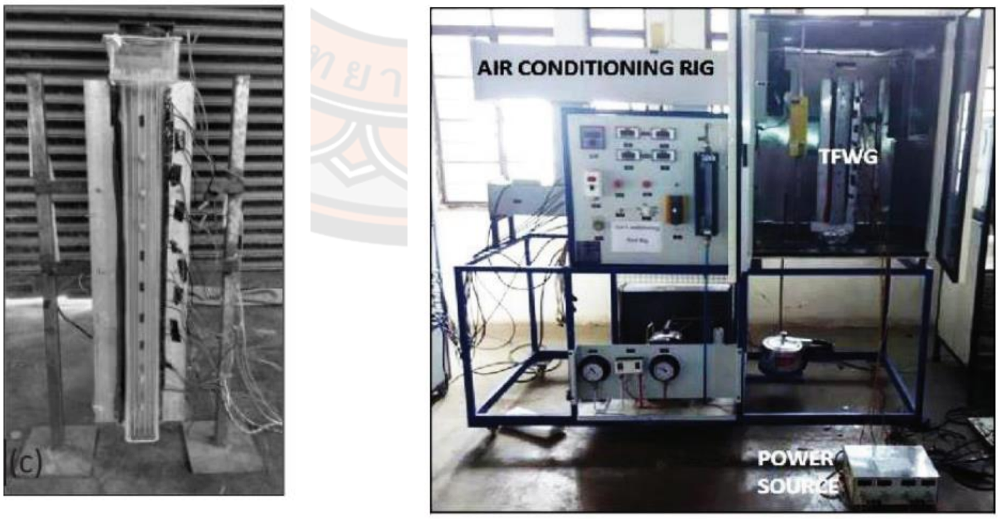

(a) **(b)**

Figure 21 Actual prototype (a) and experimental setup (b) for system

The experimental test rig (**Figure 21(b)**) comprised an air conditioning test rig for ambient air temperature and humidity control of the experimentation room, variable DC power source, and the freshwater thermoelectric generator. The effect of variation in mass flow rate, current, and relative humidity on condensed water was performed in the experimental investigation. Subsequently, the enhancement of the water generator was determined with the employment of internal heat sinks. The experimental procedure was carried out at an ambient room temperature of 30 ^{o}C for ten hours for each test. It was observed that air mass flow rate, relative humidity, and electric current were directly proportional to the water condensate. The effectiveness of the internal heat sinks was presented with and without the water condensate. An increase of 81%, i.e., from 45 ml to 240 ml, was observed. At 0.011 kg s^{-1} airflow rate and 90% relative humidity, the prototype had its maximum COP of 0.437. The research explicates the importance of extended surfaces at cold and hot sides of TEM by providing results with and without them. Although, instead of just giving the amount of water generated at the end of the experiment, water generation behavior could have been studied with time. The behavior could provide the sights for improvements in the water production of the prototype. The prototype's design optimization with multiple TEC module arrangements could provide more insights for enhancing the prototype on a different note.

In 2017, another prototype for a portable water generator was proposed with a more comprehensive study (121). **Figure 22(a)** shows the portable water generator is defined using two thermoelectric modules (thermoelectric coolers). It was designed and investigated experimentally for different inlet air parameters. An attempt was made to design a small prototype with less energy consumption to work at low airflow rates, as it had to be for portable use and light in weight (7 kg of the present prototype). The experimental setup is shown in **Figure 22(b)**, which has a humidifier, mixing chamber, air channel, and thermoelectric water generator.

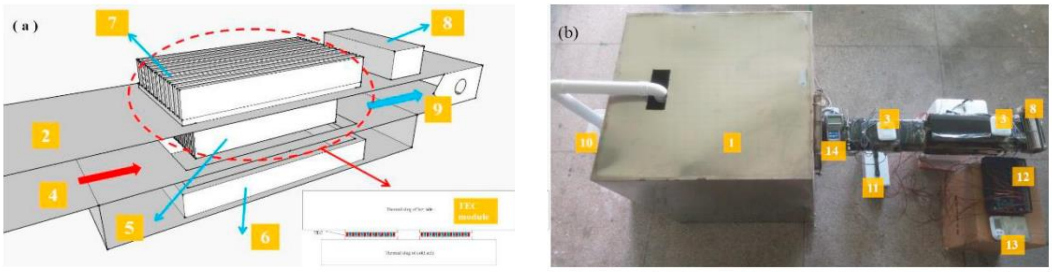

(a) **(b)**

Figure 22 The schematic of water generator (a) and the photo of experimental rig (b)

The experimental procedure of the water generated can be inferred from **Figure 22**. The humidifier and flow mixing chamber used with the cross-flow fan can control the inlet air with different relative humidity. The air then flows over TEC's cold side, and its temperature reaches the dew point temperature. Therefore, the condensate water can be collected in the pan present at the bottom. Fins are placed at both sides of the TEC module to enhance the heat transfer, and thermocouples measure the temperature. The experiment was solely based on obtaining water generation and condensation rates. The varying parameters taken were relative humidity and airflow velocity of the inlet air shown in **Figure 23(a)**, **Figure 23(b)**, **Figure 24(a)**, and **Figure 24(b)**. The maximum amount of water generated was 25.1 g h^{-1} with input power and condensation surface of 58.2 W and 0.216 m^2. Three different airflow rates were controlled by the cross-flow fan and measured by the anemometer.

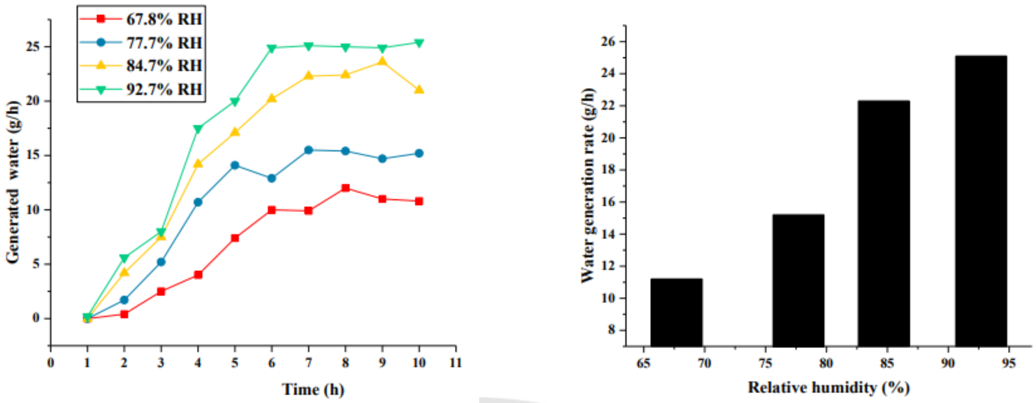

(a) (b)

Figure 23 Variation of condensed water with time for different values of RH (a) and Variation of water generation rate with relative humidity (b)

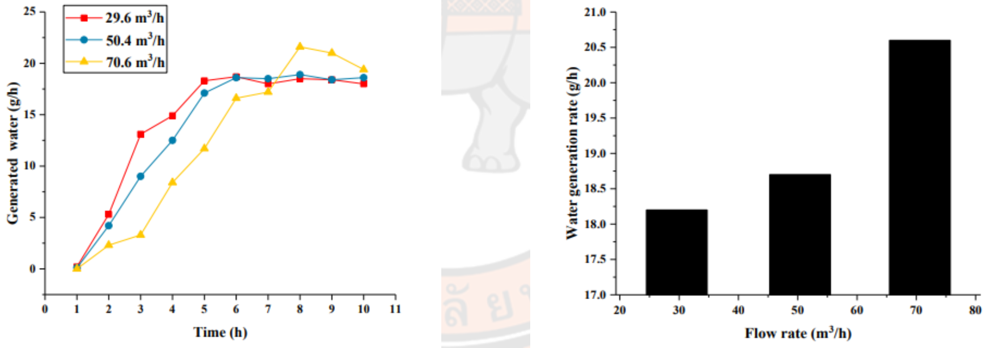

(a) (b)

Figure 24 Variation of condensed water with time for different air velocity values (a) and variation of water generation rate with flow rate (b)

It has been accounted that the water generation rate increases with an increase in either relative humidity or airflow velocity. Hence, the water generation rate increases with time. It was low at starting since gravity cannot overcome the adhesion of the water droplets with the fin surface. With an increase in relative humidity while keeping the other working conditions constant, there was an increase in air moisture. It decreases the temperature difference between the inlet air and its dew point, increasing the condensation rate. The water generation was higher for the cases of low airflow rates as compared to high airflow rates. The fin temperature gradually decreased with time and resulted in increased moisture content irrespective of airflow rates. Nonetheless, a decrease in condensation rate was observed due to the less contact time between the inlet air and the cold side surface. This was because of the low cooling capacity obtained by two TECs, as required by higher flow rates of inlet air.

A comparative study of performance with other TEC water generators was prepared to compare the consumed power, water generated, and condensation rate with different inlet air parameters. The portable water generator prototype was considered efficient for low relative humidity and less energy consumption (121). However, the optimization of the system design needs to be performed for a more efficient system. The surface material of cold side fins must have less adhesion with water, as this property of the surface exhibits dropwise condensation in the initial dehumidification stages. Furthermore, the number of TECs must be increased by taking care of the prototype's portable usability. The author has already mentioned making the prototype solar-assisted by using PV panels or solar cells. Therefore, a self-assisted solar-powered thermoelectric water generator can be attained. As heat rejection in TEC is of major concern; therefore, experimental analysis relating to the length of fins could be performed for a more efficient study regarding the thermoelectric-based water generator.

TED's design still had challenges to overcome for the arrangement and layout of components (TEMs, heat sink, and duct). Thus, in 2017, Yu Yao et al. anticipated a series of prototypes for design optimization and investigated them experimentally to enhance moisture removal rate (122). The prototypes were analyzed over structural parameters and tested using the orthogonal design method (123). The prototype had a straightforward design structure (122), as shown in **Figure 25(a)**. The TEMs were sandwiched in between the cold side and hot side heat sinks. Two cooling fans and one supply fan were located in front of hot side heat sinks, and cold side heat sinks, respectively. The supply fan must regulate the voltage to vary the inlet air velocity. This whole system was placed over a plate such that a water container below it collects all the condensate from the humid air, as shown in **Figure 25(b)**. The whole experiment was performed in a pre-humidified room to stabilize the relative humidity of the air. As there were many variables to observe in the final output, the experimental investigation was carefully designed. Hence, the orthogonal design method was used (124). It is considered a modern methodology for optimizing experiments by performing tests for various parameters in a single experiment with fewer experimental units. For the current prototype, 18 experiments were selected, each having one variable and two affecting factors to study the influence of structural parameters over moisture removal. Ten prototypes were designed for the experiment divided into four groups based on the layout of TEMs, air duct size, heat sink size, and number of TEMS.

A very keen observation was gathered in the article towards the TED operation in the winter seasons. It was regarding the frost formation over the cold side heat sinks. TED's overall performance degraded as the frost formed as a resistance for the heat exchange between air and cold side heat sink. Therefore, the enhancement of TED performance in the winter season was also investigated by considering the defrosting time interval. Consequently, the defrosting was performed by turning the fan voltage to 12 V for maximum air intake velocity and switching off the TEMs. There were two-time modes set subsequently; the long periods, used as 5 minutes after every 95 minutes, and the short periods, used as 3 minutes after every 27 minutes. Results were discussed concerning the classification of prototypes in different groups. Prototypes for experimentation were running for five hours, and condensed water was recorded on an hourly basis.

Table 7 Divisions of prototypes into groups

Groups	Structural Parameters	Prototypes
I.	Influence of layout design of TEMs	2B (Horizontal) 2D (Diagonal) 2E (Vertical)
II.	Influence of air duct size (Length and cross-section wise)	2F (Long cold air duct) 2G (Short cold air duct) 2H (Large cross-section area)
III.	Influence of heat sink size	2B (Same hot side and cold side heat sink area) 2J (Smaller hot side sink) 2I (Smaller cold side sink) 2G (Same hot side and cold side heat sink area)
IV.	Influence of no. of TEMs	1A (One TEM) 2B (Two TEMs) 4C (Four TEMs)

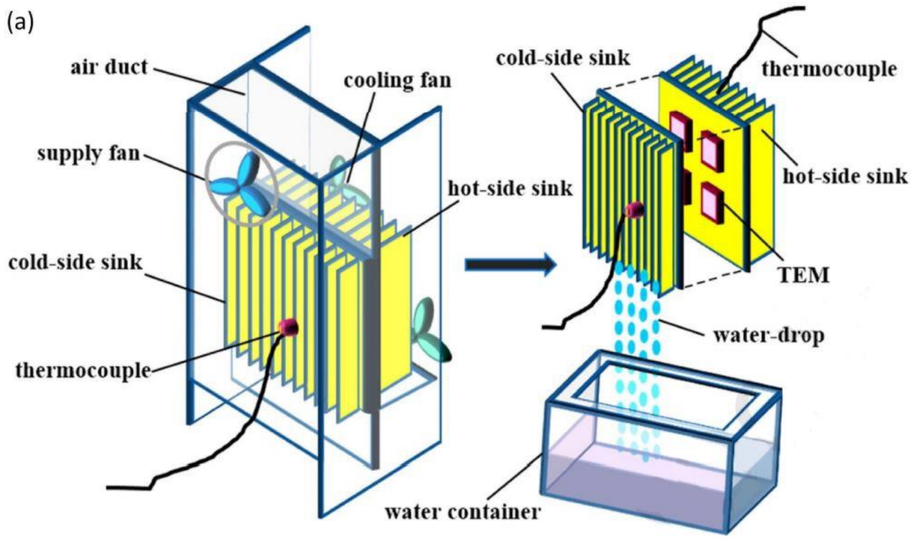

(a)

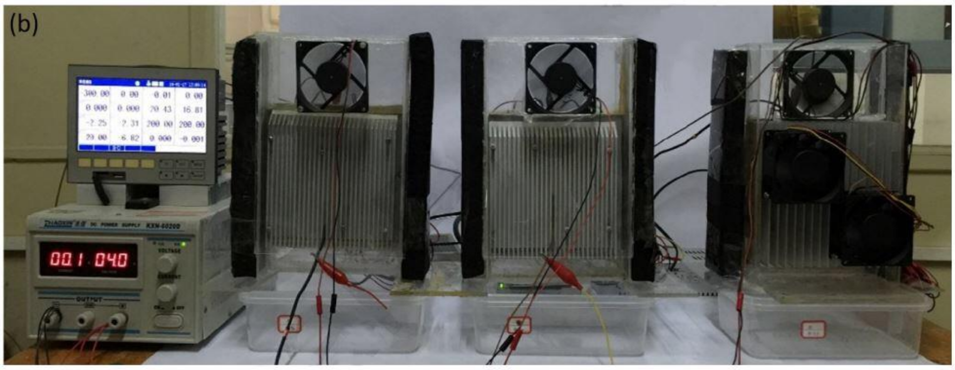

(b)

Figure 25 Schematic view depicted to view each part of TED (a) and experimental setup and data collector system (b)

The groups defined for the prototypes in **Table 7** (122) are well classified for variation in layouts of TEMs, air duct size, heat sink size, and number of TEMs. It was observed that the maximum moisture removal was obtained from the prototype using four TEMs. Thus, for further optimization of TED's performance, another prototype was proposed with novel configurations compared with four TEMs. The configuration of the novel configured prototype has quite a similar configuration to the one giving maximum performance. A significant difference was made in its design; the TEMs were sandwiched between the cold and hot sink in two parts, each consisting of two TEMs, as shown in **Figure 26(a)** (122).

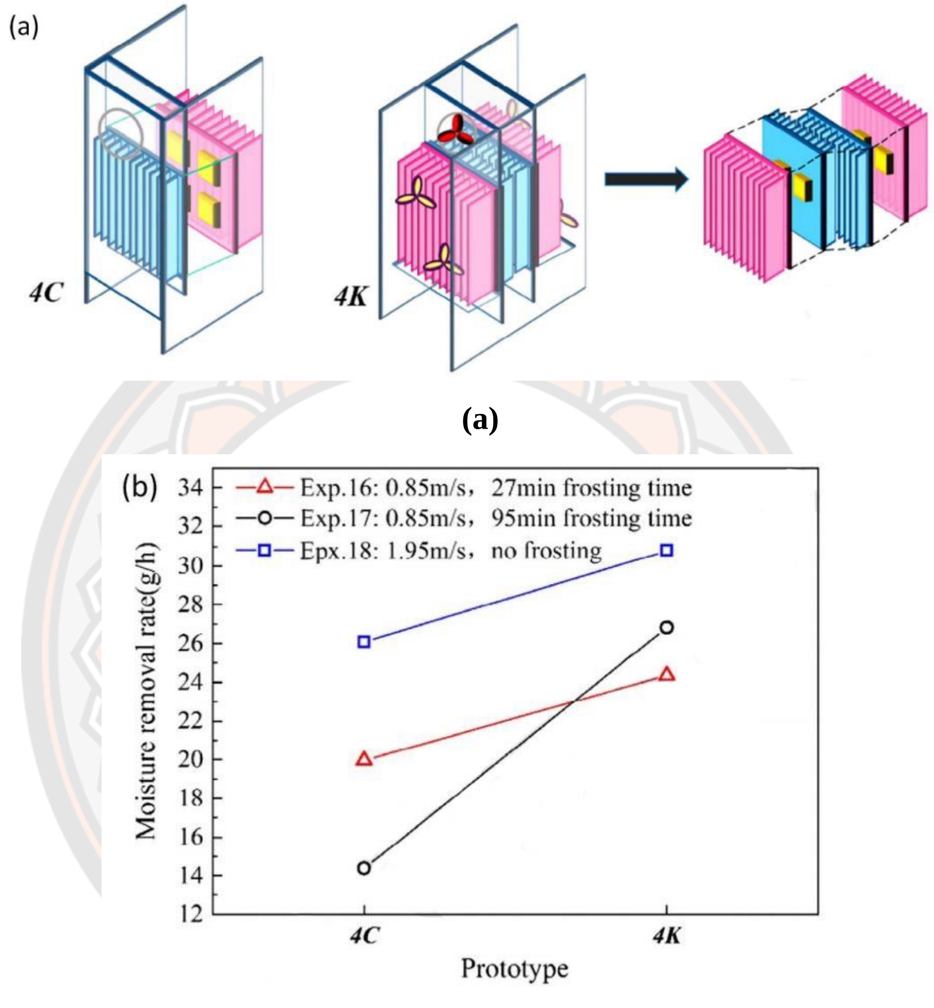

(a)

(b)

Figure 26 Final novel prototype (a) and comparing its performance with the best one observed from previous ones (b)

The comparison made under three conditions shows that moisture removal rates were better in the prototype with this design in frosting and non-frosting conditions (125). The heat transfer improvement from the cold and hot sides was made using two heat sinks on both sides. Thus, better heat transfer resulted in an ample increase in moisture removal rate (**Figure 26(b)**). For further optimization, experiments were performed for both frosting and non-frosting cases with a variation of airflow velocity and humidity ratio. Under non-frosting conditions, the optimal value for airflow velocity was 1.74 m s^{-1}. At this condition, the prototype had a moisture removal rate of 33.1 g h^{-1} and a COP of 0.75. However, for frosting conditions, it was found that frosting increases with a decrease in airflow velocity because of antagonistic effects over moisture removal rate. Correspondingly, the long frosting time condition dominated compared to the short frosting time for moisture removal rate. The temperature profiles of TEC's hot and cold sides were plotted against time, and the effect of airflow velocity was examined. From the temperature profiles, it can be deduced that the cold side's temperature increases with an increase in the airflow velocity.

In contrast, it initially increases and then decreases for the hot side. The research successfully improves the TED performance for both the summer and winter seasons. Further, a thorough optimization of design parameters was performed. However, it still could not attain COP in the upper range of the conventional dehumidifier because of the low COP of TEMs. Therefore, with better material availability for TEMs, the proposed system can hold efficient TED potentials in the market.

B.J. Li proposed a novel dehumidifier consisting of a combination of thermoelectric and desiccant techniques for dehumidifying in 2017 (126). The schematic and flow of air over the TEC's hot and cold sides is shown in **Figure 27(a)**. The prototype was designed for small-scale applications and consisted of thermoelectric coolers sandwiched between hot and cold side fins. The surfaces were coated with silica gel (desiccants) and a rotatable switchover plate shown in **Figure 27(b)**. Initially, the cold side fins are fetched with the incoming air, although it is saturated after a certain working time and requires desorption. Thus, a stepper motor was attached with the rotating plate for 180^0 rotations, exchanging the fins between cold and hot sides for desorption. Hence, desorption of saturated silica gel proceeded at hot side fins. The whole system was in a small cabinet; fans were present for forcing air on one end. The arrangements of all the parts are orderly, shown in **Figure 27(c)**. The system (**Figure 27(d)**) was placed in a relatively high humidity than outdoor humidity. The experiments were performed for the switchover time interval, thermoelectric power, and performance at different working conditions. The tests were carried out under typical working conditions at 34 ^{o}C temperature and 65% relative humidity. The switch over-analysis of moisture content with time was performed on both sides, and it was observed that for proficient performance of the prototype, time must be between 5 to 10 minutes. Thermoelectric power tests were performed with the current variation for hot/cold side temperature, moisture removal rate, and COP. The highest value of moisture removal rate and COP were obtained at 5 A. Under typical conditions, 34 ^{o}C and 65% RH, the prototype's efficiency was reported as 0.75 g (h W)$^{-1}$. The prototype's performance depends on both the cold and hot sides as it ensures the desorption of the saturated desiccants. Moreover, dehumidification's combinational technique gave an unprecedented way to tackle less cold surface area, which used to be the cause of a low efficient system.

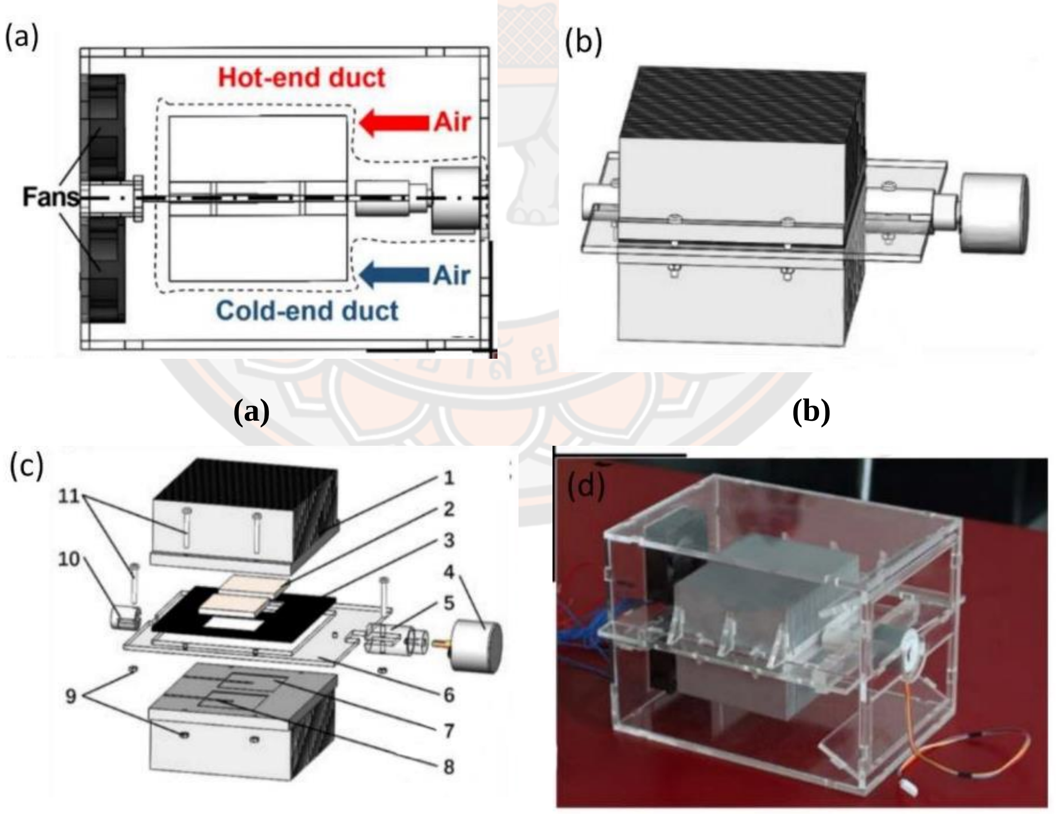

(a) (b)

(c) (d)

Figure 27 Schematic (a), structure of the prototype (b, c), and actual prototype (d)

Further, a water generator based on solar-powered thermoelectric technology (**Figure 28(a)**) was studied and simulated on MATLAB/Simulink (127). The system TEC-12706 (TEM) was powered by an 80 Ah battery and charged by solar cells of 50 W. The test's air conditions were in the range of 60 to 80% humidity and air temperature of 30 °C for the test location (Thailand). The results obtained from the experimental tests and simulations were compared for the air temperature range of 10 to 40 °C. It was found out that the results were quite similar at higher temperatures compared to lower air temperatures, where it showed notable variations. The Solartron SP-50 PV module was used for power generation at different irradiance; the surplus power was stored in the battery. The water production per day was ~0.2 to 0.3 L with a power consumption of 2.5 to 3.5 W, as shown in the experimental setup (**Figure 28(b)**). A little economic analysis inferred that it is an efficient way of water production in Thailand.

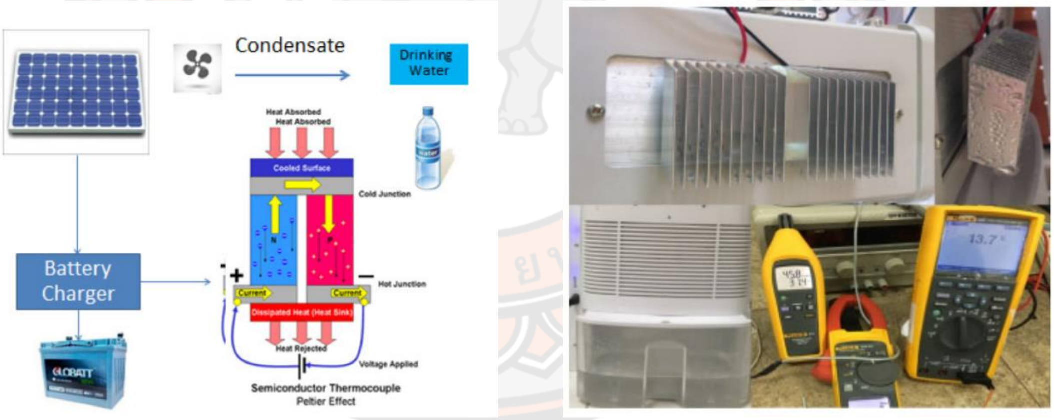

(a) **(b)**

Figure 28 Block diagram representation for water generator using the TED system (a) and experimental setup of proposed TED for validation of simulation work (b)

This was successively another study given for water generators by using thermoelectric dehumidification, especially for Thailand. However, an appropriate design for a portable thermoelectric water generator was not presented. A thermoelectric dehumidifier was studied theoretically and investigated experimentally to obtain an optimal cold sink temperature value (128). It has been noted that it directly relates to the latent heat absorption from the cold side. However, no study for optimization of cold sink has been reported. Researchers have reported that the optimization of heat rejection from the TEM does not optimize the latent heat absorption. The heat absorption on the cold side in TED occurs, firstly due to the temperature difference between ambient air and cold, and secondly, latent heat absorption. Here, water vapor is formed over the cold side surface. The latent heat absorption can be maximized by determining the ratio of latent heat absorption and total heat absorption.

In the theoretical study, the plots for the ratio of latent heat to total heat absorption rate and optimal cold sink temperature were given at different ambient temperatures, relative humidity, and heat transfer coefficients. It was found that the latent heat absorption ratio decreases radically after the cold sink temperature reaches 11 ^{o}C. Further, the optimization of latent heat absorption rate, total heat absorption, and latent heat absorption ratio was considered a function of cold sink temperature (129). The optimal cold side temperature was found by balancing heat absorption rates and heat exchange of the cold sink. The optimal cold side temperature was obtained at constant ambient air temperature values, power supplied, and relative humidity. However, the maximum energy efficiency for TED was determined at optimal cold sink temperature. With the increase in cold side temperature, latent heat absorption and total heat absorption were balanced. Thus, a maximum condensation rate was obtained at the cold sink's optimal temperature, which was 14 ^{o}C.

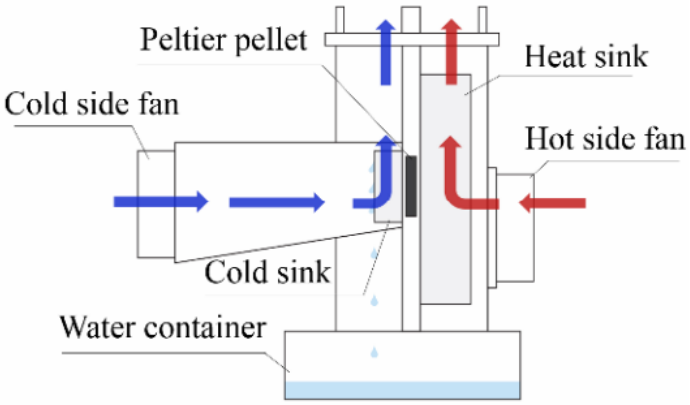

Figure 29 Schematic diagram of purposed TED

The prototype had a simple design (128) (**Figure 29**), having fans for airflow over the cold side duct and heat sink surface. A water container was used at the bottom to collect water droplets from the cold side. The water was measured every hour, and condensation rates were estimated. The variation of airflow velocity was obtained by varying the input power of the fan. The energy balance test was performed for the system at different cold side temperatures. The rate of condensation was evaluated with variations in cold sink temperature and atmospheric conditions.

Furthermore, the experimental and theoretical results were compared and quite promising for the condensation rate. However, the experimental and theoretical results differ with an increase in cold sink temperature. The maximum value obtained for condensation rate was 7.6 g h^{-1} at 15.6 ^{o}C of cold sink temperature. The results were close enough to the theoretical ones, and the maximum condensation rate was achieved at 14 ^{o}C. The small error was due to the water droplets adhering over the cold sink and the minor evaporation of the collected water (130). The COP of the TED was depicted experimentally with a variation of cold side temperature. The maximum COP was found at 14.1 ^{o}C of cold side temperature.

The condensation rate variation with ambient conditions was presented for two cases with variation in cold sink temperature. In the first case, the relative humidity was fixed at 57%. The two values of ambient temperature showed that with a decrease in ambient temperature rate of condensation increases. Additionally, the optimal temperature for cold sink gets marginally higher. In the second case, the ambient temperature was kept constant at 29 ^{o}C. For two relative humidity values, it was found that relative humidity has a more vigorous effect on condensation rate than ambient temperature (131). The difference between condensation rates increases rapidly with an increase in cold sink temperature after 7 ^{o}C.

Moreover, there was a significant increase in the optimal value of cold sink temperature with increased relative humidity. The change in cold sink temperature was theoretically evaluated with TEM specifications. It was found out that with an increase in temperature difference between the hot side and cold side, the amount of vapor condensed increases, and optimal temperature decreases. The research explains the importance of the cold side sinks and gives performance-based theoretical and experimental results for cold side temperature.

P. Rakkwamsuk et al. proposed a TED for dehumidification of indoor air in a building room. The prototype consisted of 4 TEMs (TEC-12708) for dehumidifying a test chamber of 1 m^3 volume (132). The whole system was divided into three parts: the thermoelectric cooler, test chamber, and water-cooling system, as shown in **Figure 30**. The TECs were connected in series, and the cold side sinks were placed in a duct. The test chamber had a nozzle-diffuser placed at the top for the inlet air entry by a blower. The cooling water system with a radiator fan and driving pump was used for heat rejection from the TEC's hot side. The analysis evaluated the electric current supplies to the TEM and airflow rates over the sinks. The effect of electric current at constant ambient conditions was evaluated for five current values, from 3.5 to 18.5 A. The cold side temperature was decreased to the least value of 9.5 °C at maximum current. Subsequently, the outlet water temperature at the heat sink increased. The cooling capacity and COP had opposite trends with the increase in electric current. The COP decreased to approximately 0.8 (a decrement of 115.9%) for a current value of 10 A. However, the cooling capacity increased by 55.78%, with a maximum value of 150.05 W at maximum current. Therefore, with a decrease in heat sink temperature, the effectiveness of the system increases.

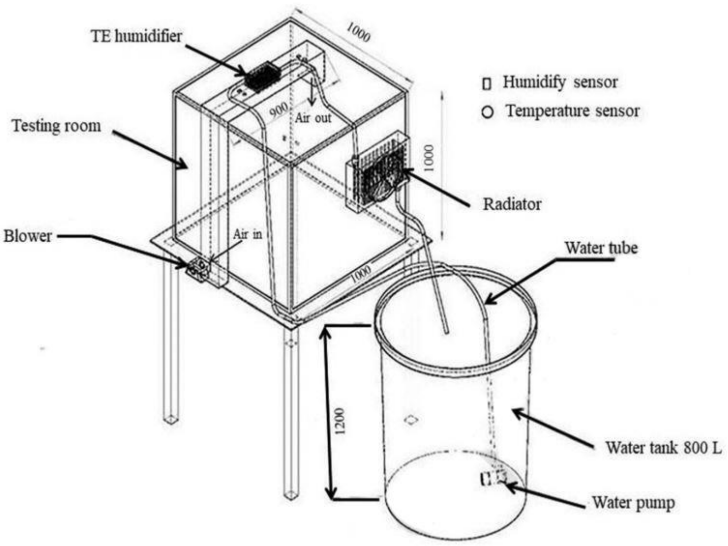

Figure 30 Experimental setup for proposed TED depicted in the schematic

However, the system's effectiveness decreases by 38.5% with an increase in the air mass flow rate. Due to a decrease in humidity ratio, there is a decrease in the contact time between air and cold heat sink at a high flow rate. A comparison study was prepared between the current system and a liquid desiccant. It was estimated that the current system's effectiveness was higher, whereas COP was lower. This is due to the small size of the prototype, which causes a low airflow rate. In the test chamber, 10 g of water was condensed in 200 min with COP and effectiveness of 0.41 and 0.62, respectively.

Amir Hossein Shourideh designed and constructed a small prototype for an atmospheric water harvester using TED to tackle pure water scarcity (16). The prototype was designed, and the model was studied and tested, considering water yielding as the main aspect. Further, different techniques for dehumidification were compared based on their performance. The design is shown in **Figure 31(a)** of the proposed model uses thermoelectric coolers (TECs) to cool the humid air, and it gets sucked into the system by intake fans.

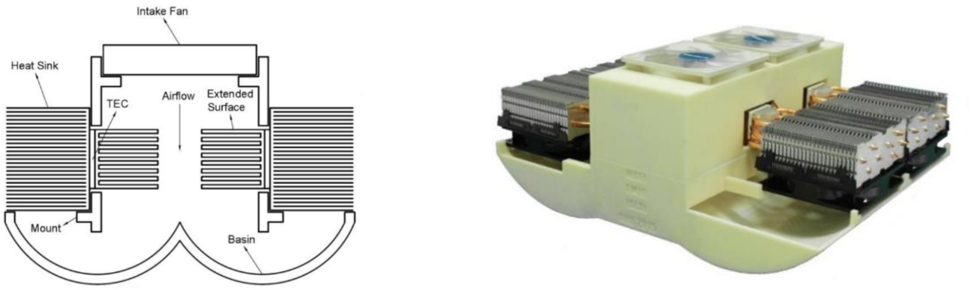

(a) **(b)**

Figure 31 2D schematic (a) and actual AWG prototype (b)

To increase the heat transfer and water generation rates, extended surfaces (fins) were present at both the cold and hot sides of the TEC modules (133). The dehumidified air was redirected towards the TEC module's hot side through their fins for heat dissipation. The design of the prototype was split into three parts (a) the TECs and their configuration, (b) the theoretical model for the water generation of the extended surfaces and their design, and (c) the housing design, fabrication, and assembly of the prototype. It was fabricated by a 3D printer using acrylonitrile butadiene styrene (ABS) plastic with dimensions of 43.56×34.25×17 cm (**Figure 31(b)**). Since the 3D printing material ABS is porous, it would be a diminution in water collection layers of superhydrophobic spray applied over the housing surface. It helps water droplets move towards the water collector smoothly. The bottom of the housing was already inclined by 2° for easy water flow into the collector opening.

A study was performed by varying the electric current of TEC, and the variations of cooling capacity and COP were reported. The cooling capacity increased with an increasing current and has its peak at the maximum value of current. However, the COP had its peak at about 1.5 A and decreased after that. The experimental tests were performed for two cases using four TECs differing in series and parallel connections. When all TECs were connected in parallel, higher system efficiency was achieved. Much emphasis was given to the design of cold side extended surfaces, an integral part of the prototype. The length of the extended surfaces was a very prominent parameter for the amount of water obtained. The method for optimizing extended surfaces given by Kılıç and Onat for wet rectangular fins was modified and used for the current study (134). The length of extended surfaces was chosen to be 8 cm based on several depending factors. The base of the fins was designed as per the TEC base area with a thickness of 2 mm. The larger the surface area of the TEC's cold surface, the higher the water generation rate. However, when it becomes long enough, then temperatures higher than the dew point make it dry and act against the condensation rate (135). **Figure 32** (16) plots the volume of water generation concerning the length of fins and their materials for one hour of operation. It is observed that increasing the length of extended surfaces increases the rate of water generation to a peak but starts to decline after that, as discussed above. Thermal conductivity plays a vital role for extended surfaces as it can be seen in the plot that Copper fins dominated over the Aluminum fins at different air-flow velocities.

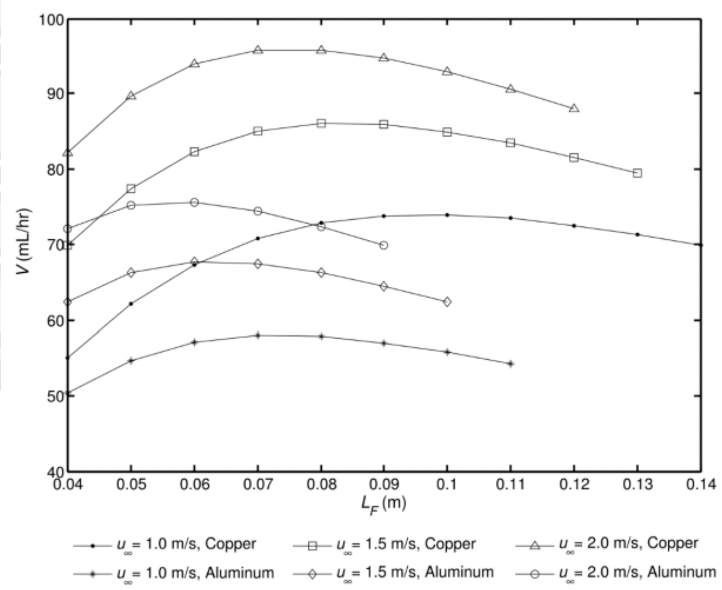

Figure 32 Representing volume of water generated with respect to the length of fins

Atmospheric water generator (AWG) tests were performed in a temperature and humidity-controlled room under different operating conditions. The three major factors for different tests/conditions were airflow velocities, surrounding air humidity, and TEC current. These factors were used for defining the water generation rate and specific energy consumption. Each experiment was performed twice, and the experiments were split into sets of different air-flow velocities, relative humidity levels, and TEC input power levels. There were 12 tests performed with different combinations of TEC connections and different operating conditions. The ambient temperature was measured for 2-hour at every 10 minutes and was then finally culminated. The variations in inlet conditions of fans negatively impacted the initial tests. However, later this variation was found to have a positive impact. However, to get an optimized value for the air-flow velocities, more test conditions were required. In all the airflow velocities and TEC connections, it was found that increased humidity improved the rate of water generation and specific energy consumption. Further, type B required more power input as compared to type A. Moreover, it had lower COP and more specific energy consumption than type A.

The author compared the AWG prototype with others while taking specific energy consumption as the most important criterion for evaluating efficiency. The presented prototype outstands with others as it gives major importance to extended surfaces on the cold side and current. It has a great influence on the efficiency of the system. Moreover, the specific energy consumption was lower than other prototypes for the same relative humidity. With the comparison, the importance of cold side fin design, TEC current level optimization, and changes in dimensions were justified for the prototype. Various ways can enhance the AWG; as mentioned by the author, some can optimize airflow velocities, basin design, and fin.

Moreover, a fin design could be developed for the wet fins to deal with the water vapor layers formed over them. Application of forced convection over fins and tilting fins could overcome the issue of wet fins to a certain degree, hence, integrating the effect of fins and cooling capacity from TECs. Finally, a change in basin design for the increment of water collection in the collector could be performed, as the basin was not slanted enough. This study emphasized the difference between with and without fin applications in the AWG and demonstrated the overall improvement for fin condition. One can infer the cost-effectiveness of the extended surface used.

CHAPTER III

METHODOLOGY

This study focuses on desiccant dehumidification (TED) to decrease the heat load on conventional vapor-compression refrigeration systems. The dehumidification system combines a composite desiccant, a heat sink, thermoelectric, and a ventilation fan to create a dehumidification system combination that. The advantages of TED with a composite desiccant-coated heat sink include the ability to exchange both sensible heat (fin heat sinks) and latent heat (desiccant material). Furthermore, the TED can regenerate the desiccant using the TEMs (hot-side) and reduce the air temperature before entering the room using the TEMs (cold-side).

This chapter explained the experimental design and production that were prepared for this work. Three major experimentation topics were under taken, firstly regarding the silica preparation cost using bagasse ash as the silica source. In this study, the mesoporous silica was prepared using sodium silicate by the alkali extraction method (topic 1). The effect of sodium hydroxide (NaOH) concentration on the physical properties and chemical phenomena of mesoporous silica was investigated. Secondly, improved composite DCAS with different mass concentrations of LiCl were fabricated and analyzed (topic 2). Thirdly, Thermoelectric dehumidifier (TED) with and without composite desiccant coated heat sink (topic 3).

A recyclable method for production of mesoporous silica nanostructure from bagasse ash of sugar cane industry

1. Materials and methods

1.1 Materials

The bagasse ash was obtained from the Thai Identity Sugar factory, Uttaradit, Thailand as shown in **Figure 33**. All of the chemicals used for producing mesoporous silica from bagasse ash were of the reagent grade. The sodium hydroxide (NaOH), sulfuric acid (H_2SO_4), and hydrochloric acid (HCl) were supplied by Merck. The initial silica content of the bagasse ash by X-ray Fluorescence analysis was 63.12 wt.%, and the main impurities were CaO (8.82 wt.%), K_2O (7.99 wt.%), and Fe_2O_3 (7.25 wt.%). Synthesis and treatment processes were performed using demineralized water.

1.2 Acid washing

Before synthesizing mesoporous silica, the sugar factory's bagasse ash was heat-treated to form a powder according to the method provided in the previous study of Chanchira et al. (136). According to the XRF analysis, the bagasse ash composition was mainly comprised of SiO_2 and oxides. In addition, XRF was conducted to determine suitable calcination times. The ash had the highest silica content of 80.81 wt.% after being calcined at 600 °C for 6 h.

According to previous research from Ribeiro and Morelli, which studied the effect of the calcination temperature on the pozzolanic activity of Brazilian sugar cane bagasse ash (SCBA), it was found that SCBA can be obtained under controlled calcination (500, 600, and 700 °C). From the XRD results, the SCBA calcined at 600 °C shows a higher amorphous characteristic (137). After calcining at 600 °C for 6 h, bagasse ash was washed with acid to remove all re-dissolved minerals. Then 10 g of bagasse ash was dispersed in 100 ml of distilled water with 1 N HCl. The dispersion was boiled with stirring for 2 h and filtered through Whatman No. 41 ashless filter paper. After that, the bagasse ash residues were washed with deionized water to a pH of 7.0 and dried for 15 h at 120 °C. The residues were utilized to extract silica.

Figure 33 Sugar cane bagasse (a) and sugar cane bagasse ash (b)

1.3 Silica extraction

The silica extraction was adopted from an alkali extraction method. The amount of 50 ml of NaOH solution containing different mass concentrations (1.0, 1.5, 2.0, and 2.5 N) was added to acid-washed bagasse ash and boiled for 3 hours at 100 °C with a constant stirring rate to dissolve the silica and produce a sodium silicate solution (**Figure 34**). The solution was filtered using Whatman No. 41 filter paper, and the carbon residues were washed with 20 ml boiling water. After allowing the filtrates and washings to cool to room temperature, mesoporous silica was prepared.

Figure 34 Sodium silicate from bagasse ash

1.4 Synthesis of mesoporous silica

The titrated sodium silicate solution prepared above to pH 7 with 2 N H_2SO_4 to obtain a gel. The gel was aged for 18 h. After aging, the gel was gently disintegrated by adding 100 ml of deionized water to make a slurry, then filtered and washed three times with deionized water and dried at 80 °C for 24 h in the furnace as show in **Figure 35**. The first step of the extraction of silica from ash as sodium silicate using NaOH.

$$SiO_2 + 2NaOH \rightarrow Na_2SiO_3 + H_2O \qquad (33)$$

The second step is precipitated silica from sodium silicate using H_2SO_4

$$Na_2SiO_3 + H_2SO_4 \rightarrow SiO_2 + Na_2SO_4 + H_2O \qquad (34)$$

The yield of silica is calculated as the following Equation (138)

$$\text{Yield of silica } (wt\%) = \frac{\text{Weight of silica obtained}}{\text{Weight of silica in bagasse ash}} \times 100\% \qquad (35)$$

Figure 35 Mesoporous silica from bagasse ash

2. Characterization

X-ray diffraction (XRD) analysis was used to investigate the mesoporous silica's crystallographic structure. The infrared spectra were recorded using a Fourier transform infrared (FT-IR) spectrophotometer. Scanning Electron Microscopy (SEM) was used to determine the morphology of mesoporous silica. The surface area, pore volume, and pore size were measured and analyzed using a surface area and porosity analyzer (Micromeritics-TriStar II 3020). The system utilizes the static volumetric technique to obtain nitrogen adsorption/desorption isotherms at -196 °C.

Development and characterization of composite desiccant-coated aluminum sheets (DCAS)

1. Preparation of composite desiccant-coated aluminum sheets (DCAS)

Table 8 presents the specifications of the materials that were utilized in this study. It was based on the coating technique developed by Zheng et al. (139). The commercial silica gel was dried at 100 °C for 4 h prior to preparing the composite DCAS. An aluminum sheet was weighed and brushed with liquid glue, followed by the scattering of silica gels onto the glue-adhered sheet. After dipping the aluminum sheet in silica sol for approximately 30 min to thoroughly combine the silica gel, it was dried at 100 °C for 4 h. The aluminum sheets were dipped in silica sol and dried 5 more times. The aluminum sheets were then immersed in an aqueous lithium chloride (LiCl) solution containing various mass concentrations (30, 35, 40, and 45 wt.%) for 12 h before being dried in an oven at 100 °C for at least 6 h until the weight remained constant. The salt content of the composite DCAS was measured by weighing the aluminum sheets before and after salt impregnation, as shown in **Figure 36**.

Table 8 Material specifications for preparing the DCAS

Name	Description	Manufacturer
Aluminum sheet	60 mm × 40 mm × 1 mm $k = 230\ Wm^{-1}\ K^{-1}$	AIC Aluminum Profile Service Center
Silica gel	Mesoporous, the grain size of 70 to 230 mesh $S_{BET} = 500\ m^2\ g^{-1}$; $V_t = 0.75\ cm^3\ g^{-1}$; $d_{av} = 6$ nm $k = 0.1\ Wm^{-1}\ K^{-1}$	Merck KGaA
Silica sol	30 wt.% suspension in H_2O, pH = 9.1 $S_{BET} = 230\ m^2g^{-1}$; $V_t = 0.21\ cm^3g^{-1}$; $d_{av} = 4.3$ nm	Merck KGaA
Liquid glue	Polyurethane base (BT550) $k = 0.26\ Wm^{-1}\ K^{-1}$	Adhesive Manufactures Bond Chemicals Co.,Ltd
Anhydrous LiCl	ACS reagent, assay ≥99%	Merck KGaA

Table 9 shows the results of this research, which included the fabrication of four composite DCAS. The composite DCAS were labeled SG-L30, SG-L35, SG-40, and SG-L45, where the digital numbers represent the mass concentrations of the impregnating LiCl in the composite DCAS, respectively. The salt content of composite DCAS increased as the impregnating concentration of LiCl solution increased. SGCAS (SG-L0) was also produced as a contrast sample.

Table 9 Experimental parameters of the DCAS

Composition	Impregnating Concentration of LiCl (wt.%)	Mass of Desiccants (g)	Total Mass (g)	Salt Content (wt.%)	Coating Amount (kg m^{-2})
SG-L0	0	1.05	7.45	0.0	0.44
SG-L30	30	1.18	7.58	12.38	0.49
SG-L35	35	1.20	7.60	14.29	0.50
SG-L40	40	1.23	7.63	17.14	0.51
SG-L45	45	1.27	7.67	20.95	0.53

2. Characterization

2.1 Thermal Conductivity

The hot disk thermal constant analyzer (TCA), Hot Disk AB: TPS2500S, was used to measure the thermal conductivity of the DCAS. Thermal conductivity was measured using the standardized transient plane source (TPS) technique, which has an accuracy greater than 5%. The samples were 50 mm × 50 mm × 10 mm in size. Before the test, all of the DCAS samples were oven-dried for 4 h at 100 °C.

2.2 Textural and morphological characterization

The BET surface area, pore volume, and pore size were measured and analyzed using a surface area and porosity analyzer (Micromeritics-TriStar II 3020, Micromeritics instrument corporation, Norcross, United States). To obtain nitrogen sorption isotherms at 77 K, the system employed the physical adsorption and capillary condensation principles. Temperature and pressure were the main causes of experimental errors. The temperature accuracy of the manifold was ±0.25 °C, and the pressured ones had a testing error of around 0.5%. To determine the morphology of DCAS, scanning electron microscopy (SEM) analysis was performed using a LEO1455VP scanning electron microscope. X-ray diffraction (XRD) analysis is used to investigate the desiccant coated aluminum sheets’ crystallographic structure.

Additionally, scanning electron microscopy (SEM) analysis was carried out, employing a LEO1455VP scanning electron microscope, to determine the morphology of DCAS.

2.3 Sorption kinetics

The kinetics of the DCAS sorption were studied in a constant temperature and humidity chamber. The humidity control range was 10 to 98%, while the temperature range was -70 to 180 °C. The defined working conditions were set at 20 °C and 70% RH. During the test, the temperature fluctuated in the chamber by 0.1 to 0.2 °C while the relative humidity fluctuated by ±2.5%. Before the test, the DCAS samples were dried at 100 °C for 4 h in an oven and weighed. The DCAS were then placed in a chamber with pre-set conditions. The weights of the DCAS were recorded at prescribed times on an electronic scale with an accuracy of 0.001 g, which was used in this study.

The LDF model may be used to determine the adsorption rate (140). The sorption rate can therefore be represented by,

$$\frac{dx}{dt} = k(x - x_t) \tag{36}$$

Where dx/dt is the sorption rate, k is the sorption rate coefficient (s^{-1}), x is the equilibrium water sorption quantity ($g\ g^{-1}$), and x_t is the dynamic water sorption quantity ($g\ g^{-1}$).

After integration of Equation (36), the dynamic water sorption quantity of a DCAS can be calculated.

$$x_t = x(1 - \exp(-kt) \tag{37}$$

Rearranging Equation (37) and using the Napierian logarithm, results in the following

$$-\ln(1-\frac{x_t}{x})=kt \tag{38}$$

2.4 Moisture sorption isotherms

The DCAS moisture sorption isotherms were generated using a vapor sorption analyzer (VSA) at 25 °C. The VSA generated dynamic isotherms by employing the dynamic dew point isotherm (DDI) method, water activity, and a gravimetric analysis method that does not control water content or activity but dries or wets the sample to measure water activity and water content during the wetting or drying process. A high-precision magnetic force balance was used to weigh the samples to determine water content. **Table 10** shows the specifications of the VSA.

Table 10 Vapor sorption analyzer (VSA) specifications

Physical Parameter	Range or Deviation
Water activity, A_w	0.03-0.95 A_w
Water activity, A_w accuracy	±0.005 A_w (for volatiles setting ± 0.02 A_w)
Sample temperature control range (°C)	15-60 at STP
Operating environment (°C)	4-50
Sample weight (mg)	500-5,000
Mass resolution (mg)	±0.5

“Source” Vapor Sorption Analyzer (operator ’s manual)

2.5 Moisture sorption isotherms models

Moisture sorption isotherms depict the relationship between water activity and moisture content at a constant temperature. It depends on the chemical composition, physical structure, and physical-chemical condition of the material. Due to variations in capillary, surface, and colligative processes, the isotherm shape is unique to each material type. Over the decades, several renowned adsorption models were developed based on monolayer and multilayer adsorption theories, with the BET (141) and GAB (142) being the most widely used. The BET model is often used to estimate moisture sorption data ranging from 0 to 0.5 A_w (143).

In comparison, the GAB model enhances the BET model’s applicability over a broader range (0.05 to 0.95 A_w) (142). The DLP model (144) is a new empirical model that is even more effective than the GAB model in characterizing complicated isotherms. The ability of the three moisture sorption isotherm models to fit the experimental data for the DCAS was evaluated in this study (BET, GAB, and DLP). The following are the equations for the models:

BET

$$m = \frac{cm_0 A_W}{(1-A_W)(1+(c-1)A_W)} \tag{39}$$

GAB

$$m = \frac{c_1 K m_0 A_W}{(1-KA_W)(1-KA_W+c_1 KA_W)} \tag{40}$$

DLP

$$m = b_3 x^3 + b_2 x^2 + b_1 x + b_0 \tag{41}$$

Where m is moisture content (%) and, for Equations (39) and (40), *c* is a constant related to water binding energy to the primary binding sites, m_0 is the monolayer moisture content (%), A_w is the water activity, c_1 is a dimensionless measure of the strength of water binding to the primary binding sites, and *K* is a constant related to the adsorption energies of multilayer adsorption sites. In the GAB model, which differs from the BET theory, the difference in adsorption energies between monolayer and multilayer adsorption sites is represented by an additional adsorption parameter (*K*). The GAB model may be reduced to the BET equation when parameter $K = 1$. Moreover, in Equation (41), $x = \ln(-\ln(\mathrm{A}_w))$;b_0, b_1, b_2, and b_3 are empirical constants. The BET, GAB, and DLP models were fitted using non-linear regression. The Origin 9.0 software was used to perform regression calculations. In addition to the coefficient of determination (R^2) of the non-linear regression, the goodness of the model fit was tested using the root mean square error (RMSE). **Figure 37** show characterization of composite desiccant-coated aluminum sheets (DCAS).

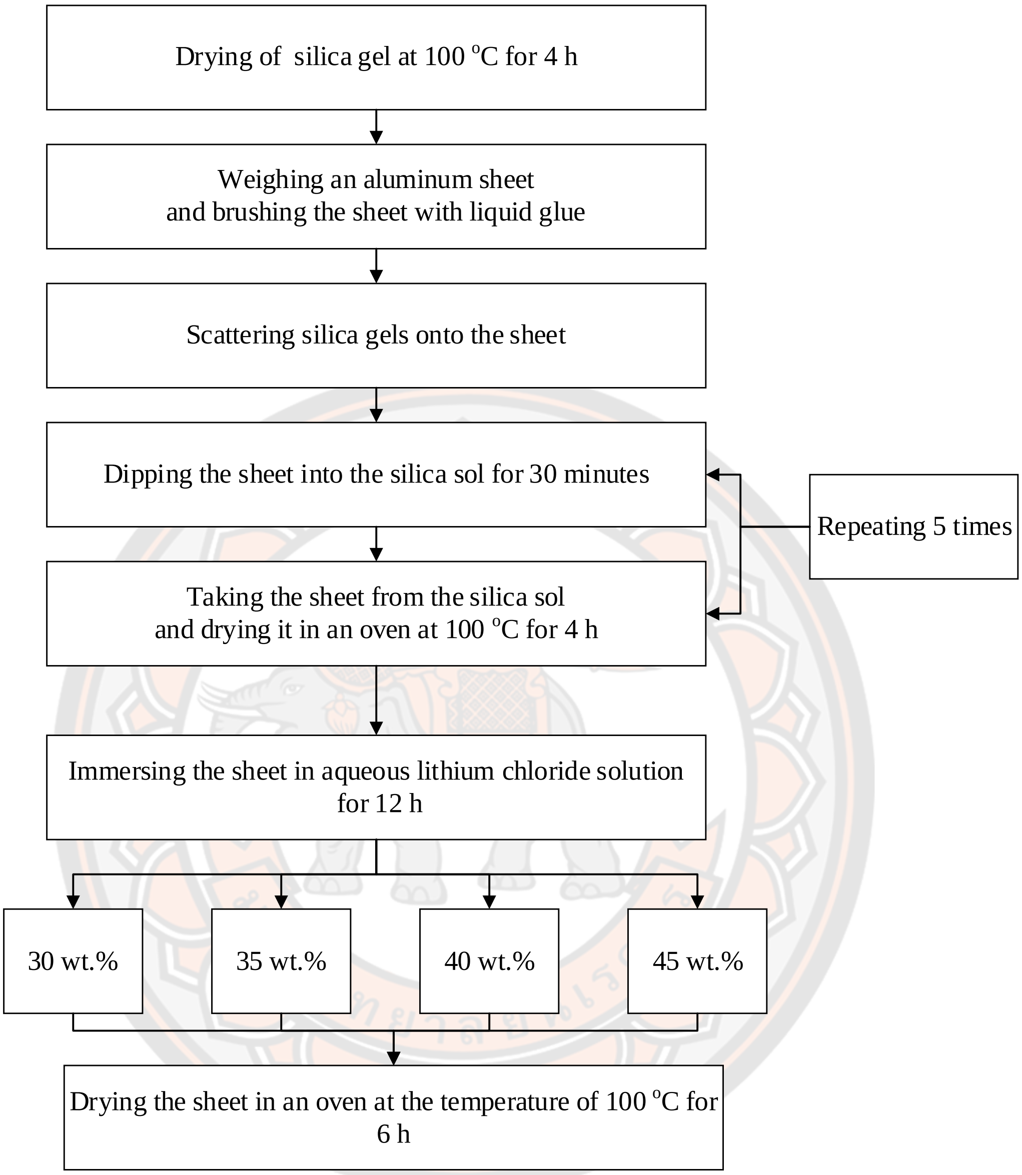

Figure 36 Preparation of composite desiccant-coated aluminum sheets (DCAS)

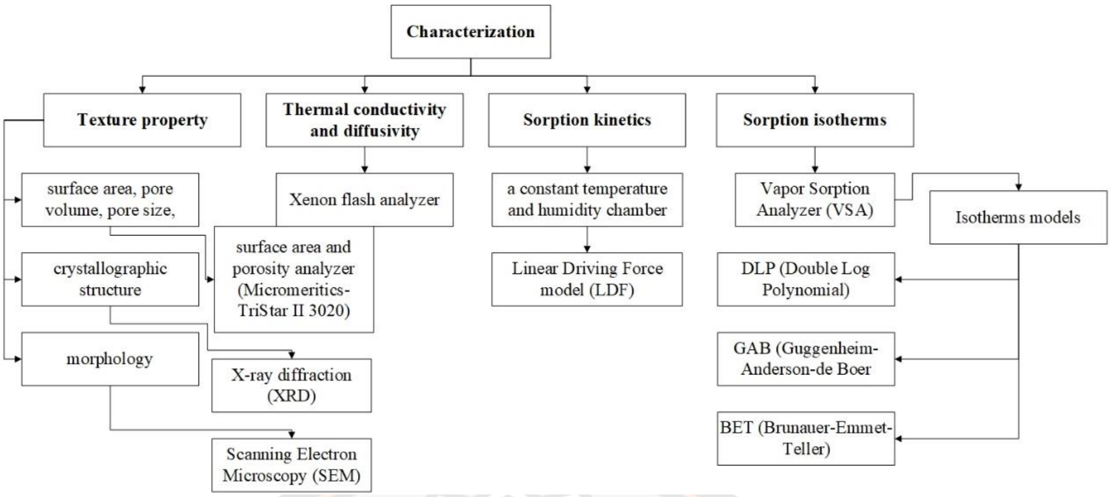

Figure 37 Characterization of composite desiccant-coated aluminum sheets (DCAS)

Thermoelectric dehumidifier (TED) without and with composite desiccant coated heat sink

1. System description

Thermoelectric coolers (TEC) are ideal devices to cool electronic components or small electronic enclosures. However, practical limitations can restrict the range of useful applications. One serious limitation is the performance of conventional heat exchangers. The TEC consists of P and N-type dissimilar conductors (e.g., bismuth-telluride-selenide) through which an electric current flow. The TEC utilizes the Peltier effect, whereby an electric current pumps heat and produces a temperature differential between the junctions of the P and N-type materials. It is the inverse of the thermocouple operating principle, in which a temperature differential across the junctions of dissimilar materials produces an electric current. The P and N-type elements are sandwiched between two ceramic plates. One ceramic plate is cooled to a cold temperature (T_c) by the Peltier heat pumping. Heat must be rejected from the other plate at a hot temperature (T_h). In addition to the heat pumped into the cold ceramic, heat is pumped within the TEC from two other sources. These are the internal resistive, or Joule heat, and the heat conducted through the thermoelectric elements. At moderate to high temperature differences across the TEC, the conducted heat can become the greatest source of heat and can severely limit the performance of the device. A "heat sink" heat exchanger must be attached to the TEC hot side to reject heat to ambient. Typically, air-cooled heat exchangers are used. A low performance heat exchanger can result in high values for the hot-side temperature. Such high temperatures increase the conduction heat source and severely limit the COP of the TEC (145).

A relationship is developed to define the required thermal resistance of the heat sink heat exchanger as a function of the properties of the thermoelectric material, the cold side heat input and temperature, and the entering coolant temperature. A novel, air-cooled thermosyphon reboiler-condenser system is described that promises significantly higher COP for a TEC than is possible with current heat exchange technology. This heat exchanger design concept is described, and preliminary test results are presented. The performance of the new heat exchange device is compared to that of conventional heat exchange devices.

2. TED system modelling

The derivation of governing equations will be done for an arbitrary module of TE elements. The lists of assumptions made in deriving the governing equations are as follows:

2.1 Assumptions

2.1.1 One-dimensional heat transfer under steady-state conditions.

2.1.2 The material properties are known and constant for small temperature differences.

2.1.3 No heat is lost or gained through the sides of the elements.

2.1.4 Thermal properties of materials are independent on the temperature.

2.1.5 Inlet air temperature is considered equal to ambient temperature.

2.2 Thermoelectric consideration

A typical multicouple thermoelectric module is show schematically in **Figure 38**, n and p type semiconductor thermoelement are connected is series by highly conducting metal strips to form a thermocouple. The output voltage V_0 and output current I_0, arc given by (146):

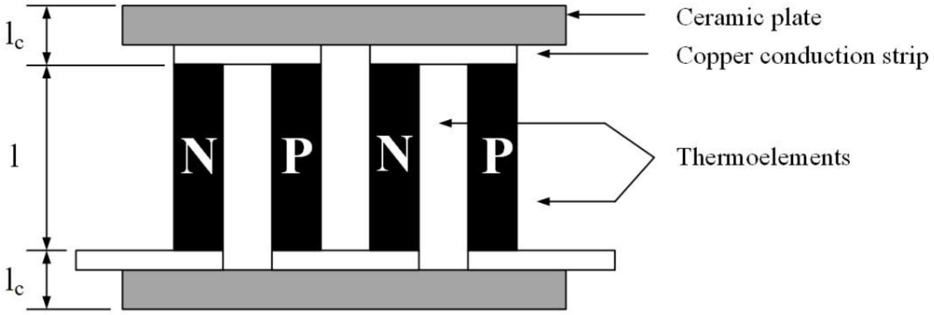

Figure 38 Schematic diagrams of multicouple thermoelectric modules

$$V_0 = \frac{\alpha N\left(T_h - T_c\right)}{1 + 2rI_c / l} \tag{42}$$

$$I_0 = \frac{\alpha A_c\left(T_h - T_c\right)}{2\rho\left(\psi + 1\right)\left(1 + 2rl_c / l\right)} \tag{43}$$

Where

N is number of thermoelement in the module

α is Seebeck coefficient, V K^{-1}

T_h is Temperature at the hot side, K

T_c is Temperature at the cold side, K

A_c is cross-section area of each P-N thermoelectric element, m^2

l is Length of the thermoelement, m

l_c is Thickness of the contact layer, m

ρ is Electrical resistivity of the thermoelement, Ω m

ρ_c is Electrical resistivity of contact

k is Thermal conductivity of the thermoelement, W m^{-1} K^{-1}

k_c is Thermal conductivity of the contact, W m^{-1} K^{-1}

$$r = \frac{k}{k_c}$$

$$\psi = \frac{2\rho_c}{\rho}$$

The power output can be written as

$$P_0 = \frac{\alpha^2}{2\rho}\frac{A_c N}{(\psi+1)(1+2rl_c/l)^2} \tag{44}$$

2.2.1 Thermoelectric Cooler Performance (145)

A schematic diagram of a thermoelectric couple used in a TEC is shown in **Figure 39**. In this Figure, Q_c is the heat removed from a device being cooled. This includes the active heat generated by the device and any passive loads from the surroundings. Q_h is the heat that must be rejected from the TEC's hot side. It includes the cold side heat load, Q_c, and the electric power input to the TEC, P_e, Q_{hs} is the heat sink thermal resistance for constant heat sink temperature. For a given TEC size, this is expressed in units of K W^{-1}.

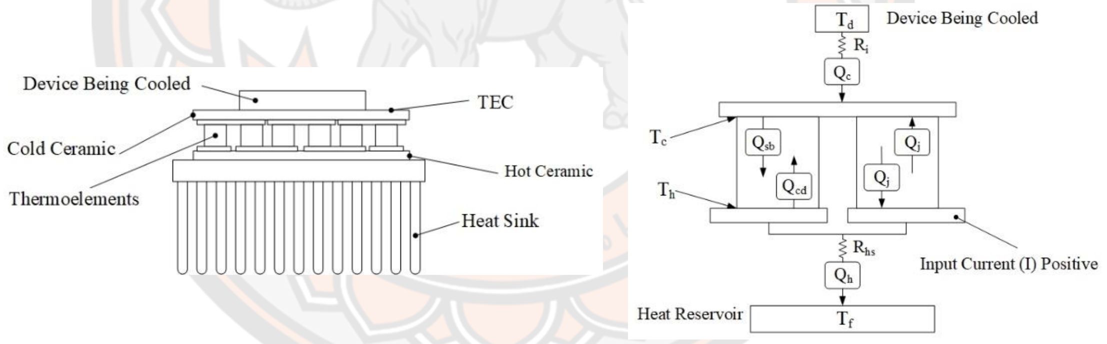

(a) **(b)**

Figure 39 Typical TEC cooling application (a) and schematic diagram of a thermoelectric couple (b)

Cold-Side Heat Transfer.

Peltier Heat Pumping. The actual thermoelectric heat pumping (Peltier effect) at the cold side of the TEC is defined by Ioffe (147) as Seebeck/Peltier heat pumping rate, Q_{sb} (W) and is given by

$$Q_{sb} = 2N\alpha IT_c \tag{45}$$

We see from this relation that heat is pumped when current flows through a TEC. However, the heat pumped may include other unwanted heat sources.

Joule Heat. Current flow generates resistive or Joule heating (Q_J) in the thermoelectric material. It can be shown that 50 percent of the Joule heat goes to the cold side and 50 percent goes to the hot side. Details of this analysis are presented by Goldsmid (148). The Joule heat generation rate, Q_J (W) is given by

$$Q_J = 0.5I^2\left(2N\lambda\rho\right) \tag{46}$$

Conducted Heat. During operation, heat is conducted from the hot side to the cold side of the TEC through the thermoelectric material. The rate of heat conduction within all thermoelectric elements, Q_{cd} (W) is given by

$$Q_{cd} = k\left(2NA_c\right)\frac{\left(T_h - T_c\right)}{H} = k\frac{2N}{\lambda}\left(T_h - T_c\right) \tag{47}$$

Equation (47) shows that Q_{cd} increases with the temperature difference across the TEC. Combining Equation (45), (46), and (47) into an energy balance at the cold side of the thermoelectric elements gives the following:

The heat transfer rate to cold-side ceramic, Q_c (W)

$$Q_c = Q_{sb} - \left(Q_J / 2\right) - Q_{cd} = 2N\alpha I T_c - 0.5 I^2 N \lambda \rho - \left(2N / \lambda\right) k \left(T_h - T_c\right) \tag{48}$$

Where

α is Seebeck coefficient of thermoelectric material, W A^{-1} K^{-1}
N is total number of P and N couples in thermoelectric device
I is current flow, A
ρ is electric resistivity of the thermoelectric material Ω m
λ is thermoelectric element aspect ratio ($\frac{H}{A_c}$), m^{-1}
k is thermal conductivity of thermoelectric material, W m^{-1} K^{-1}
T_h is hot-side surface temperature of the TEC, °C
T_c is cold-side surface temperature of the TEC, °C

Equation (48) is the standard TEC performance equation. From this equation, we can conclude that a thermoelectric module is not functional ($Q_c = 0$) when the total of half the Joule heat and the conducted heat equals the Peltier heat. Q_c is zero when $0.5Q_J + Q_{cd} = Q_{sb}$.

The module's power consumption (electrical energy) Q_E (W) is:

$$Q_E = IV = 2N\left(I^2 \rho \lambda + \alpha I \left(T_h - T_c\right)\right) \tag{49}$$

Thermoelectric module cooling COP:

$$\varepsilon = \frac{Q_c}{Q_E} = \left[\left[aIT_c - \frac{k}{\lambda}\left(T_h - T_c\right) - 0.5 I^2 \rho \lambda\right] / \left[I^2 \rho \lambda + \alpha I \left(T_h - T_c\right)\right]\right] \tag{50}$$

There is an optimum current for maximum COP for specific modules and working temperatures. The equation by $\delta\varepsilon / \delta I = 0$

$$I_{opt} = \left[\frac{k}{\lambda} (T_h - T_c) \left(1 + (1 + ZT_m)^{1/2} \right) \right] / (\alpha T_m) \tag{51}$$

Replacing I in Equation (50) by I_{opt}:

$$\varepsilon_{opt} = \left[T_m / (T_h - T_c) \left(\left((1 + ZT_m)^{1/2} - 1 \right) / \left((1 + ZT_m)^{1/2} + 1 \right) \right) \right] - \frac{1}{2} \tag{52}$$

$$T_m = \frac{1}{2}(T_h + T_c) \tag{53}$$

The dimensionless Figure of merit, ZT. The value of Z is given by

$$Z = \alpha^2 / (\rho k) \tag{54}$$

Where α, ρ and k represent the Seebeck coefficient (V K^{-1}), electrical resistivity (Ω-cm) and thermal conductivity (W cm^{-1} K^{-1}) respectively.

The material property coefficient of thermoelectric are from Electronics cooling December 2014 electronics-cooling.com and Laird Smart Technology Delivery company. Material Property Coefficients

$$\alpha = \left(\alpha_0 + \alpha_1 T_m + \alpha_2 T_m{}^2 \right) \times 10^{-9} \text{ (V K}^{-1}\text{)} \tag{55}$$

$$\alpha_0 = 22224.0$$

$$\alpha_1 = 930.6$$

$$\alpha_3 = -0.9905$$

$$\rho = \left(\rho_0 + \rho_1 T_m + \rho_2 {T_m}^2\right) \times 10^{-8}\,(\Omega\ \text{cm}) \tag{56}$$

$$\rho_0 = 5112.0$$

$$\rho_1 = 163.4$$

$$\rho_3 = -0.6279$$

$$k = \left(k_0 + k_1 T_m + k_2 {T_m}^2\right) \times 10^{-6} \tag{57}$$

$$k_0 = 62605.0$$

$$k_1 = 277.7$$

$$k_3 = 0.4131$$

Hot Side Heat Transfer. An energy balance on the hot side of the thermoelectric elements gives

Heat transfer rate to hot-side ceramic, Q_h (W)

$$Q_h = 2N\alpha I T_h - 0.5 I^2 N \lambda \rho - \left(2N/\lambda\right) k \left(T_h - T_c\right) \tag{58}$$

Thermoelectric module for heating COP

$$\eta = \frac{Q_h}{Q_E} = \left(Q_c + Q_E\right)/Q_E = 1 + Q_c/Q_E \tag{59a}$$

$$\eta = 1 + \left(\alpha I T_c - \frac{k}{\lambda}\left(T_h - T_c\right) - 0.5 I^2 \rho \lambda\right) / \left[I^2 \rho \lambda - \alpha I \left(T_h - T_c\right)\right] \tag{59b}$$

Given $\delta\eta/\delta I = 0$, the optimum current for the maximum COP for heating equals that for cooling (see Equation (51)). Put I in Equation (59b) by I_{opt}, to get maximum COP:

$$\eta_{\max} = 1 + \left[T_m/\left(T_h - T_c\right)\left(\left(\left(1 + ZT_m\right)^{1/2} - 1\right)/\left(\left(1 + ZT_m\right)^{1/2} + 1\right)\right)\right] - 1/2 \tag{60}$$

2.4 Heat sink

The cold and hot sink shown in **Figure 40**. The geometric parameters of this model are n channels and n-1 fin. The two effects resulting from the use of finitely thick fin are a reduction of cross-sectional flow (L_f and W) and the induction of influential fin efficiency. The same assumptions are made regarding properties, steady state, entrance effect, etc.

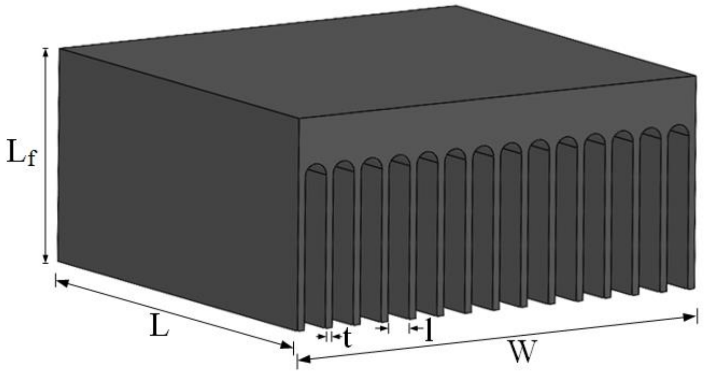

Figure 40 Schematic of cold and hot sink

Figure 40 shows the geometry of the heat spreader being analyzed is ratio of tin thickness to fin space. The following four equations 61 to 64 are strictly geometric. They describe respectively the hydraulic diameter of one channel (D_h), the cross section available for flow in the system, the aspect ratio for one channel (A_s), and the surface area available for heat transfer (A_f) (149).

$$D_h = \frac{2W}{n_f + \Gamma\left(n_f - 1\right) + W / L_f} \tag{61}$$

$$A_f = \frac{n_f W L_f}{n_f + \Gamma\left(n_f - 1\right)} \tag{62}$$

$$l / L_f = \frac{W / L_f}{n_f + \Gamma\left(n_f - 1\right)} \tag{63}$$

$$A_s = \frac{n_f W L_f}{n_f + \Gamma\left(n_f - 1\right)} + 2\eta_f L_f L(n_f - 1) \tag{64}$$

The Nusselt number developed in a rectangular channel is also the function only aspect ratio of the channel. The Nusselt number (Nu) equation is as follows:

$$Nu = -1.047 + 9.326G \tag{65}$$

In this case, the Nusselt number results from a boundary condition of constant heat flux. A parameter G is defined as suggested by Bejan; by:

$$G = \frac{\left(l / L_f\right)^2 + 1}{\left(\left(l / L_f\right) + 1\right)^2} \tag{66}$$

For an approximation, it has been assumed the length of the fin is much more than its thickness, L , Γl . From the definition of Nusselt number

$$h = \frac{Nu k_a}{D_h} \tag{67}$$

k_a =0.0029+7.76x10^{-5}T$_a$

k_a is Thermal conductivity of air

Heat sink resistance (HSR) characterizes the overall performance of heat sink

$$HSR = \frac{l}{h} + \frac{L_b}{k_f} \tag{68}$$

Where

h is convection heat transfer coefficient of fluid, W m^{-2} K^{-1}

k_f is Thermal conductivity of fin material (204 W m^{-1} K^{-1}) (149)

l is gap thickness

L_b is base fin thickness (0.007 m)

The cold side temperature of the module is given in the equation below (150)

$$T_c = HSR\left(Q_h - P_o\right) + T_a \tag{69}$$

The rectangular fin is used to enhance beat transfer in the present study at the cold side. The fin efficiency of the rectangular fin (n_f) can be expressed as:(151)

$$n_f = \frac{\tanh mL_c}{mL_c} \tag{70}$$

$$mL_c = \left[\frac{2h}{k_f A_P}\right]^{0.5} L_c^{1.5} \tag{71}$$

Where

A_P is corrected fin profile area (m^2) $= L_c \cdot t$

L_c is corrected fin length (m)= $L_f + 0.5t$

L_f is fin length (0.04 m)

t is fin thickness (0.003 m)

2.4.1 Heat sink coated with composite desiccant

Before preparing the composite desiccant, the commercial silica gel was dried at 100 °C for 4 h. The Heat sink was weighed and brushed with liquid glue, followed by the scattering of silica gels onto the glue-adhered sheet. The Heat sink was then dipped in silica sol to thoroughly combine the silica gel for around 30 min, and dried at 100 ^{o}C for 4 h. The Heat sink were dipped in silica sol and dried 5 more times. After that, the Heat sink were immersed in an aqueous lithium chloride (LiCl) solution containing different mass concentrations (40 wt.%) for 12 h, and dried in an oven at 100 ^{o}C for at least 6 h until the weight remained constant. Additionally, Silica gel coated heat sink (0 wt.% of LiCl) was produced as a contrast sample, as shown in **Figure 41**.

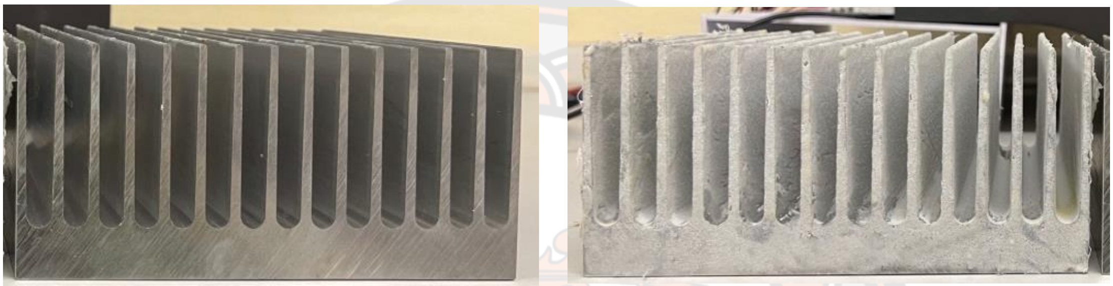

TED without composite desiccant **TED with composite desiccant**

Figure 41 A schematic view of the structure of TED

3. Experimental setup

A schematic of the structure of TED is illustrated in **Figure 42**. It consists of twenty-four TE module (TEMs) (model TEC1-12708, China) are made of bismuth telluride-based alloys were used. Each module had an area of 4×4 cm^2, as shown in **Figure 43**. The TEC1-12708 is a popular commercial TEM, which is used to build the dehumidification. Its parameters are listed in **Table 11** and **12.** The TE modules were connected in series and arranged in 2 rows with 6 TE modules in each row connected in parallel in each row (**Figure 44**). The rectangular fin heat sinks made of aluminum were attached to the hot side of TE modules in order to release heat more efficiently. The cold side of the TE modules was also attached to the rectangular fin heat sinks in order to cool the air. The fins were 3 mm thick; 145 mm long in the horizontal direction and have a height of 40 mm from the base. They are 10 mm spaced each other as shown in **Figure 45**. Four direct-current (DC) fans were used: two at the hot side mainly to help propel the extra heat out into the atmosphere, and the other at the cold side for enhancing convection of the air flowing through the fin heat sink at the cold side. The TEC-12708 and fans are electrically driven by the 12V DC power. A DC power supply with adjustable voltage is used to drive the fan. All the heat sinks are made of Al alloy and air ducts are consisted of acrylic plates. During the experiment, an electrical voltage was supplied to the TEMs at different voltages of 3, 6, 9, and 12 V, respectively. The cycle time was set at 60 min. In this study, the hot side air flow rate was fixed at 0.08 kg s^{-1}, the clod side air flow rate was 0.04, 0.06, and 0.08 kg s^{-1}. The humidity ratio and temperature are 13.19 g kg^{-1} and 28 ºC, respectively.

The dehumidification system comprises two dehumidifier units. One of the dehumidifier units works on the dehumidification process, so it was supplied with the cold side of TEMs to adsorb moisture in ambient air, whereas the other works on the regeneration process, so it was supplied with the hot side of TEMs to remove water from the saturated desiccant. Two of these dehumidifiers work simultaneously; while one dehumidifies the working air, the other gets regenerated. The two switch their operations periodically to achieve dehumidification of the work in process. The experiments were performed during December 2021 to January 2022. Experimentation started at 9 a.m. and ended at 5 p.m. A data-acquisition system was used to collect data at regular 5 min intervals. **Figure 46** shows a schematic diagram of experimental setup and data acquisition system.

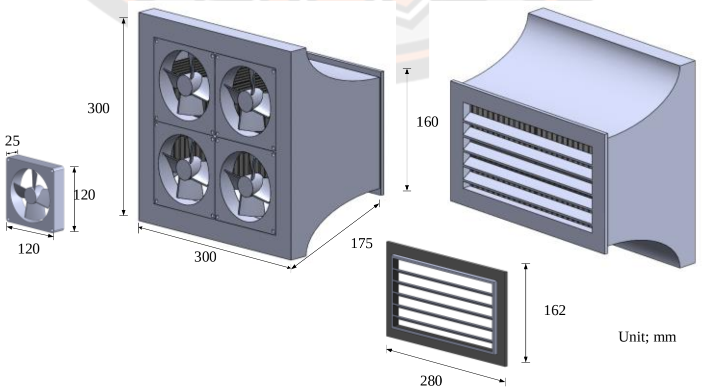

Figure 42 A schematic view of the structure of TED

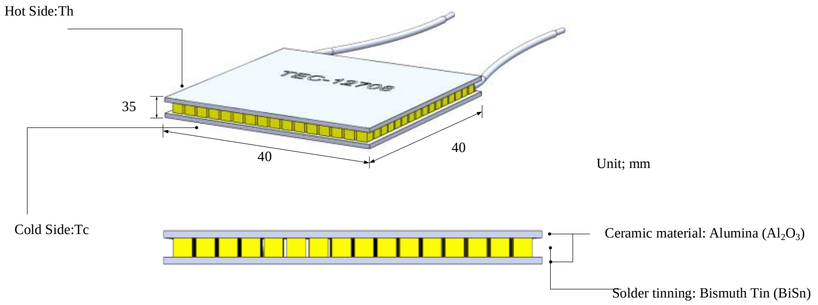

Figure 43 TE module (TEMs) (model TEC1-12708, China)

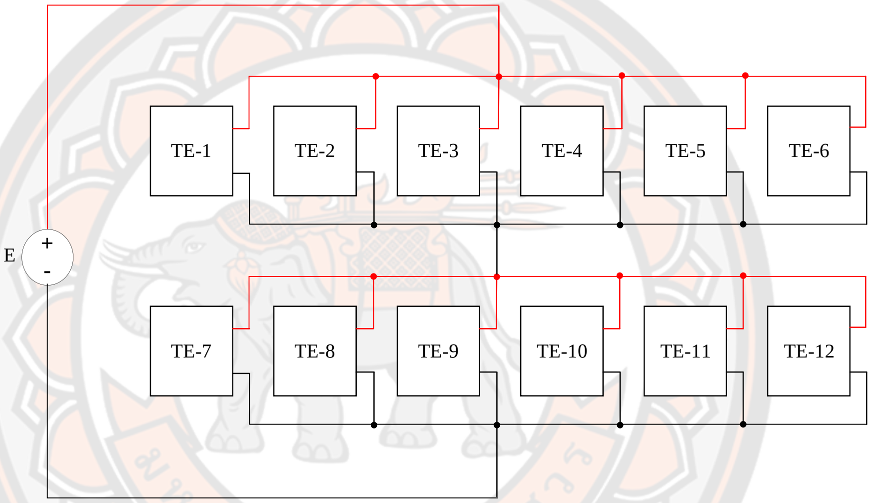

Figure 44 Parallel connection image of TEC1-12708 thermoelectric module same block and the serial connection image thermoelectric module the two blocks

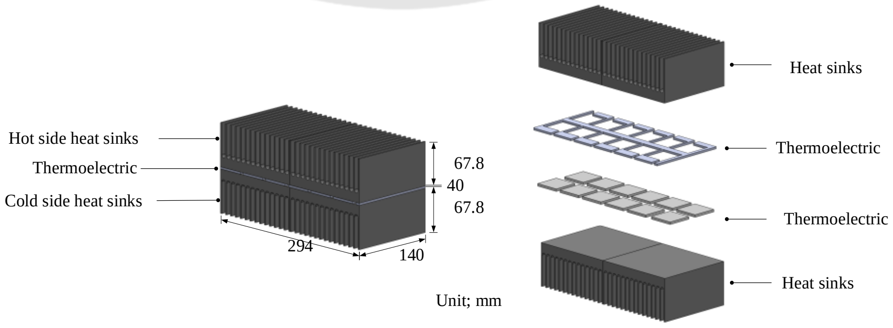

Figure 45 The specifications of cold-side and hot-side heat sinks

Table 11 Characteristics of thermoelectric TEC1-module 12708

Parameter	TEC1-12708
Leg length 9 width (mm)	14×14
Leg height (mm)	1.2
Area of the thermoelement (mm^2)	1.96
Contact height (mm)	1.0
Insulator plate thickness (mm)	0.63
Module height (mm)	3.46
Area-to-length ratio	1.63
Max. operating hot-side temp. (^oC)	160-170
Module cost (US$)	8

Table 12 Specification of thermoelectric TEC-Module 12708

Hot side Temperature	25 ^oC	50 ^oC
Q_{max} (W)	71	79
ΔT_{max} (^oC)	66	75
I_{max} (A)	8.5	8.4
V_{max} (V)	15.4	17.5
Module Resistance (Ω)	1.50	1.80

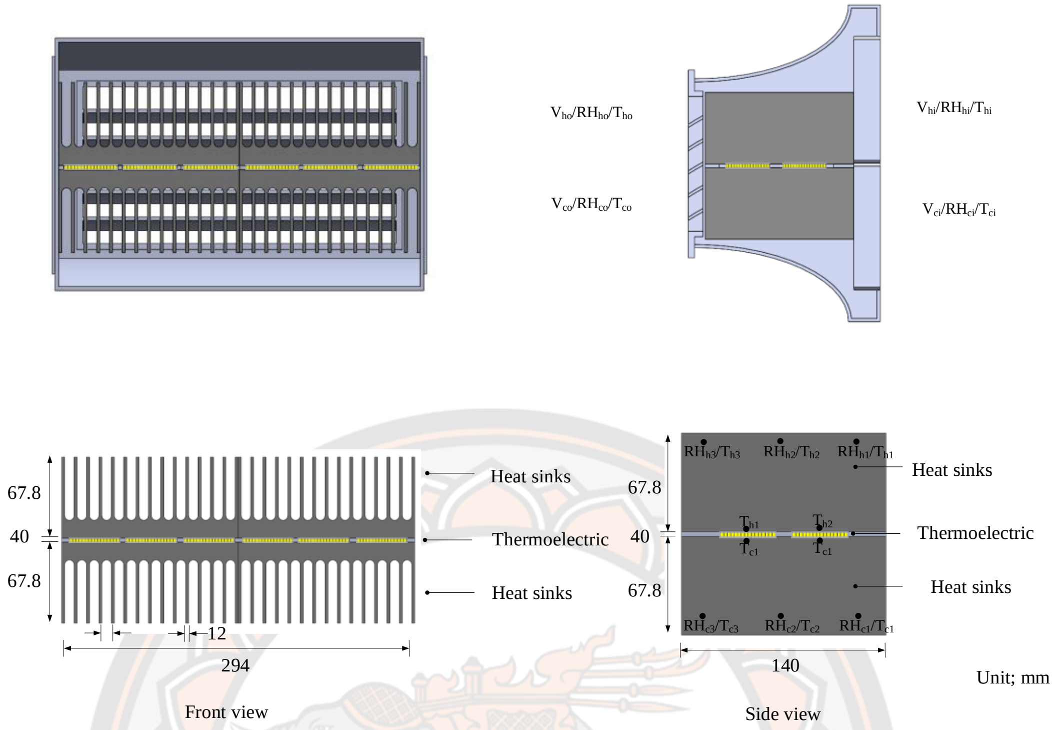

(a) A schematic diagram of experimental setup and data acquisition system

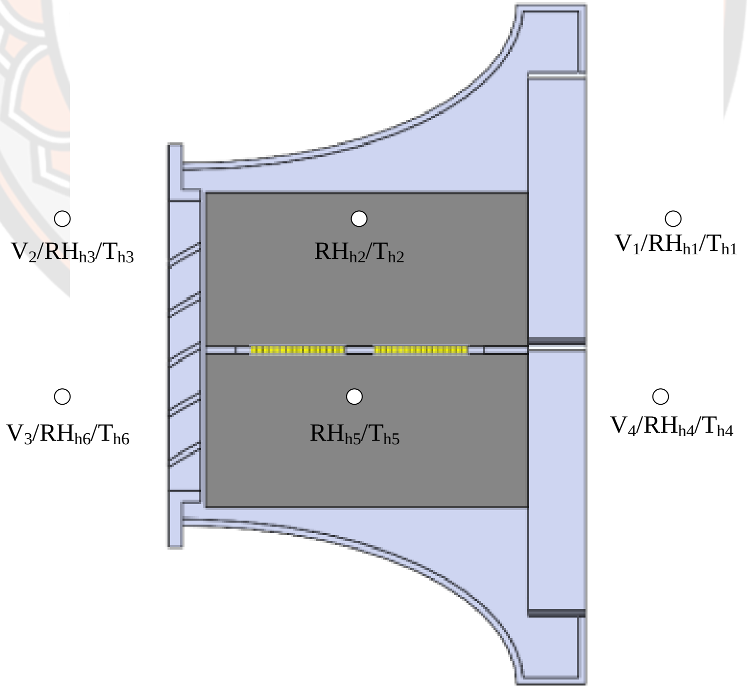

(b) The sensor DHT22 recorder was set to position in the hybrid air ventilation

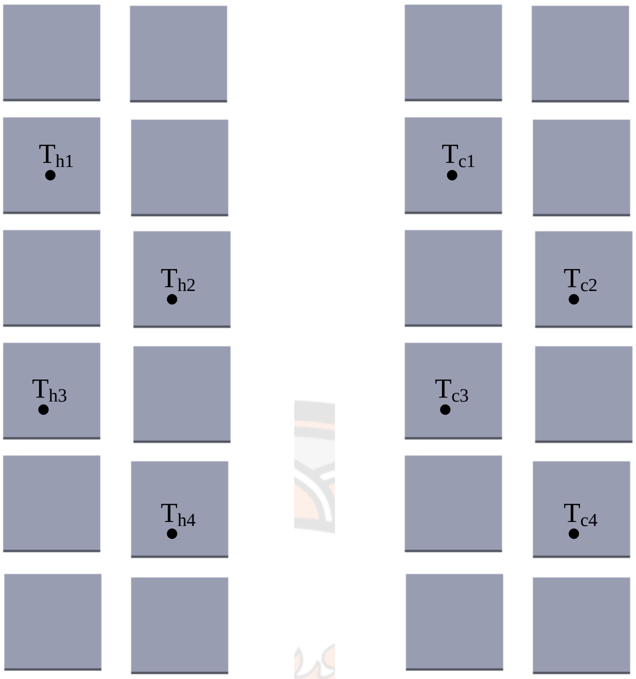

(c) Setting thermocouple to position measuring

Figure 46 Schematic diagram of experimental setup and data acquisition system

The relative humidity (RH) and temperature at the heat sink were computed by the measurement of the two (1 hot and 1 cold),as shown in **Figure 44(b)** and the mean temperature hot and cold sides (T_h and T_c) of TEMs were computed by averaging the measurement of the eight (4 hot and 4 cold) points embedded, as shown in **Figure 44(c)**.

$$T_h = \frac{T_{h1} + T_{h2} + T_{h3} + T_{h4}}{4} \tag{72}$$

$$T_c = \frac{T_{c1} + T_{c2} + T_{c3} + T_{c4}}{4} \tag{73}$$

4. Working principle

Two composite desiccant coating heat sinks (CCHSs) run in parallel with respect to two modes: dehumidification and regeneration process mode. Process air is divided into two parts for dehumidification and regeneration, respectively. In other words, during the first cycle as shown in **Figure 47**, cooling air is pumped into CCHS-C through cold fan (1,2). The process air can be dehumidified and cooled at the moment. Outlet supply air from CCHS-C is supplied to the conditioned room.

Meanwhile, CCHS-H operates in regeneration process mode. The CCHS-H is heated by TE, and therefore, desiccant material is regenerated. The exhaust air, with high temperature and high humidity ratio from CCHS-H is exhausted to the environment. In the second cycle, as shown in **Figure 48**, CCHS-C and CCHS-H are switched into regeneration process and dehumidification process, respectively. By switching between the first and the second cycle, the whole desiccant dehumidification unit can realize a continuous process of moisture absorption and cooling. Figure 47 show the optimization the TED flowchart.

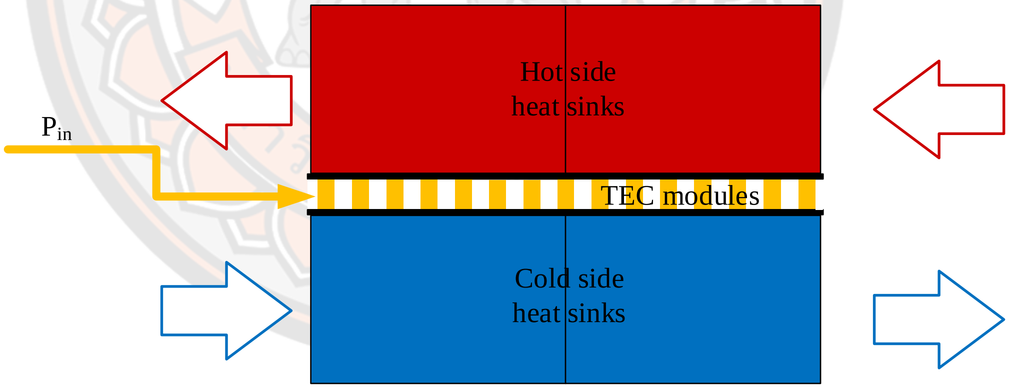

Figure 47 A schematic diagram of dehumidification process mode

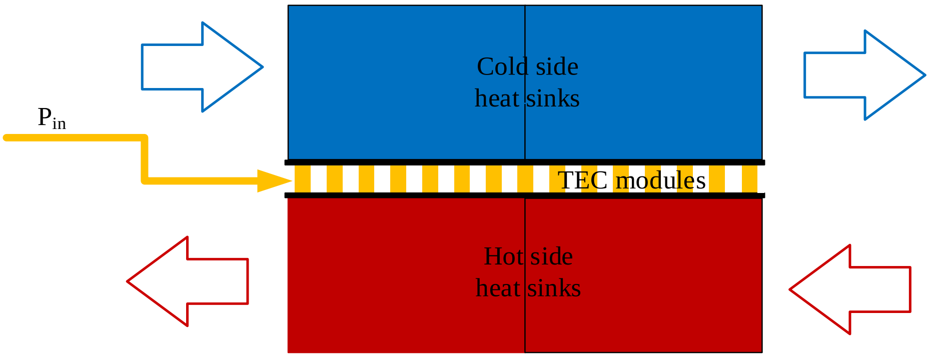

Figure 48 A schematic diagram of regeneration process mode

5. Numerical analysis of TED

The thermoelectric dehumidifier mechanism majorly depends on the TEC module. Hence, the mathematical relations and equations involved in defining TED's cooling capacity and performance are closely related to TEC. The cooling capacity and heat rejection from the hot side for TED can be defined as (152):

$$Q_c = \alpha I T_c - 0.5 I^2 R - K_t (T_h - T_c) \tag{74}$$

Where Q_c is the cooling capacity of TED. The heat transfer equation from the hot side is:

$$Q_h = \alpha I T_h - 0.5 I^2 R - K_t (T_h - T_c) \tag{75}$$

Where Q_h is the heat rejected from the hot side of TEMs. TED's electrical power input can be defined as the electrical power supplied to TEMs and heat sink fans (if any used) (153).

$$P_{TE} = \alpha I (T_h - T_c) + I^2 R \tag{76}$$

$$P_F = V_F I_F \tag{77}$$

Where P_{TE} and P_F are the input electric powers to TEM and heat sink fans, respectively. Here, in these equations I and I_F are the input current supplied to TEMs and heat sink fans, respectively. Moreover, V_F is heat sink fan input voltage. The term T_c and T_h are temperatures of cold and hot sides of TEM. Further, α (Seebeck coefficient), R (electric resistance) and K_t (total thermal conductance) can be defined as follows (154):

$$\alpha = \frac{V_{\max}}{T_h} \tag{78}$$

$$R = \frac{\left(\frac{V_{\max}}{T_h} - \Delta T_{\max}\right) V_{\max}}{T_h I_{\max}} \tag{79}$$

$$K_t = \frac{\left(T_h - \Delta T_{\max}\right) V_{\max} I_{\max}}{2 T_h \Delta T_{\max}} \tag{80}$$

Here, in Equations 78, 79, and 80 for TEMs, the terms $V_{\max}$, $I_{\max}$ and, $\Delta T_{\max}$ are the maximum voltage, electric current and the temperature difference between the two sides. Hence, the coefficient of performance (COP) for TED can be defined as (155)

$$COP = \frac{Q_c}{P_{TE} + P_F} \tag{81}$$

Riffat and Ma (156) suggested that the optimum current for the maximum COP is as follows

$$I_{opt} = \frac{K \Delta T \left(1 + \left(1 + Z T_m\right)^{0.5}\right)}{\alpha T_m} \tag{82}$$

Where Z is the figure of merit of the TE material, T_m is the average temperature between the hot and cold side of the TE, △T is the temperature difference across the TE.

A reversed Carnot cycle can be employed as a reversible refrigeration cycle, providing a measure of the maximum possible COP value for a refrigerating machine operating between two temperatures. The Carnot value of the COP for cooling (COP$_c$) is calculated by Ref. (87) as

$$COP_C = \frac{T_c}{(T_h - T_c)} \tag{83}$$

To compare the COP values of a TE cooling system and the Carnot cooling cycle, the COP ratio (C) is defined as the COP of the TE cooling system divided by the COP of the Carnot cooling cycle, calculated as

$$C = \frac{COP}{COP_c} \tag{84}$$

Exergy analysis of TED (157)

$$Ex_i - Ex_o - Ex_d = \frac{dEx}{dt} \tag{85}$$

Ex_i is exergy inflow (W), Ex_o is exergy outflow (W), and Ex_d is exergy destruction (W) $\frac{dEx}{dt} = 0$, when the TED is in a steady state. Hence, Equation (85) can be written as:

$$Ex_d = Q_c\left(1 - \frac{T_o}{T_c}\right) + P - Q_h\left(1 - \frac{T_o}{T_h}\right) \tag{86}$$

After solving this equation, the exergy destruction is

$$Ex_d = T_o\left(\frac{Q_h}{T_h} - \frac{Q_c}{T_c}\right) \tag{87}$$

But $\left(\frac{Q_h}{T_h} - \frac{Q_c}{T_c}\right)$ is entropy generation $\left(S_g\right)$ in the TED

$$Ex_d = T_o S_g \tag{88}$$

T_o is Surrounding temperature (K or ^{o}C) S_g is Entropy generation (W K^{-1}). Hence, the second law efficiency η_{Ex} of the TE cooler on the basis of exergy destruction can be calculated as: Exergy efficiency

$$\eta_{Ex} = 1 - \frac{Ex_d}{Ex_s} \tag{89}$$

The exergy supplied Ex_s is the electrical power supplied to the TE modules. The total thermal resistance (R_{ohs}) of the conventional heat sink is expressed as

$$R_{ohs} = \frac{\left(T_{hhs} - T_{amb}\right)}{Q_h} \tag{90}$$

Where T_{amb} is the ambient temperature, T_{hhs} is the hot-side temperatures of the TE module.

Theoretically, the maximum power output of a realistic TE module takes into account the contact resistance and the conversion efficiency as given by Rowe and Min (158).

$$P = \frac{\alpha^2}{2\rho} \frac{NA\left(T_h - T_c\right)^2}{\left(L+n\right)\left(1+2r\,L_c/L\right)^2} \tag{91}$$

$$\eta_{TE} = \left(\frac{T_h - T_c}{T_h}\right)\left\{\left(1+2rL_c\,/\,\mathrm{L}\right)^2\left[2-0.5\left(\frac{T_h - T_c}{T_h}\right)+\frac{4}{ZT_h}\left(\frac{L+n}{L+2rL_c}\right)\right]\right\}^{-1} \tag{92}$$

Where T_h and T_c are the hot side and cold side of thermoelectric, respectively.

Typically, n =0.1 mm, r =0.2, L =1.2 mm, L_c =0.8 mm, α =2.0 x 10^{-4} VK^{-1}, N =127 couples, ρ =1.0 x10^{-3} Ω cm, $Z = 1.565 \times 10^{-3}$ K^{-1} and, A = 1.96 mm^2.

Moisture removal capacity (MRC) shows the amount of moisture removed in the air passing the desiccant wheel. MRC is the calculation of the desiccant wheel sorption rate. The formulation of the MRC is presented as

$$MRC = \overset{\leftrightarrow}{m}_{a,deh}\left(W_{in} - W_{out}\right) \tag{93}$$

Where $\overset{\leftrightarrow}{m}_{a,deh}$ is the mass flow rate of dehumidification process air in (kg s^{-1}), and W in term of humidity ratio ($\mathrm{kg_w/kg_{da}}$)

Moisture removal regeneration (MRR) is the desiccant wheel's performance in removing moisture from its desiccant surface. The formulation of MRR is presented as

$$MRR = \overset{\leftrightarrow}{m}_{a,reg}\left(W_{in} - W_{out}\right) \tag{94}$$

Where $\overset{\leftrightarrow}{m}_{a,reg}$ is the mass flow rate of regeneration process air in (kg s^{-1}), and W in term of humidity ratio ($\mathrm{kg_w/kg_{da}}$)

Dehumidification effectiveness E_{deh} represents the ratio between the humidity reduction across the heat exchanger and the inlet humidity ratio

$$Dehumidification\ effectiveness = \frac{W_{in} - W_{out}}{W_{in}} \tag{95}$$

Where W in term of humidity ratio (kg_w/kg_{da})

The calculation of the amount of regeneration heat consumed for desorbed water is given in the regeneration effectiveness $\left(E_{reg}\right)$

$$Regeneration\ effectiveness = \frac{W_{in} - W_{out}}{W_{in}} \tag{96}$$

Where W in term of humidity ratio (kg_w/kg_{da})

The experimental error of the independent variables, such as temperature and input electrical current, is determined by the accuracy of the corresponding instrument. While the experimental error of the dependent variables, including the moisture removal rate and COP the overall system can be calculated from the experimental error of the independent variables according to the theory of error propagation. The relative error (RE) of the dependent variable y is calculated as follows (159):

$$RE = \frac{dy}{y} = \frac{\partial f}{\partial x_1}\frac{\partial x_1}{y} + \frac{\partial f}{\partial x_2}\frac{\partial x_2}{y} + \ldots\frac{\partial f}{\partial x_n}\frac{\partial x_n}{y} \tag{97}$$

$$y = \int\left(x_1, x_2, \ldots x_n\right) \tag{98}$$

Where $x_i = (i = 1 \ldots n)$ is the variable of the dependent variable y, and $\frac{\partial f}{\partial x}$ is the error transferring coefficient of the variables.

The experimental relative mean error (RME) during the test period can be expressed as:

$$RME = \frac{\sum_{1}^{N} |RE|}{N} \tag{99}$$

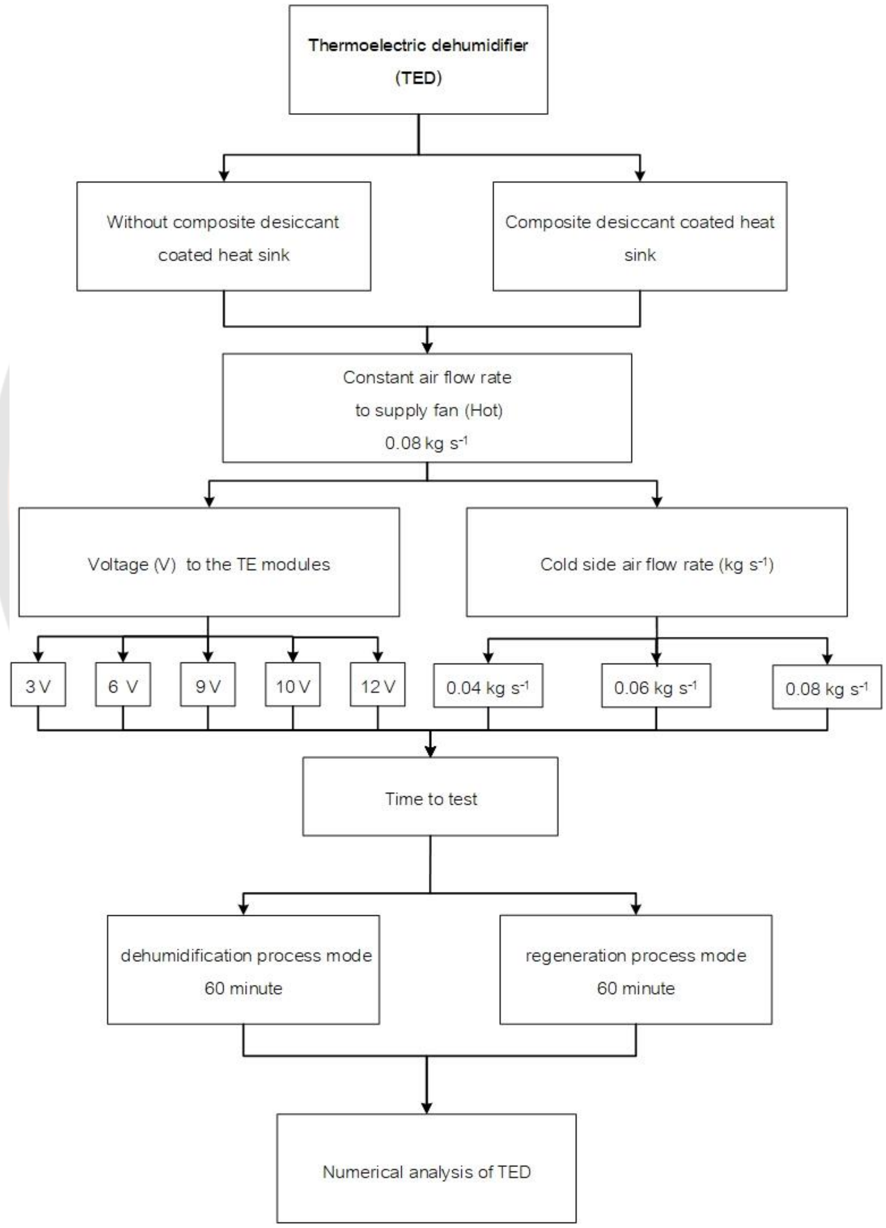

Figure 49 The optimization the TED flowchart

6. Measuring instruments

- To evaluate the power output of TED the following parameters were monitored and recorded.
- Temperature at hot and cold side
- Humidity and Temperature at the inlet-outlet of TED
- Humidity and Temperature at the cold-hot heatsink of TED
- Ambient air temperature and humidity
- Air velocity at the inlet-outlet of the cold-hot heatsink TED
- Direct Current of fans
- Direct Voltage of TEMs

1. Velocity Measurement (Testo model 454) is used to measure the air velocity at the outlet of cold heat sink. A wide range of hot bulb probes (diameter 0.3 mm, range of 0 to 10 m s^{-1}). The accuracy of the hot bulb probes is ±0.05 m s^{-1}. The air flow rate was calculated from the air velocity, measured by a hot wire anemometer (Testo model 445, accuracy 70.03 m s^{-1}) at the collector outlet, and the known duct area.

2. Multi meters (TES model 2800) was used to measure current output. RS 232 connected to computer. DC current range of 400 mAmp to 10 Amp and the accuracy ±0.2 %.

3. Multi meters (Hioki model 3801) was used to measure current output. RS 232 connected to computer. DC current range of 300 mAmp to 10 Amp, 20 mV to 800 V and the accuracy ±0.1 %.

4. Micro data logger (Hioki model LR8431 10 Ch) is used to record the temperature and DC voltage passing thermocouples. The measurement accuracy ±0.05%. Storage CF and USB Real time recording.

5. Temperature /humidity data logger Temperature logger LR5011 Measurement range (-40-180 ^{o}C) Accuracy (±0.5 ^{o}C) Storage 60,000 data

6. Arduino sensor DHT22 Power supply 3.3-6 V DC Polymer capacitor Operating range RH (0-100%); Temp (-40-80 ^{o}C) Repeatability RH (±1%); Temp

(±0.2 °C) Dimensions 14×18×5.5 mm. Humidity range 0–100%- Operating voltage 3-5 VDC- Max current of measurement 2.5 mA-Accuracy rate ± 2%

7. Micro SD card modules Power supply 3.3-5.5V DC

8. A Testo humidity sensor (accuracy ±3% RH) was used to record the relative humidity of the cold air.

9. Computer monitoring Component Computer Arduino software Arduino board Mega 2560

10. Microcontroller NodeMCUESP8266 802.11 (Wi-Fi) 2.4 GHz-32-bit of low power CPU- Operating voltage 5VDC

11. Tesco Temperature camera Testo-872 Thermal image Measuring range -30 to +100 °C; 0 to +650°C Accuracy ±0.2°C

12. Thermocouple wires of type k (Copper-constantan, diameter 0.15 mm and range -0 to 1250 °C) are used to record temperature of the hot and cold sides of the TE modules, the fin heat sinks, and the hot and cold air. The error of thermocouple type T and recorder was calibrated by temperature calibrator (Model X45L). Were calibrated by standard testing from 20-150 °C, which is the temperature range in this research.

CHAPTER IV

RESULT AND DISCUSSION

This chapter describes the experimental results of three major experiments undertaken. Firstly, a recyclable method for the production of mesoporous silica nanostructure from bagasse ash of the sugar cane industry (topic 1). Secondly, development and characterization of composite desiccant-coated aluminum sheets (DCAS) (topic 2). Finally, thermoelectric dehumidifier (TED) without and with composite desiccant coated heat sink (topic 3).

In topic 1, the mesoporous silica was prepared using sodium silicate by the alkali extraction method. The effect of calcination for bagasse ash and sodium hydroxide (NaOH) concentration on synthesized mesoporous silica's microstructure, morphology, and pore characteristics was investigated.

In topic 2, composite DCAS with varying LiCl mass concentrations were created and analyzed. This can certainly provide an in-depth understanding of the reaction mechanism during the adsorption/desorption operations on LiCl concentration, thus, leading to valuable information for the advancement of composite desiccant materials. The texture properties, as well as the microstructure properties, were studied. To determine and analyze sorption kinetics, the linear driving force (LDF) model was used. Moreover, the thermal conductivity was measured and discussed. To fit the experimental data, three moisture sorption isotherm models were used: the BET model, the GAB model, and the DLP model. This composite desiccant material as the most suitable desiccant is applied in topic 3.

In addition, topic 3 to evaluate the operation of the TED with and without composite desiccant, as well as to determine the relationship between the input electrical voltage and the cold air flow rate, which may be used to optimize the design of comparable TEDs. The dehumidification capacity of with and without composite desiccant was investigated.

A Recyclable method for production of mesoporous silica nanostructure from bagasse ash of sugar cane industry

1. Effect of calcination for bagasse ash

Before we synthesize mesoporous silica, the sugar factory's bagasse ash was heat treatment to form a powdered. According to the XRF analysis, the bagasse ash composition mainly comprises SiO_2 and oxides in **Table 13**. Moreover, were conducted to determine suitable calcination times. The result of XRF, the chemical composition ash after calcined at 600 ^{o}C for 6 h presented the highest silica content of 80.81 wt.%. According to our previous research Ribeiro and Morelli (137), study the effect of the calcination temperature on the pozzolanic activity of Brazilian sugar cane bagasse ash (SCBA), obtained under controlled calcination (500, 600, and 700 °C). The XRD results, the SCBA calcined at 600 °C, show a higher amorphous character.

Table 13 Chemical composition of bagasse ash before and after calcination at 600 ^{o}C 4 h and 6 h

Components expressed as oxides.	**Al_2O_3**	**SiO_2**	**P_2O_5**	**SO_3**	**K_2O**	**CaO**	**TiO_2**	**Mn_2O_3**	**Fe_2O_3**	**ZnO**
Before calcination	5.01	63.12	3.62	2.62	7.99	8.82	1.04	0.53	7.25	0.00
Calcination 600 ^{o}C 4 h	4.73	71.7	3.03	2.04	4.53	5.34	0.54	0.31	3.97	0.05
Calcination 600 ^{o}C 6 h	4.30	80.81	1.84	1.69	2.54	3.39	0.53	0.27	2.41	0.05

The chemical composition of ash, after calcination at 600 °C for 4 and 6 h. The result SiO_2 content and other components are different. Because some elements decompose at the point below 600 °C, for example, Phosphorus, Potassium Aluminum, and organic compound decompose at 240 to 490 °C. Moreover, some oxide compound increases because of the thermal degradation of hydrocarbon. The same as some oxide compound decreases because of thermal degradation.

The SiO_2 content at calcination 6 h with the same temperature is higher than that of calcination 4 h due to the organic compound decreasing at a higher 450 °C. Besides, the contaminate, alkaline, Potassium, Sodium, and Alumina decrease when the temperature increase due to the lignocellulosic material decomposed at this temperature range (160). The ashes resulting from calcination to these times were mineralogically analyzed crystallographic structure by XRD shown in **Figure 50**; the XRD pattern of bagasse ash shows many diffraction peaks, which indicates the presence of crystalline structure from the alpha phase silica (SiO_2), calcium silicate, and calcium aluminate phases. The increase of the amorphous character of bagasse ash can be visualized (XRD background, where the present amorphous, nondiffracting component causes the hump). Thus, it observed that the ashes' reactivity increases when the heat treatment time increased, which agrees with the chemical composition results (**Table 13**). The diffraction peaks have consentient JC-PDS 46-1045 Quart-syn-SiO_2 with a Primitive-Hexagonal structure.

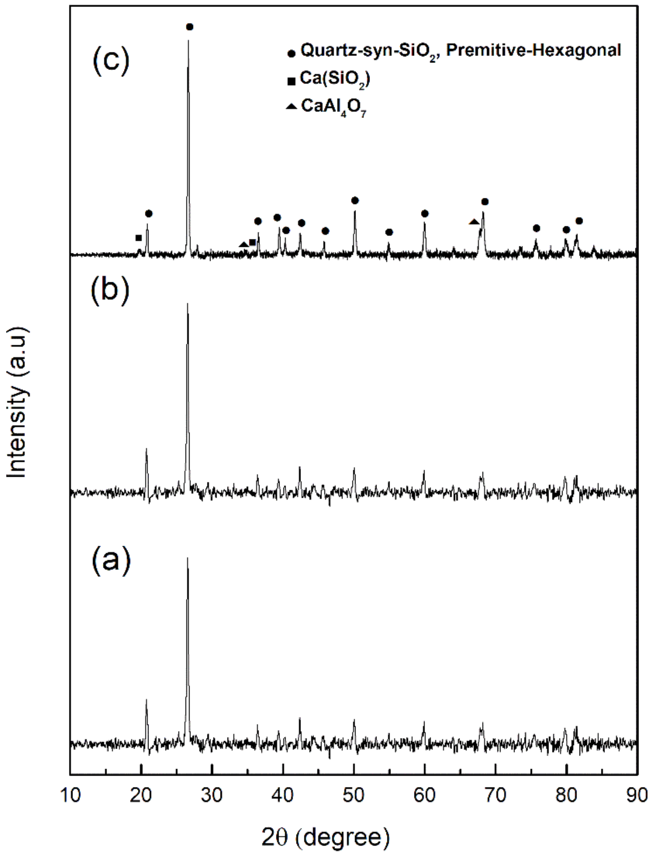

Figure 50 X-ray diffraction (XRD) pattern of bagasse ash, (a) before calcination, (b) calcination at 600 °C 4 h, and (c) calcination at 600 °C 6 h

Heat treatment also changes some physical characteristics of the powder that might affect its reactivity. The bagasse ash morphology from differing heat treatment times is shown in **Figure 51**. According to XRD results, the bagasse ash obtained at 600 °C 6 h has a higher amorphous character, confirmed in the SEM images (**Figure 51**), and shows a tangled phase without a well-defined format. The composition of the bagasse ash was mainly composed of carbon and silicium, according to EDS analysis.

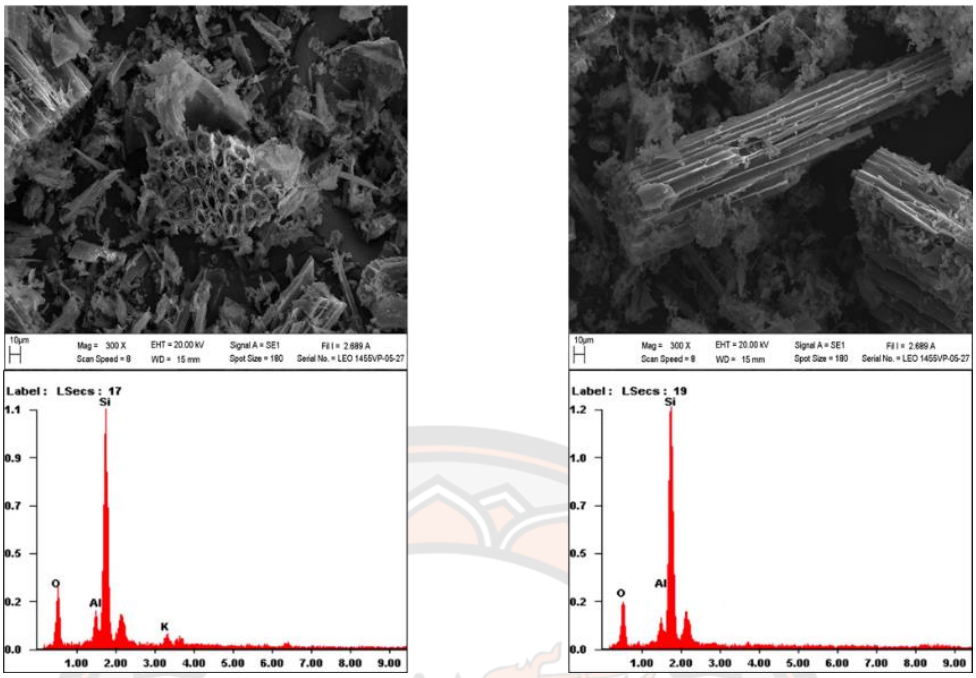

(a) (b)

Figure 51 The scanning electron micrograph (SEM) image and EDS of bagasse ash before after calcination at 600 ^{o}C, (a) 4 h and (b) 6 h

2. Effect of NaOH concentration on mesoporous silica

According to a previous study, bagasse ash calcined at 600 °C for 6 h was selected as a starting material for the synthesis of the mesoporous silica by the alkaline extraction method. The concentration of sodium hydroxide (NaOH) was varied from 1.0 to 2.5 N under the gelation pH of 7 and the aging time of 18 h. The effect of NaOH concentration variation on the percentage yield of silica is shown in **Figure 52**. With increasing NaOH concentration, the yield of silica increased from 51.24% for 1.0 N NaOH to 66.21% for 1.5 N and then reached the maximum value of 91.73% at 2.0 N. Further increase of NaOH concentration to 2.5 N resulted in a slight decrease in percentage yield from 91.73 to 89.08%.

This can be explained by the fact that as the concentration of NaOH increases, so does the concentration of OH- ions in the solution, which are readily available to react with the silica in bagasse ash, as described in Equation (100). Silica is a polycondensation polymer of silicic acid ($SiOH_4$), and the reaction in water is catalyzed by OH- ions through hydrolysis, as shown in Equation (101) and (102) (161).

However, increasing the alkali concentration further can result in the formation of siloxane linkages from the existing silanol groups in the basic regime, resulting in the formation of a negative surface. The negative surface's electrostatic attraction to the excess OH- ions reduces the yield of silica (162).

$$2OH^{-} + SiO_2 \Leftrightarrow SiO_3^{2-} + H_2O \tag{100}$$

$$(OH)_3\,Si - OH + OH^{-} \rightarrow (OH)_3\,Si - O^{-} + H_2O \tag{101}$$

$$(OH)_3\,Si - OH + (OH)_3\,Si - O^{-} \rightarrow (OH)_3\,Si - O - Si(OH)_3 + OH^{-} \tag{102}$$

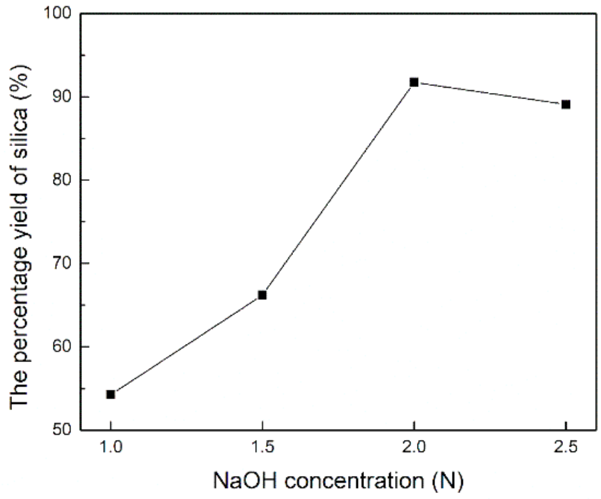

Figure 52 Effect of NaOH concentrations of 1.0, 1.5, 2.0, and 2.5 N on the percentage yield of silica

The XRD patterns of the silica produced from bagasse ash at different NaOH concentrations are shown in **Figure 53**. For all samples, a broad diffraction peak at 2θ = 22° to 25° was clearly observed, indicating the typical amorphous nature of silica (163) which may be attributed to the disordered cristobalite (164). Moreover, as the NaOH concentration increased to 2.0 N and 2.5 N, the sharp smaller peaks at 2θ ~ 38°, 45°, and 65°, which were previously observed at the 1.0 and 1.5 N NaOH concentrations, disappeared. The absence of these sharp peaks indicated a relatively high purity of silica, which is consistent with the percentage yield of silica demonstrated in **Figure 52**, where a high percentage yield of silica was observed at 2.0 and 2.5 N NaOH concentrations.

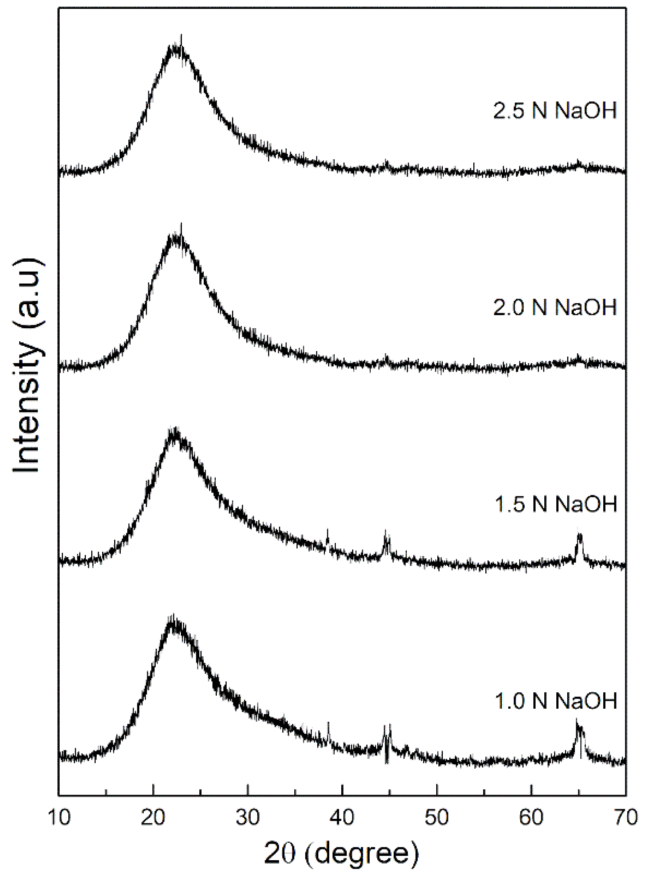

Figure 53 X-ray diffraction (XRD) pattern of silica produced from bagasse ash at different sodium hydroxide solution concentrations

The effect of varying the NaOH concentration on the specific surface area (a) and pore volume (b) of silica generated from bagasse ash is shown in **Figure 54**. The specific surface area of silica ranged from approximately 204 to 525 $m^2 g^{-1}$. The specific surface area (**Figure 54(a)**) of silica tended to increase when increasing NaOH concentration, peaking at 2.0 N and decreasing afterward. The pore volume (**Figure 54(b)**) of silica exhibited a similar trend to the specific surface area, which is increasing when increasing the NaOH concentration, peaking at 2.0 N, and then decreasing afterward. At NaOH concentrations (1.0, 1.5, and 2.0 N), an increase in specific surface area and pore volume is mostly attributed to increased sodium silicate salt deposition during precipitation. When the larger salt was washed out of the gel matrix, this left larger pores, resulting in increased surface area and pore volume. When the concentration of NaOH reached 2.5 N, the primary particles formed during neutralization cluster together and form a dense gel network. As a result, both the surface area and the volume of the pores decreased (165).

The pore size distributions of silica with the various NaOH concentrations are shown in **Figure 55** and **Table 14.** Silica prepared with 2.0 N NaOH has the narrowest peak compared to that of 1.0, 1.5, and 2.5 N, thus indicating that the pore sizes are the most uniform. Table 2 summarizes the specific surface area, the pore volume, and the pore size of silica produced from bagasse ash at different sodium hydroxide solution concentrations. The results show that silica pores obtained from 1.0, 1.5, and 2.0 N NaOH are mesopores while silica pores prepared from 2.5 N NaOH are macropores.

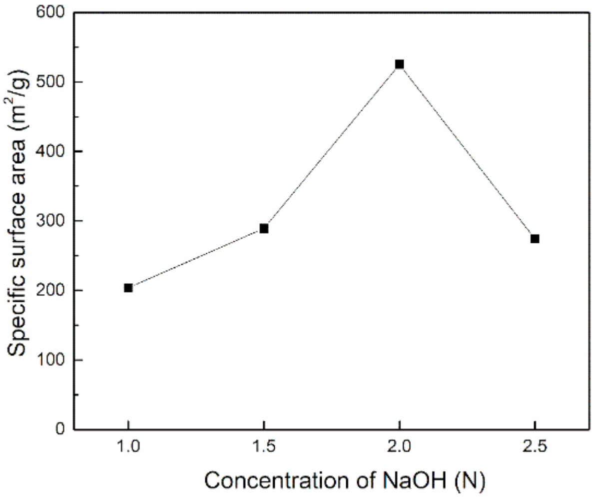

(a)

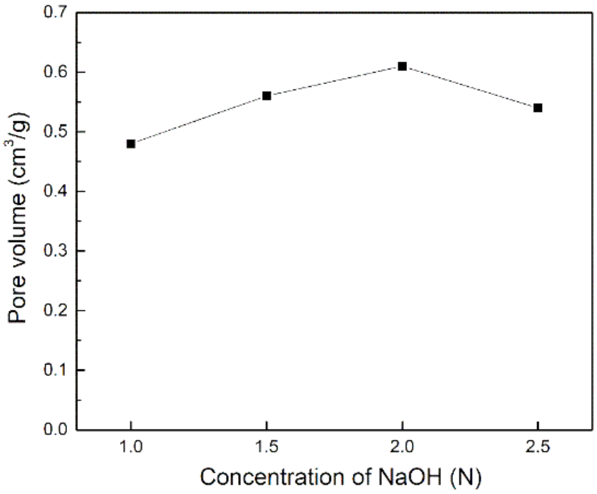

(b)

Figure 54 Effect of NaOH concentration, (a) the specific surface area, and (b) the pore volume of silica produced from bagasse ash

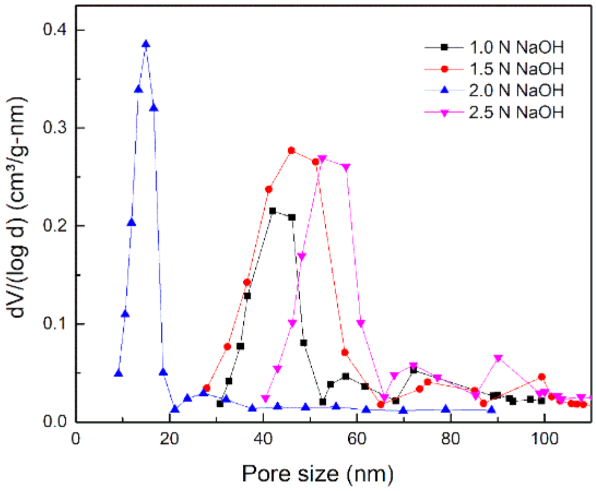

Figure 55 Pore size distributions of silica produced with various NaOH concentrations

Table 14 Effect of NaOH concentration on surface properties of silica produced from bagasse ash

NaOH concentration (N)	Specific surface area ($m^2\ g^{-1}$)	Pore volume ($cm^3\ g^{-1}$)	Pore size (nm)
1.0	204	0.48	40
1.5	289	0.56	47
2.0	525	0.61	15
2.5	274	0.54	58

The typical N_2 sorption isotherms for mesoporous silica produced prepared from bagasse ash with 2.0 N NaOH are presented in **Figure 56**. The obtained silica exhibited Type IV isotherms, as indicated by the disappearance of the hysteresis saturation limit, according to the IUPAC classification (166). This isotherm type is attributed to the indefinite multilayer formation after the monolayer has been completed. The result indicates that the prepared silica is mesoporous. In addition, the hysteresis observed was the H4 type. The two branches remain horizontally and parallel to each other over a wide P/Po range. Type H4 hysteresis was associated with narrow-slit pores (167).

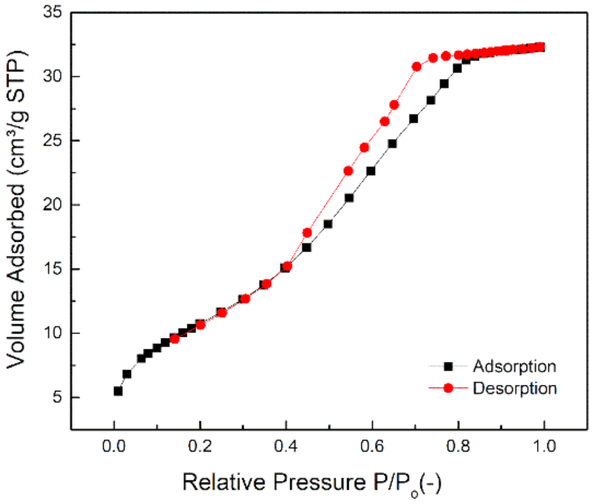

Figure 56 Nitrogen adsorption-desorption isotherms for mesoporous silica produced from bagasse ash with 2.0 N NaOH

Figure 57 shows the t-plot calculated from mesoporous silica produced from bagasse ash's nitrogen adsorption. Mesoporous solids exhibit an adsorption isotherm, and the resulting t-plot has two regimes (168). Before capillary condensation, adsorption occurs on mesoporous particles' internal and external surfaces. This line's slope (the blue line) gives the total specific surface, which is the sum of the mesoporous and external surface areas. Above condensation, adsorption only happens on the mesoporous external surface, so the t-plot was linear. After condensation, this linear regime's slope (the red line) gives the specific surface area of the external surface area only.

In this study, the mesoporous silica produced from bagasse ash with 2.0 N NaOH possessed a total surface area of 554 m^2 g^{-1} and an external surface area of 88 m^2 g^{-1}. The mesopore surface area of 466 m^2 g^{-1} was calculated by the difference between the total surface area and the external surface area. A good agreement was found between the surface area obtained from **Table 14** (525 m^2 g^{-1}) and the mesopore + external surface area (554 m^2 g^{-1}) determined by t-plot. Therefore, the differences in determining the surface area between the two methods were ± 29 m^2 g^{-1} or 5.5%.

Moreover, the total or mesopore volume can be extracted from the point where the second slope of the t-plot departs from the experimental data, which is found to be 0.61 mL g^{-1}. Both the specific surface area and the pore volume are consistent with the data in **Table 14**.

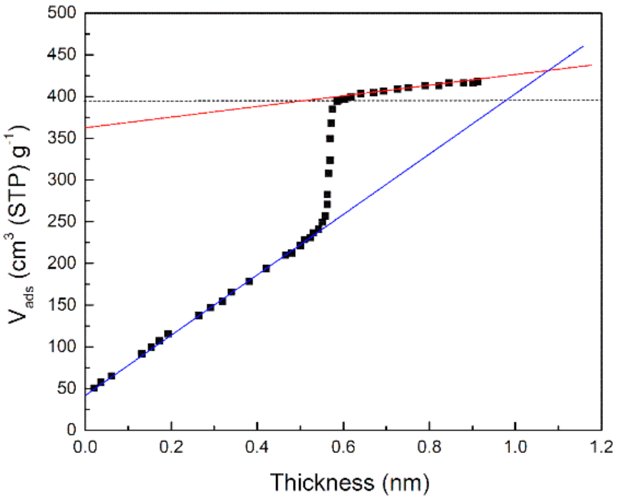

Figure 57 T-plot for nitrogen adsorbed in mesoporous silica produced from bagasse ash with 2.0 N NaOH

The FT-IR spectrum by adsorption band in the region of 4000 to 400 cm^{-1} for mesoporous silica produced from bagasse ash with 2.0 N NaOH is shown in **Figure 58.** The functional group of Si, O, and H has a wavenumber range of 4000 to 400 cm^{-1}. The absorption bands at 455.48, 796.91, and 1064.20 cm^{-1} are the consequence of the vibration of silica stretching and bending (Si-O-Si) (169, 170). The peak at 971.43 cm^{-1} is attributed to the silanol Si-OH stretching vibration group of silica (171, 172). Additionally, Figure 9 shows absorption bands at 3396.03 and 16333.81 cm^{-1}, which were caused by the adsorbed water's H-O-H stretching and bending vibrations, respectively (138). There were no additional absorption bands present. As a result, the FT-IR analysis verified that the mesoporous silica produced was composed entirely of pure silica particles.

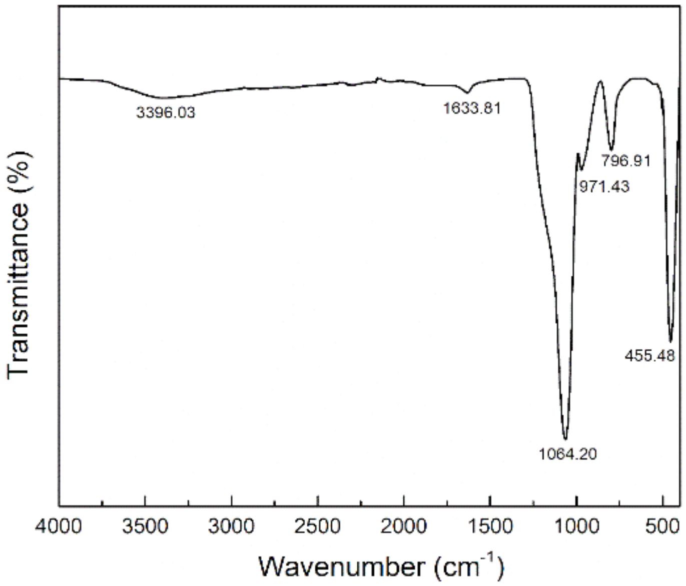

Figure 58 FT-IR spectra of mesoporous silica produced from bagasse ash with 2.0 N NaOH

Figure 59(a) shows the microstructure of mesoporous silica produced from bagasse ash with 2.0 N NaOH. The SEM image is observed to have agglomeration with irregular particle shapes, which have a size that varies from the nano to the micron order and is widely distributed. The surface was found to be rough and spherical. The EDS elemental analysis in **Figure 59(b)** shows that the mesoporous silica produced contains just the Si and O elements, which is consistent with the FT-IR spectra in **Figure 58**. Due to the acid washing step, the trace minerals in the bagasse ash were removed (138). **Figure 59(b)** confirms that the mesoporous silica produced consists of silica with high purity.

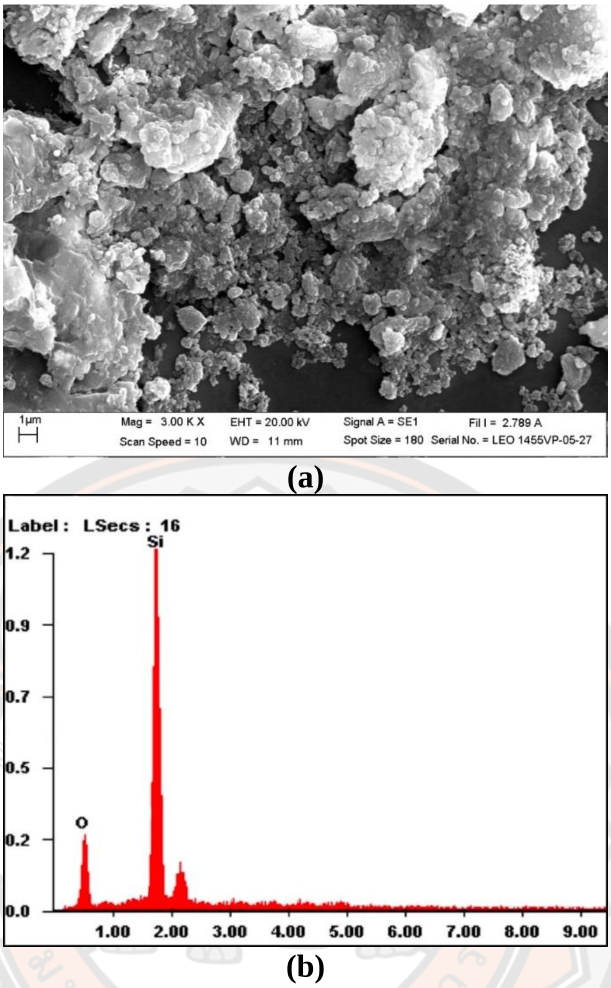

Figure 59 Mesoporous silica produced from bagasse ash with 2.0 N NaOH, (a) SEM image and (b) EDS

According to the experiment results on a recyclable method for production of mesoporous silica nanostructure from bagasse ash of the sugar cane industry, the silica gel produced in the first experiment has a specific surface area 525 (m^2 g^{-1}), which is similar to commercial silica gel. However, the silica gel content produced in the first experiment (the bagasse ash was burned at 600 ^{o}C for 6 h) was 0.87 g of silica gel from 100 g bagasse ash. Furthermore, because we needed a large amount of silica gel to coat the heat sink in Experiment 3 (thermoelectric dehumidifier (TED) with composite desiccant coated heat sink), we used commercial silica gel instead of synthesized silica gel to save money and energy on the synthesis of silica gel.

Development and characterization of composite desiccant-coated aluminum sheets (DCAS)

1. Thermal conductivity

The thermal conductivity for the DCAS is presented in **Figure 60**. In the result, the thermal conductivity of the DCAS varied from 3.0 to 6.1 Wm^{-1} K^{-1}, with all DCAS exhibiting good thermal conductivity due to the advantage of the aluminum sheet. Furthermore, the salt content of composite DCAS influenced thermal conductivity significantly. Compared to SGCAS (SG-L0), thermal conductivity increased by impregnating aluminum sheets with salt particles. Due to the immersed salt particles filling some pore space inside the silica, the highest thermal conductivity of composite DCAS (SG-L45) was approximately twice that of SGCAS (SG-L0) (139, 173).

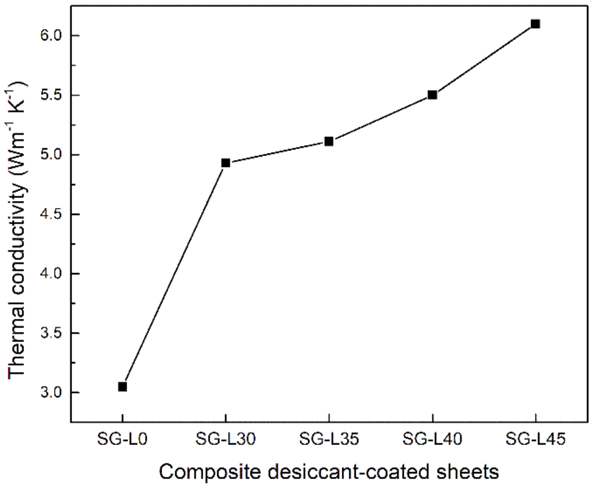

Figure 60 Thermal conductivity of the DCAS

2. Textural and morphological characterization

Table 15 shows the textural characteristics, including BET surface area (S_{BET}), pore volume (V_t), and average pore size (d_{av}) of DCAS. The calculated parameters were based on the unit mass. S_{BET} and V_t decreased as the mass concentration of LiCl solution in the impregnating solution increased. However,

S_{BET}* and V_t* were slightly reduced when salt content was considered. Salt surface complexes were formed as a result of various interactions between silica gel and LiCl during impregnation (174). A similar phenomenon was observed by a number of other researchers (46, 175-178). Furthermore, the d_{av} of composite DCAS decreased slightly due to the complex nature of the LiCl that formed on the silica surface during deposition. The formation of the LiCl layer completely or partially filled the small holes (46, 174). Consequently, d_{av} increased, decreased, or remained relatively constant.

Table 15 Texture characteristics of the composite DCAS

Composition	**Impregnating Concentration of LiCl (wt.%)**	**Salt Content (wt.%)**	**S_{BET} ($m^2\ g^{-1}$)**	**S_{BET}* ($m^2\ g^{-1}$)**	**v_t ($cm^3\ g^{-1}$)**	**v_t* ($cm^3\ g^{-1}$)**	**d_{av} (nm)**
SG-L0	0	0.00	208.10	-	0.31	-	3.71
SG-L30	30	12.38	89.59	115.86	0.21	0.18	3.69
SG-L35	35	14.29	117.33	146.39	0.18	0.23	3.86
SG-L40	40	17.14	128.55	162.92	0.21	0.26	3.74
SG-L45	45	20.95	59.49	110.10	0.10	0.17	3.68

*Salt content in DCAS was considered.

Figure 61 depicts the nitrogen sorption isotherms of the DCAS (SG-L0 to SG-L40), with silica gel as a comparison sample. The DCAS exhibited typical type IV isotherms at relative pressures ranging from 0.45 to 0.8, with a hysteresis loop at high relative pressure, according to the IUPAC classification (179). Type IV isotherms are commonly seen in mesoporous materials (with pores ranging in size from 2 to 50 nm) and indicate multilayer adsorption followed by capillary condensation (180). Furthermore, the shape of the pores in the studied material was determined by the type of hysteresis. The hysteresis loops for DCAS were of type H1, indicating agglomerates or spherical particles arranged fairly uniformly, as well as relatively high pore size uniformity and facile pore connectivity (181, 182). Furthermore, the capillary condensation process caused a rapid rise in nitrogen sorption at the beginning of the hysteresis loop. Moreover, at a relative pressure of about 1.0, the composite DCAS had a lower nitrogen sorption quantity than SGCAS (SG-L0), because the immersed salt particles blocked some of the silica gel's narrow pores (183). To further understand the pore structure in DCAS, pore size distributions were also analyzed, as shown in **Figure 62**. The DCAS showed a sharp peak in the mesoporous region at approximately 4 nm. However, because the immersed salt particles caused pore blockage, the amount of nitrogen sorption by the composite DCAS was significantly reduced.

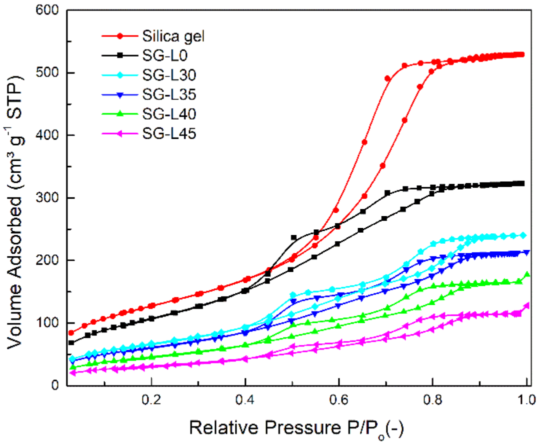

Figure 61 Nitrogen sorption isotherms of silica gel and DCAS

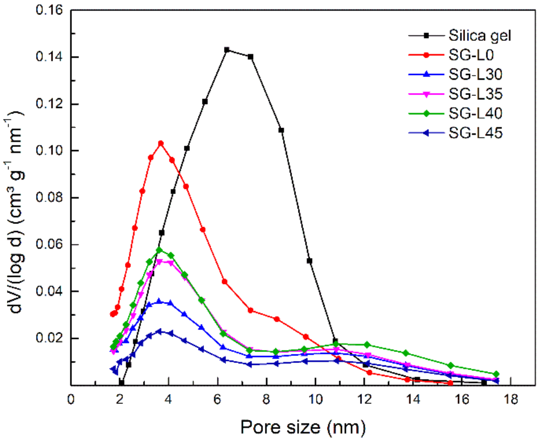

Figure 62 Pore size distributions of silica gel and DCAS

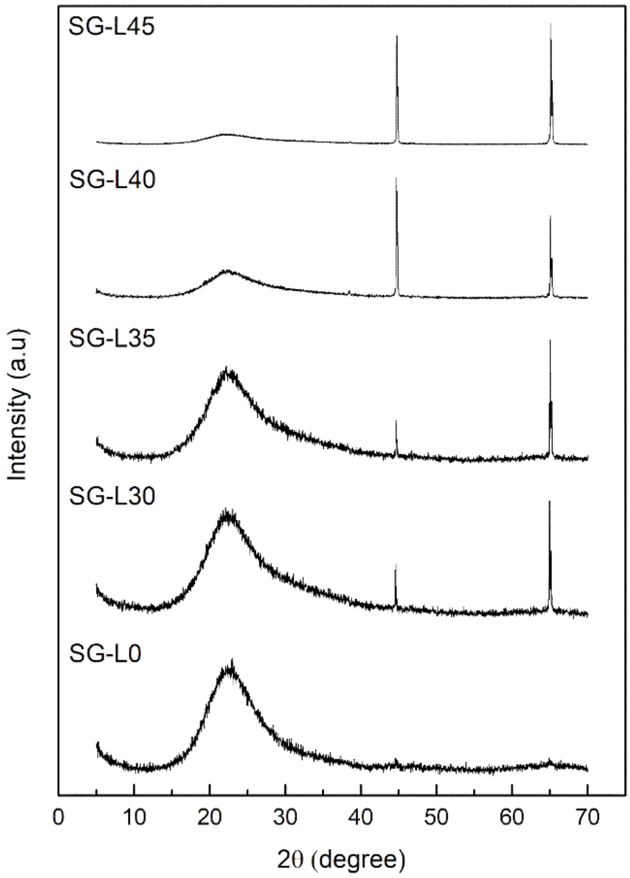

Figure 63 The X-ray diffraction (XRD) patterns of composite desiccant-coated aluminum sheets

The XRD patterns of the composite desiccant-coated aluminum sheet at different LiCl concentrations are shown in **Figure 63**. The broad diffraction peak at $2\theta = 15^o$ to 20^o was observed for all samples, indicating the typical amorphous state. Moreover, as the LiCl concentration increased to 30 wt.%, 35 wt.%, 40 wt.%, and 45 wt.%, the sharp peaks at $2\theta \sim 45^o$ and 65^o but at 0 wt.% of LiCl concentration disappeared. The XRD pattern appears that LiCl is well dispersed in the composite desiccant-coated aluminum sheet. The XRD pattern shows that LiCl exhibits amorphous to crystalline change as LiCl concentration in the composites increases.

Figure 64 shows scanning electron microscopy (SEM) images of the DCAS. When viewing the images from **Figure 64(b–f)**, it is clear that, as the mass fraction of LiCl increased, the LiCl gradually occupied the micro porosity of the silica pellet. It was demonstrated, however, that all composite DCAS had a salt layer that partially covers their matrix surface. LiCl was not entirely contained within the pores and was partially deposited on the outside surface of the grain. Furthermore, the SEM images show potential explanations for the thermal conductivity trend in **Figure 60** and the nitrogen sorption isotherm trend in **Figure 61.** Thermal conductivity initially increased with increasing LiCl concentrations for composite DCAS with the same silica gel ratio because composite DCAS had a more organized structure. Similarly, a higher LiCl concentration during the gas transfer decreased nitrogen adsorption because the silica gel may have been overly squeezed, leaving fewer empty spaces for gas passage.

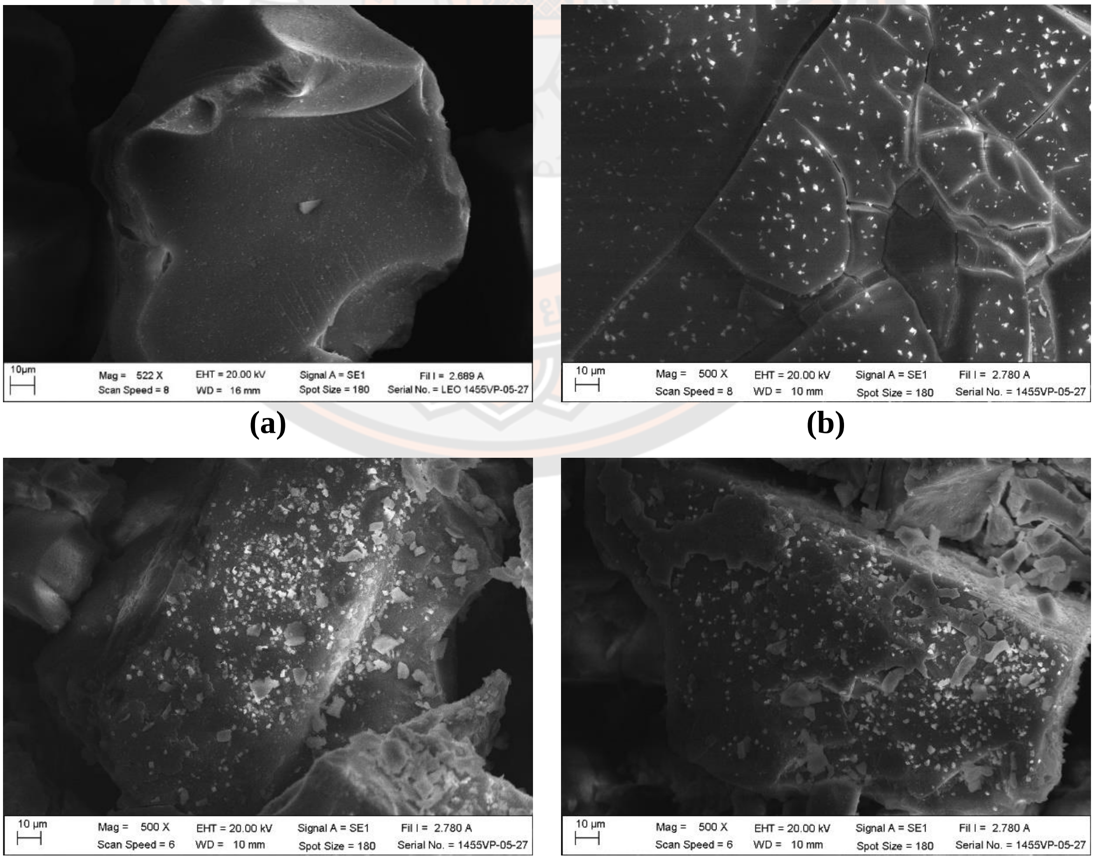

(a) **(b)**

(c) **(d)**

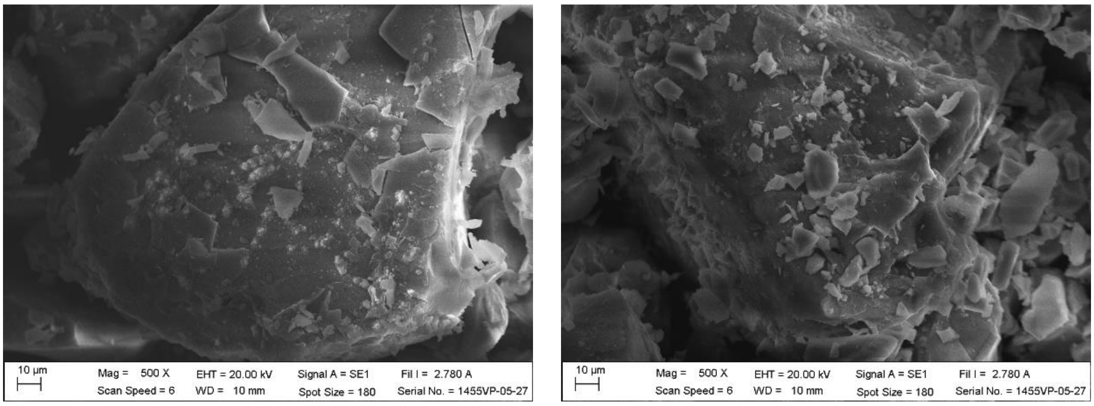

(e) **(f)**

Figure 64 The scanning electron microscopy (SEM) image of (a) Silica gel, (b) SG-L0, (c) SG-L30, (d) SG-L35, (e) SG-L40, and (f) SG-L45

3. Sorption kinetics

The water sorption kinetics of solid desiccant systems are essential since they can influence the cycle time. Experimental results are illustrated in **Figure 65**. During the initial stages of sorption, dynamic water sorption increased significantly for all DCAS. After that, as the amount of absorbed water approached saturation, it gradually increased. In comparison to SGCAS (SG-L0), composite DCAS demonstrated greater water sorption quantities and rates, indicating a collaborative contribution of the porous host matrix (silica gel) and impregnated salt particles (LiCl). The water sorption quantities of composite DCAS (SG-L40), after testing at 10, 30, and 60 min, were 0.22, 0.30, and 0.34 g g^{-1}, whereas the water sorption quantities of SGCAS (SG-L0) were 0.04, 0.09, and 0.12 g g^{-1}, respectively. This is due to the fact that water sorption through silica gel is a physical process, as opposed to through composite desiccants, which includes both chemical (salt hydration) and physical sorption(139).

Furthermore, because the composite DCAS had higher thermal conductivity than the SGCAS, the influence of the released sorption heat decreased, resulting in a shorter time required to reach sorption equilibrium. When the sorption time exceeded 20 min, the water sorption quantities increased significantly as the LiCl concentrations of the composite DCAS increased.

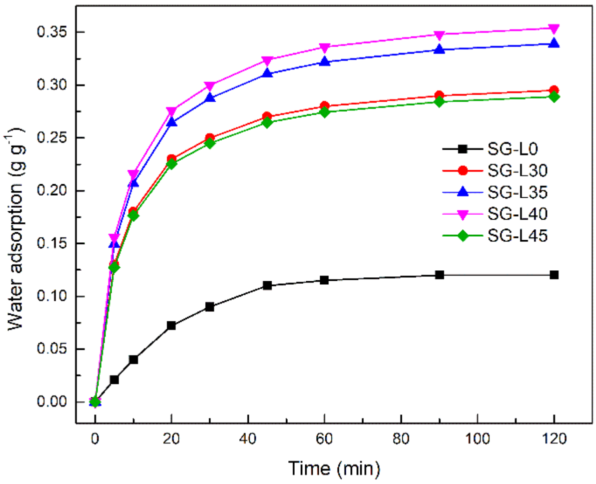

Figure 65 Water adsorption kinetics curves of DCAS

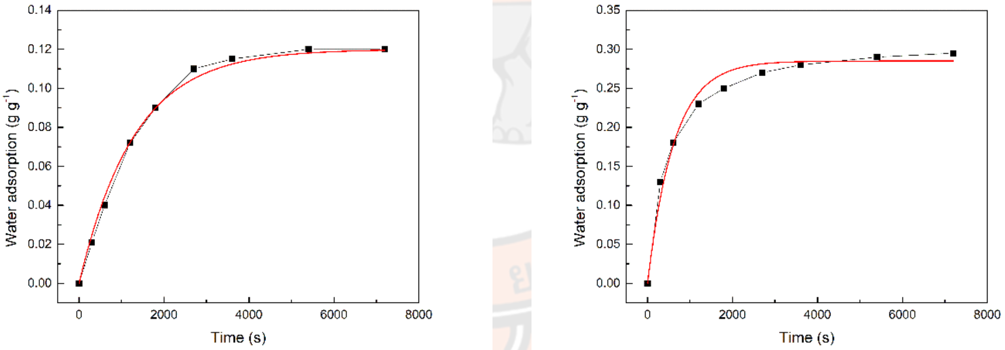

(a) SG-L0 **(b) SG-L30**

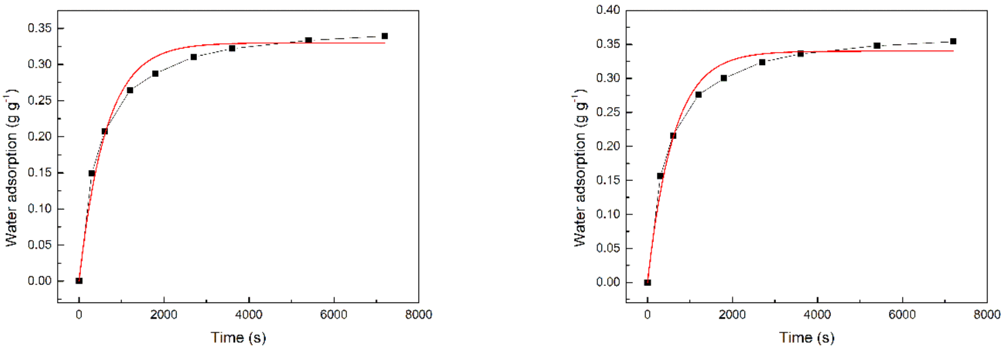

(c) SG-L35 **(d) SG-L40**

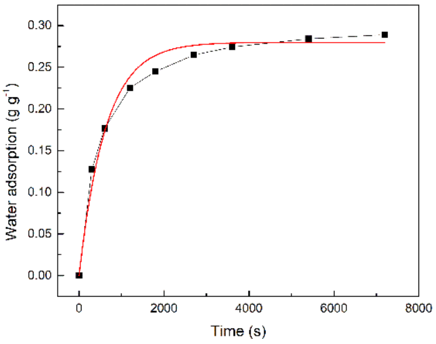

(e) SG-L45

Figure 66 The LDF model may be used to determine the adsorption rate of DCAS

The sorption rate coefficients (k) and coefficient of determination (R^2) of SGCAS (SG-L0) and composite DCAS (SG-L30 to SG-L45) were calculated (**Figure 66**), as shown in **Figure 67**. The sorption rate coefficients (k) of the DCAS ranged from 0.77×10^{-3} to 1.78×10^{-3} s^{-1}, which is approximately 1 time greater than SGCAS, indicating the positive effect of LiCl. The LDF model corresponded with well-measured data, with the coefficient of determination (R^2) ranging between 0.983 and 0.996 for all DCAS. When compared to SGCAS (SG-L0), the dynamic water sorption quantity and sorption rate coefficient significantly increased.

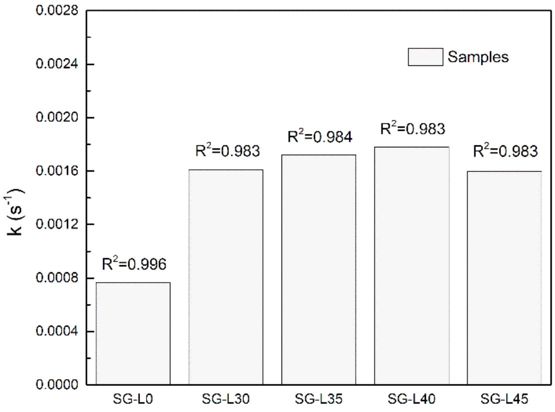

Figure 67 Sorption rate coefficients of DCAS

4. Moisture sorption isotherms

As shown in **Figure 68**, the VSA was used to study delicate moisture sorption isotherms on DCAS to better understand the mechanism of moisture sorption behavior of DCAS. The moisture content (%) of composite DCAS (SG-L40) was significantly higher than that of SGCAS (SG-L0) because of the highly hygroscopic salt LiCl contribution. However, moisture sorption isotherms indicated that composite DCAS (SG-L40) had a higher adsorption capacity, with a 20 to 30% greater water uptake than SGCAS (SG-L0). For DCAS, moisture content (%) increased as water activity (A_w) increased.

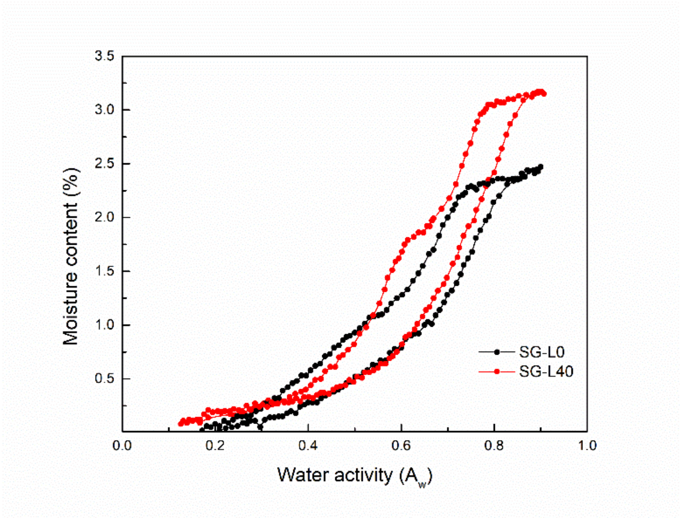

Figure 68 Moisture sorption isotherms of DCAS

5. Moisture sorption isotherms models

Table 16 shows that, regardless of sorption direction, the DLP model is the best fit for estimating the moisture sorption isotherms of DCAS (R^2 and RMSE), followed by the GAB and BET models, as shown in **Figure 69**. As expected, the BET model fitted sorption data quite well, but only in the water activity (A_w) range of 0 to 0.5. Only the GAB and BET models provided values for monolayer moisture content (m_0), which represent the adsorption potential and amount of water adsorbed to DCAS pore surface monolayer sites for each sorption direction. The higher m_0 values for composite DCAS (SG-L40) showed that this LiCl had a significant effect on sorption behavior, indicating that monolayer moisture content increased with increasing LiCl mass concentrations. Similarly, in the GAB model, the K value increased as the strength of the interactions between the water molecules and the adsorbent increased, compensating for differences in the characteristics of the multilayer molecules compared to the bulk liquid (173).

On the other hand, when the mass concentration of LiCl was increased, the interactions between surface groups and water molecules decreased, resulting in reduced c and c_1 value. Several layers of water molecules were arranged around each hydrophilic site during the formation of hydration monolayers. The sorption energy decreased as the distance between water molecules and the sorption site increased during the second hydration phase due to the progressive saturation of hydrophilic sites (184). The direction of sorption is explained by the DLP-fitting equation as given in **Table 17**, and it was possible to determine the moisture content (%) of DCAS with known initial water activity more quickly.

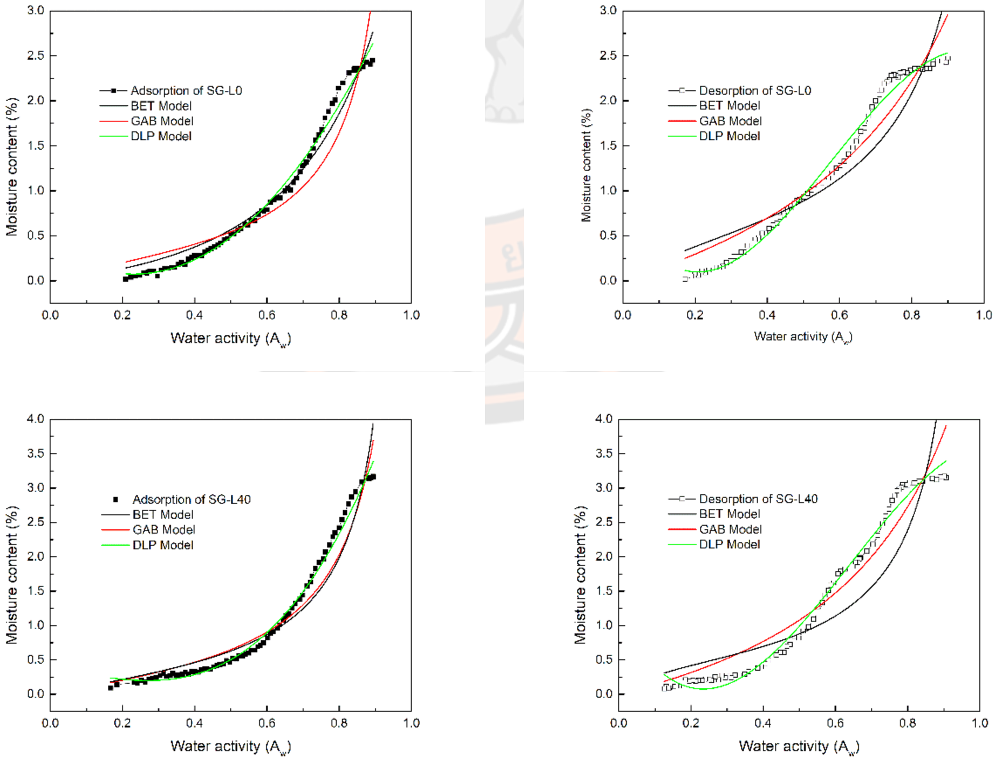

Figure 69 Estimated parameters of models for the sorption isotherms of DCAS

Table 16 Estimated parameters of models for the sorption isotherms of DCAS

Model	Para.	SG-L0		SG-L40	
		Adsorption	Desorption	Adsorption	Desorption
BET	c	3.33187	16.1423	2.62282	8.41901
	m_0	0.35426	0.40358	0.43488	0.49152
	R^2	0.91465	0.70074	0.92648	0.75911
	RMSE	0.2570	0.47098	0.26471	0.56232
GAB	c_1	1.60935	1.13943	1.46069	0.9858
	K	0.94432	0.70814	0.96112	0.7583
	m_0	0.50833	1.61023	0.56778	1.78218
	R^2	0.9516	0.93344	0.95263	0.93973
	RMSE	0.19354	0.22213	0.21248	0.28126
DLP	b_0	0.36629	0.78821	0.40107	1.15945
	b_1	-2.49502	-7.17614	-1.05856	-10.01023
	b_2	5.24140	21.08981	-0.49086	26.20371
	b_3	-2.49502	-12.18092	6.04448	-13.72783
	R^2	0.99198	0.98990	0.99255	0.98878
	RMSE	0.07878	0.08651	0.08428	0.12138

Table 17 Best fit equations for DCAS experimental sorption data

Composition	Sorption Direction	DLP Fitting Equations
SG-L0	Adsorption	$m = 0.44693x^3 + 5.2414x^2 - 2.49502x + 0.36629$
	Desorption	$m = -12.18092x^3 + 21.08981x^2 - 7.17614x + 0.78821$
SG-L40	Adsorption	$m = 6.04448x^3 - 0.49086x^2 - 1.05856x + 0.40107$
	Desorption	$m = -13.72783x^3 + 26.20371x^2 - 10.01023x + 1.15945$

* m is the moisture content (%) and x is the water activity (A_w)

6. Dehumidification performance

To investigate the application of composite desiccants further, a TED with a composite (SG-L40-DCHS) and silica gel (SG-L0-DCHS)-coated heat sink was built with a desiccant thickness of 1.5 mm. A schematic of the structure of the TED is illustrated in **Figure 70(a)**. The TED comprised twelve thermoelectric (TE) cooling modules (TEC1-12708) sandwiched between four aluminum, rectangular heat sinks (two for hot and two for cold air), as shown in **Figure 70(b)**. The TE modules were connected in series and arranged in two rows, each containing six TE modules. A total of four direct-current (DC) blowers were employed: two for the hot side, which were primarily used to assist in transferring excess heat to the environment, and two for the cold side, which were used to improve the convection of the air moving through the fin heat sink on the cool side. During the experiment, an electrical voltage was supplied to the TE modules at different voltages of 3, 6, 9, and 12 V, respectively. The cycle time was set at 60 min. The humidity ratio and velocity of the input air were 13.19 g kg^{-1} and 1.2 m s^{-1}, respectively.

The dehumidification system comprised two dehumidifier units. One of the dehumidifier units worked on the dehumidification process, so it was supplied with the cold side of the TE modules to adsorb moisture in ambient air, whereas the other worked on the regeneration process, so it was supplied with the hot side of the TE modules to remove water from the saturated desiccant. These two dehumidifiers worked simultaneously; while one dehumidified the working air, the other was regenerated. The two switched their operations periodically to achieve dehumidification of the work in process.

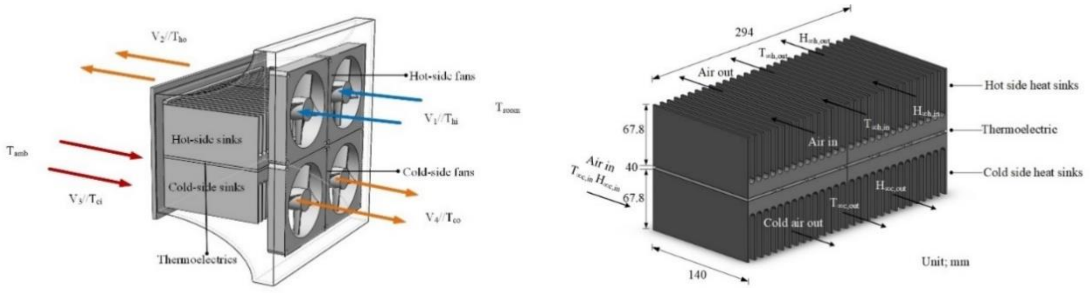

(a) **(b)**

Figure 70 Schematic of (a) thermoelectric dehumidifiers (TED) and (b) the air-to-air TED system.

Figure 71 shows the effect of increasing the electrical voltage on the cold and hot sides of the thermoelectric module. For the tests, four different voltages were used: 3, 6, 9, and 12 V. The cold-side temperature decreased from 45 to 19 °C as the electrical voltage increased. Meanwhile, when the electrical voltage increased, the temperature on the hot side increased. The maximum temperature on the hot side was 45 °C at 12 V. The minimum temperature on the cold side was 19 °C at 9 V. The higher the electrical voltage, the lower the temperature on the cold side and the higher the temperature on the hot side.

Figure 72 compares the dehumidifying processes under different input electrical voltages of the thermoelectric module. It can be seen that the outlet air humidity ratio depended strongly on the input electrical voltage of the thermoelectric module. In this experiment, when the input electrical voltage was 3, 6, and 9 V, the outlet air humidity ratio (**Figure 72(a)**) reached 12.40, 12.34, and 12.26 g kg^{-1} for SG-L0-DCHS and 11.62, 11.46, and 10.23 g kg^{-1} for SG-L40-DCHS.

In contrast, for the input electrical voltage of 12 V, the outlet air humidity ratio showed an increasing tendency. The outlet air humidity ratio was 11.53 g kg^{-1} for SG-L0-DCHS and 10.43 g kg^{-1} for SG-L40-DCHS, respectively. As a result, the outlet air temperature tended to be the same as the humidity ratio (**Figure 72(b)**).

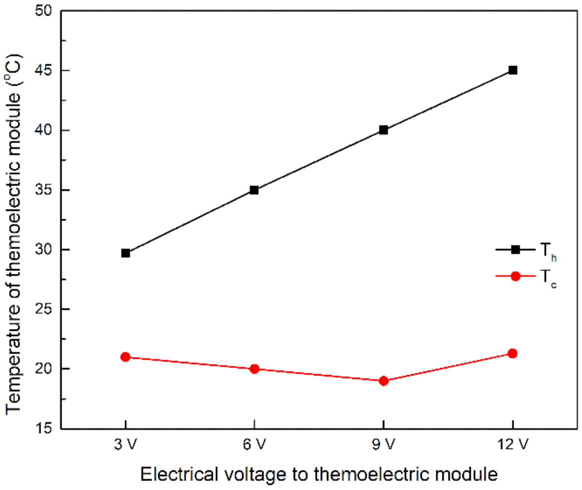

Figure 71 Hot- and cold-side temperatures of thermoelectric module versus electrical voltage (hot-side air flow rate: 0.034 $m^3\ s^{-1}$, cold-side air flow rate: 0.017 $m^3\ s^{-1}$)

This result is explicable by the material properties of thermoelectric modules. The heat absorbed from the ambient by a thermoelectric module came from two sources: one due to the Peltier effect, which is proportional to the module's current, another the Joule effect, which is proportional to the square of the current passing through the module. When the input voltage was too low, the Peltier effect was ineffective, resulting in a slow rate of dehumidification. On the other hand, when the input voltage was excessive, the Joule effect took over, imposing a large heat load on the: one due to the Peltier effect, which is proportional to the module's current, another the Joule effect, which is proportional to the square of the current passing through the module. Once the generated heat could not be dissipated into the ambient, it was transferred to the cold side via heat conduction, thereby weakening the condensing heat transfer on the fin heat sink.

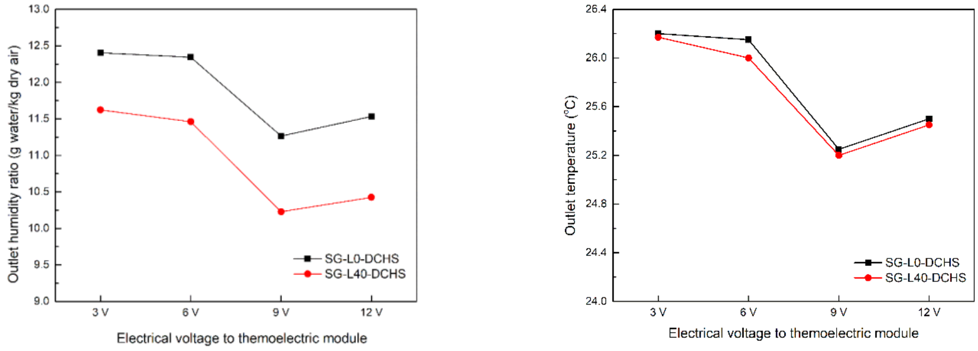

(a) **(b)**

Figure 72 The outlet air (a) humidity ratio and (b) temperature under different electrical voltages to thermoelectric module (hot-side air flow rate: 0.034 m^3 s^{-1}, cold-side air flow rate: 0.017 m^3 s^{-1})

Dehumidification capacity is one of the most critical performance indicators in the DCHS system, and was determined using the following Equation (14).

$$Q_{de} = m_a \left(\int_0^{t_{de}} (w_{ai} - w_{ao}) dt \right) / t_{de} \qquad (103)$$

Where, Q_{de} is dehumidification capacity (kg h^{-1}), m_a is the mass flow rate of process air (kg s^{-1}), w_{ai} and w_{ao} are humidity ratios of process air at the inlet and outlet (g kg^{-1}), and t_{de} is dehumidification time (s).

Figure 73 shows the Q_{de} of the DCHS using the TED. With increasing electrical voltage to the thermoelectric module, the Q_{de} increased from 0.031 kg h^{-1} at 3 V to 0.034 kg h^{-1} at 6 V and then reached the maximum value of 0.076 kg h^{-1} at 9 V. A further increase of electrical voltage to 12 V resulted in a slight decrease in the Q_{de} from 0.076 to 0.066 kg h^{-1} for SG-L0-DCHS. Similarly, the Q_{de} of SG-L40-DCHS, after testing at 3, 6, 9, and 12 V, was 0.062, 0.069, 0.117, and 0.110 kg h^{-1}, respectively. Additionally, SG-L40-DCHS removed more moisture from the process air, which was approximately 1 time greater than SG-L0-DCHS. This was due to the combined effect of silica gel with impregnated LiCl.

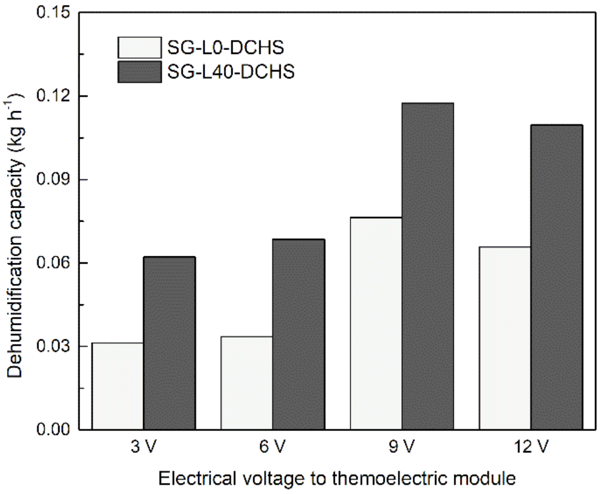

Figure 73 Dehumidification capacities of DCAS under different voltage (V) to thermoelectric

Thermoelectric dehumidifier (TED) without composite desiccant coated heat sink

1. Temperature profiles

Figure 74 and **Table 18** shows the temperature profiles of TED at the temperature of the hot (T_h) and cold (T_c) sides of the thermoelectric module. The temperature at the hot (T_h) and cold (T_c) sides of the thermoelectric module depends on electrical voltage. **Figure 74(a)-74(c)** shows the temperature profiles of temperature of the hot and cold sides of the thermoelectric module. It can be seen that the trend line of temperatures of electrical voltage are similar. **Figure 74** shows the effect of increasing the electrical voltage on the cold and hot sides of the thermoelectric module. For the tests, four different voltages were used: 3, 6, 9, and 12 V. At cold-side air flow rate 0.04 kg s^{-1}, the cold-side temperature decreased from 45 to 19 °C as the electrical voltage increased. Meanwhile, when the electrical voltage increased, the temperature on the hot side increased. The maximum temperature on the hot side was 45 °C at 12 V. The minimum temperature on the cold side was 19 °C at 9 V. At cold-side air flow rate 0.06 kg s^{-1}, the cold-side temperature decreased from 45 to 20 °C as the electrical voltage increased. Meanwhile, when the electrical voltage increased, the temperature on the hot side increased. The maximum temperature on the hot side was 45 °C at 12 V. The minimum temperature on the cold side was 20 °C at 6 and 9 V. At cold-side air flow rate 0.08 kg s^{-1}, the cold-side temperature decreased from 46 to 21 °C as the electrical voltage increased. Meanwhile, when the electrical voltage increased, the temperature on the hot side increased. The maximum temperature on the hot side was 46 °C at 12 V. The minimum temperature on the cold side was 21 °C at 6 and 9 V. The higher the electrical voltage, the lower the temperature on the cold side and the higher the temperature on the hot side.

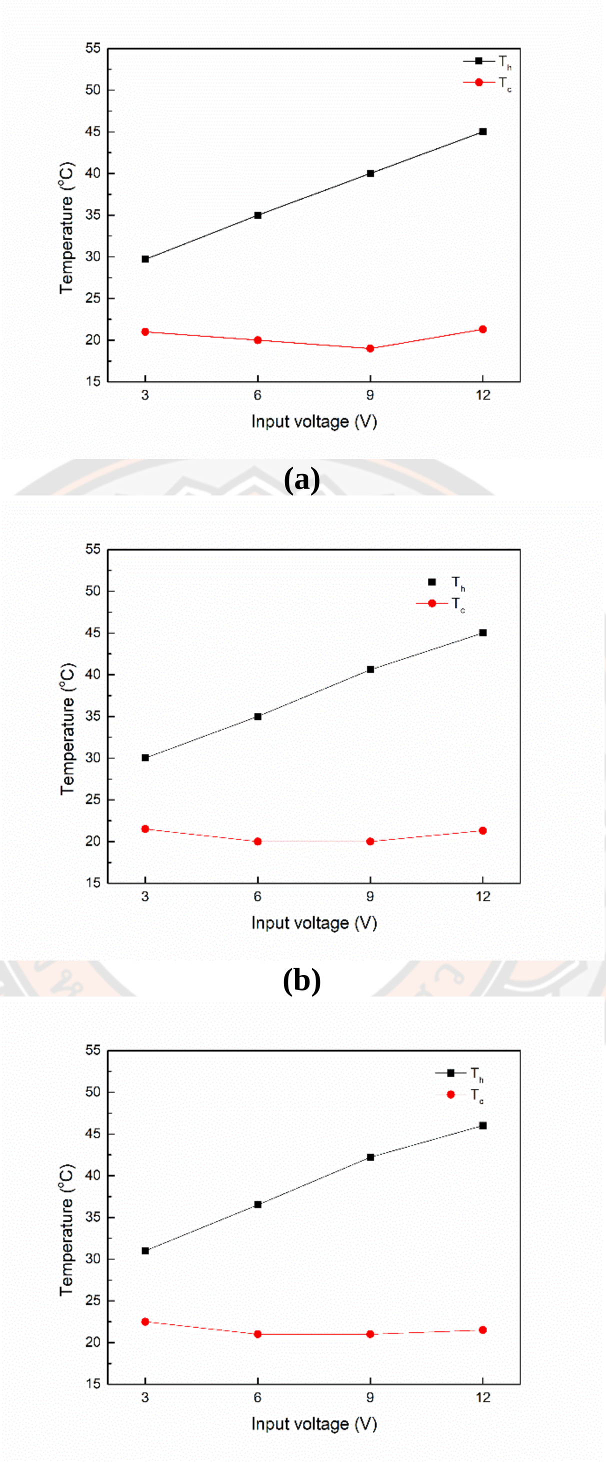

(a)

(b)

(c)

Figure 74 Hot- and cold-side temperatures of thermoelectric module versus electrical voltage (a) cold-side air flow rate: 0.04 kg s^{-1}, (b) 0.06 kg s^{-1}, and 0.08 kg s^{-1} (hot-side air flow rate: 0.08 kg s^{-1})

Table 18 The values of the temperature of the hot (T_h) and cold (T_c) sides of the thermoelectric module.

Cold-side air flow rate (kg s^{-1})	Input voltage to TE (V)	Temperature (°C)	
		T_h	T_c
0.04	3	29.7	21
	6	35	20
	9	40	19
	12	45	21.3
0.06	3	30	21.5
	6	35	20
	9	40.6	20
	12	45	21.3
0.08	3	31	22.5
	6	36.5	21
	9	42.2	21
	12	46	21.5

2. Effect of voltage supply

For a 60-minute test period, **Figure 75** to **Figure 77** shows the inlet and outlet temperature and humidity ratio (**Figure 78** to **Figure 80**). The outlet humidity ratio decreased from 13.19 g kg^{-1} to 12.18 g kg^{-1} for the TED, while the outlet temperature in the TED dropped by only about 0.5 to 2 °C.

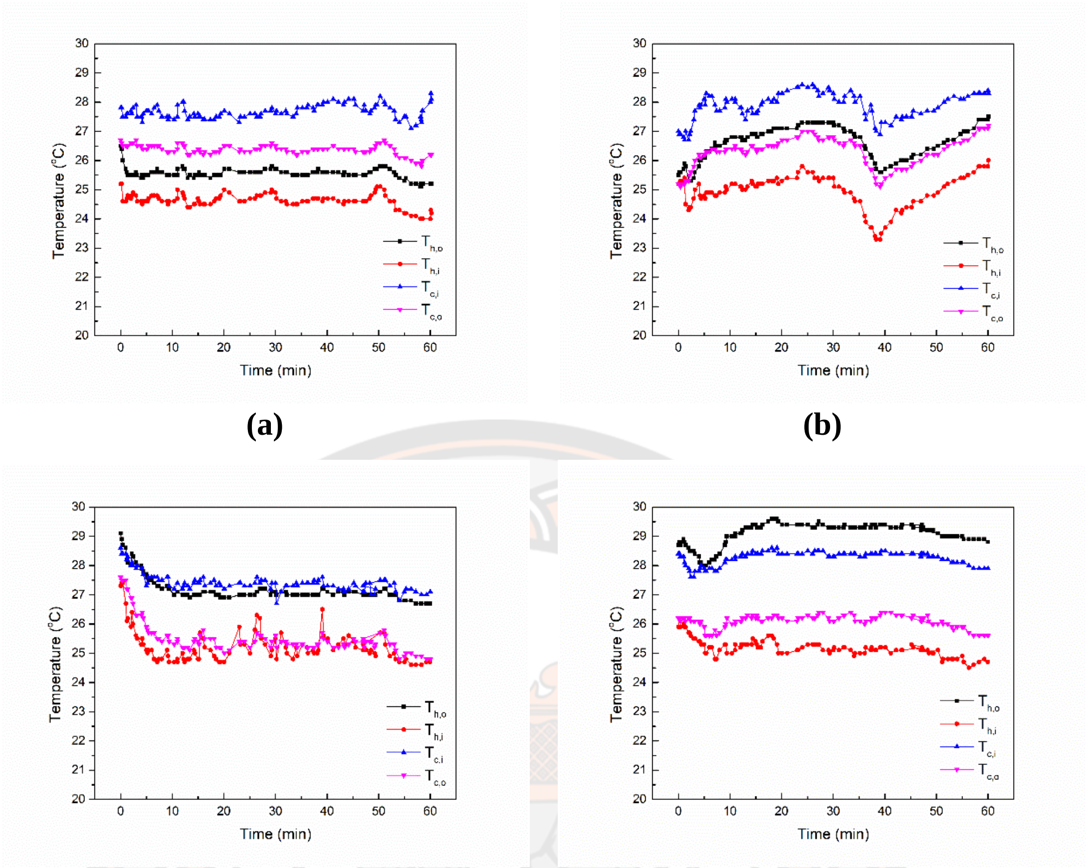

(a) (b)

(c) (d)

Figure 75 Inlet and outlet temperature of the TED (a) TE 3 V (b), TE 6 V (c) TE 9 V, and (d) TE 12 V versus time (cold side air flow rate: 0.04 kg s^{-1}, and ambient temperature: ~ 28 ^{o}C)

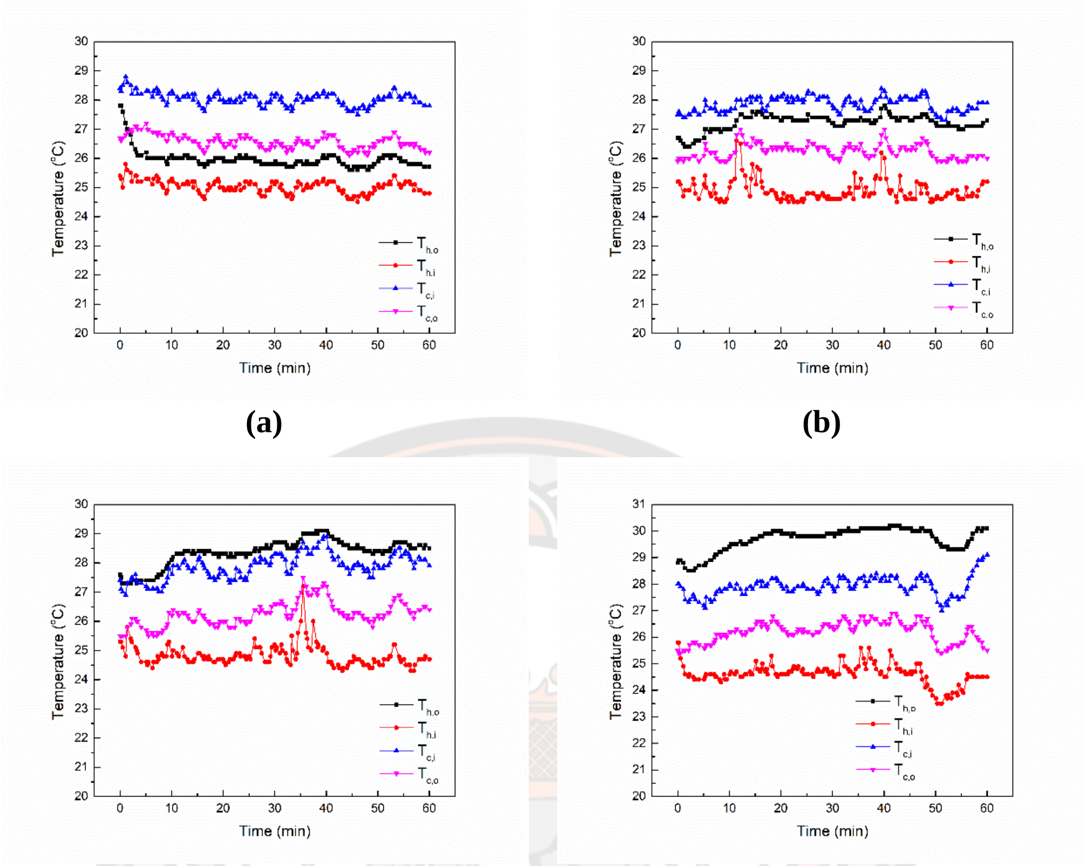

(a) **(b)**

(c) **(d)**

Figure 76 Inlet and outlet temperature of the TED (a) TE 3 V (b), TE 6 V (c) TE 9 V, and (d) TE 12 V versus time (cold side air flow rate: 0.06 kg s^{-1}, and ambient temperature: ~ 28 ^{o}C)

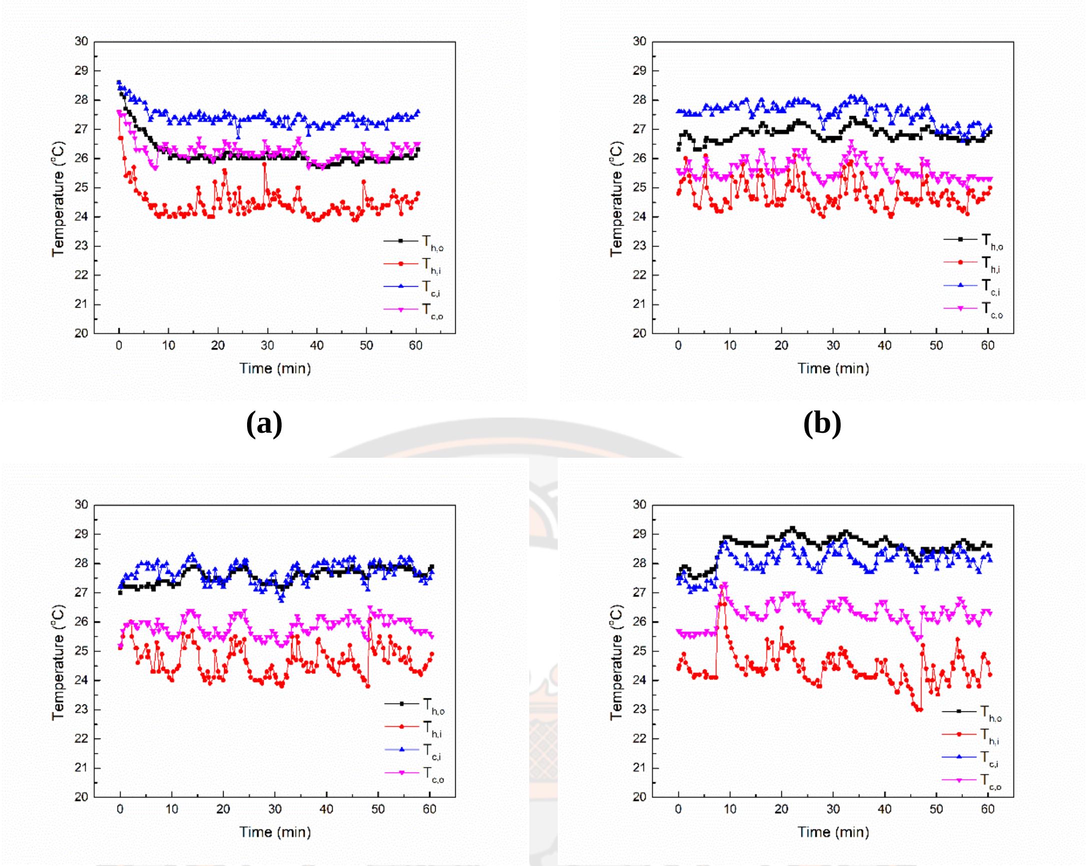

(a) **(b)**

(c) **(d)**

Figure 77 Inlet and outlet temperature of the TED (a) TE 3 V (b), TE 6 V (c) TE 9 V, and (d) TE 12 V versus time (cold side air flow rate: 0.08 kg s^{-1}, and ambient temperature: ~ 28 ^{o}C)

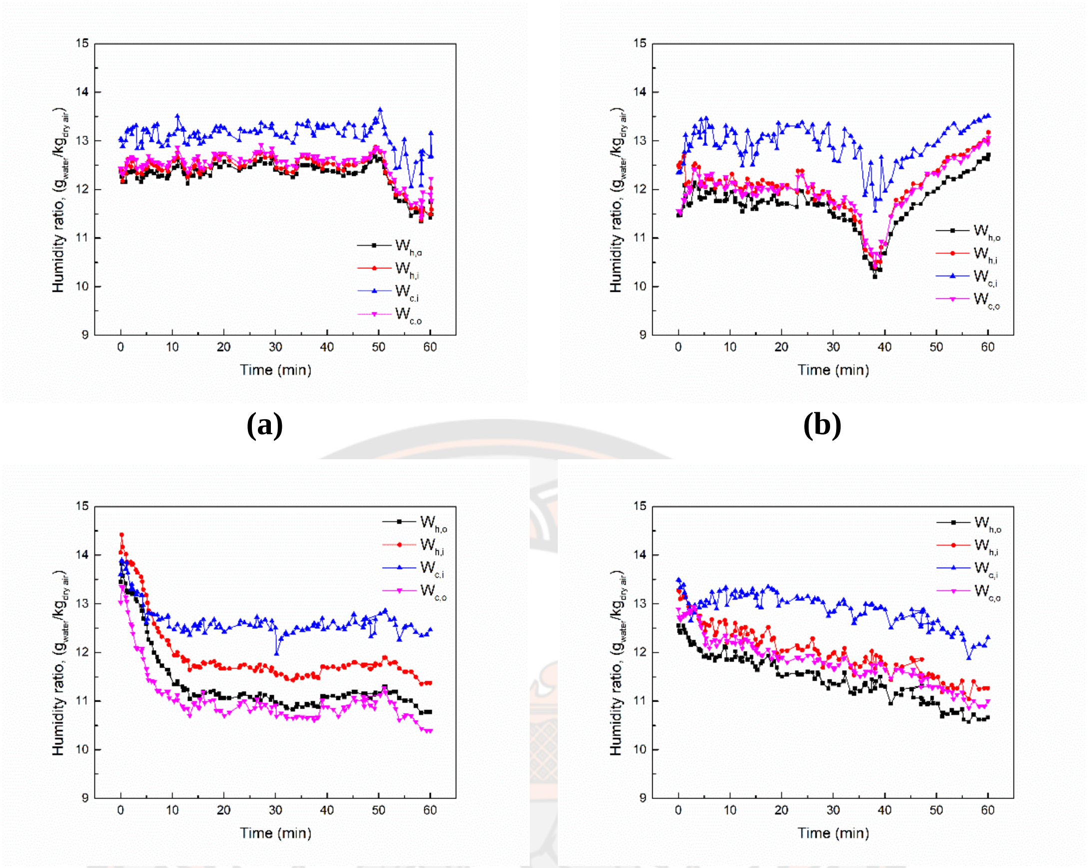

(a) **(b)**

(c) **(d)**

Figure 78 Humidity ratio of the TED (a) TE 3 V (b), TE 6 V (c) TE 9 V, and (d) TE 12 V versus time (cold side air flow rate: 0.04 kg s^{-1}, and ambient temperature: ~ 28 ^{o}C)

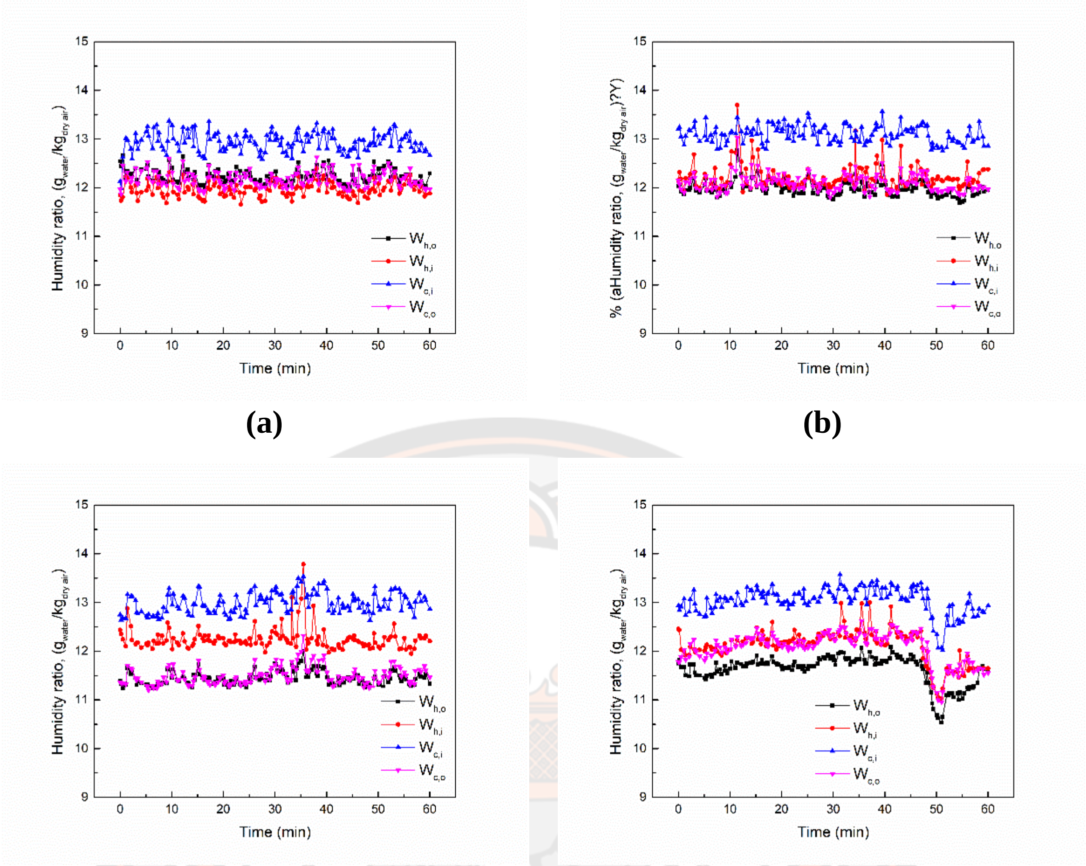

(a) (b)

(c) (d)

Figure 79 Humidity ratio of the TED (a) TE 3 V (b), TE 6 V (c) TE 9 V, and (d) TE 12 V versus time (cold side air flow rate: 0.06 kg s^{-1}, and ambient temperature: ~ 28 ^oC)

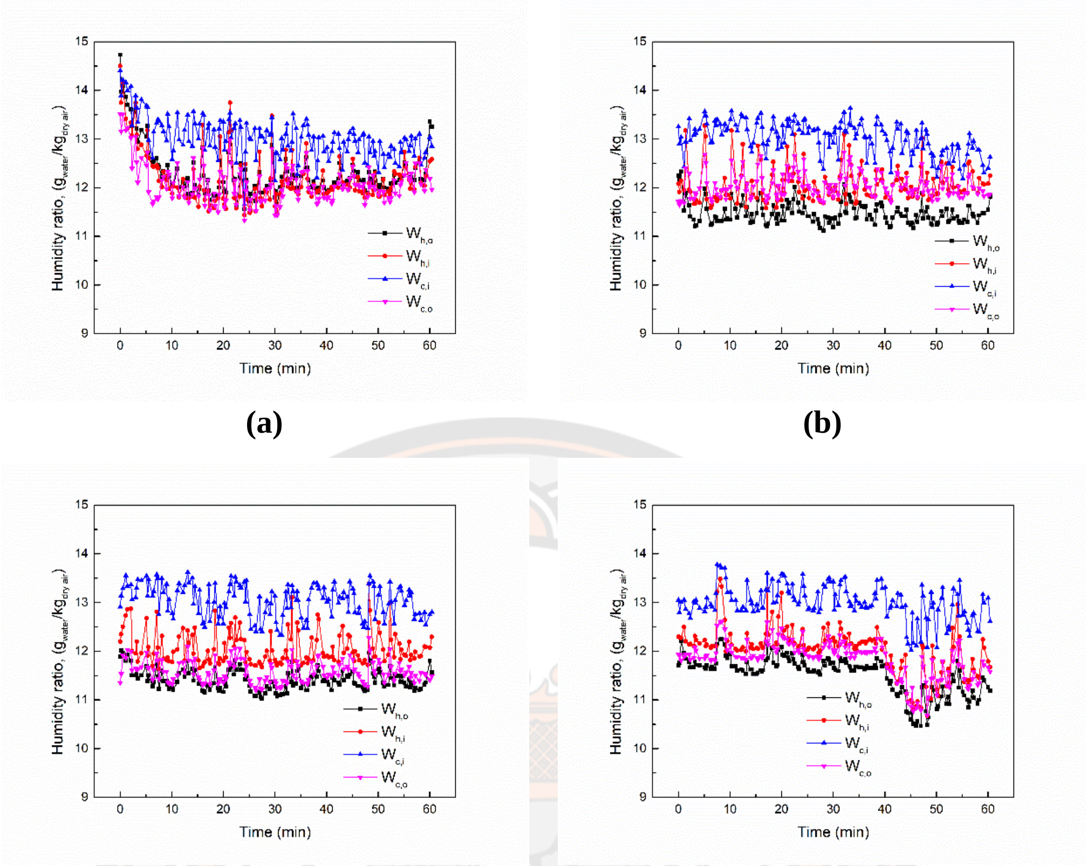

(a) (b)

(c) (d)

Figure 80 Humidity ratio of the TED (a) TE 3 V (b), TE 6 V (c) TE 9 V, and (d) TE 12 V versus time (cold side air flow rate: 0.08 kg s^{-1}, and ambient temperature: ~ 28 °C)

Figure 81 and Table 19 compares the dehumidifying processes under different electrical voltages of the TEMs. It can be seen that the outlet air humidity ratio depends strongly on the electrical voltage of the TEMs. In this experiment, when the electrical voltage was 3, 6, 9, and 12 V, the outlet air temperature decreased from 28.25 to 25.55 °C of cold side air flow rate 0.04 kg s^{-1}, 26.24 °C of cold side air flow rate 0.06 kg s^{-1}, and 25.84 °C of cold side air flow rate 0.08 kg s^{-1} at 9 V. Meanwhile, when the electrical voltage increased, the outlet air temperature of TED also increased slightly. At 9 V, the minimum outlet air temperature of TED was 25.55 °C. The outlet air humidity ratio for TED was 11.13, 11.49, and 11.59 g kg^{-1}, for cold side air flow rate 0.04, 0.06, and 0.08 kg s^{-1}. In contrast, for an electrical voltage of 12 V, the outlet air humidity ratio showed an increasing tendency. The outlet air humidity ratio was 11.87, 12.08, and 11.84 g kg^{-1} for cold side air flow rate 0.04, 0.06, and 0.08 kg s^{-1}, respectively. As a result, the outlet air temperature tends to be the same as the humidity ratio.

This result is explicable by the material properties of TEMs. The heat absorbed from the ambient by the TEMs comes from two sources: One is due to the Peltier effect, which is proportional to the module's current. Another source of energy comes from the Joule effect, which is proportional to the square of the current passing through the module. When the input electrical voltage is too low, the Peltier effect is ineffective, resulting in a slow rate of dehumidification. On the other hand, when the input electrical voltage is excessive, the Joule effect takes over, imposing a large heat load on the heat-cold heat sinks. Once the heat can't be dissipated into the air, it moves to the cold side of the fin heat sink through heat conduction. This weakens the condensing heat transfer on the fin heat sink.

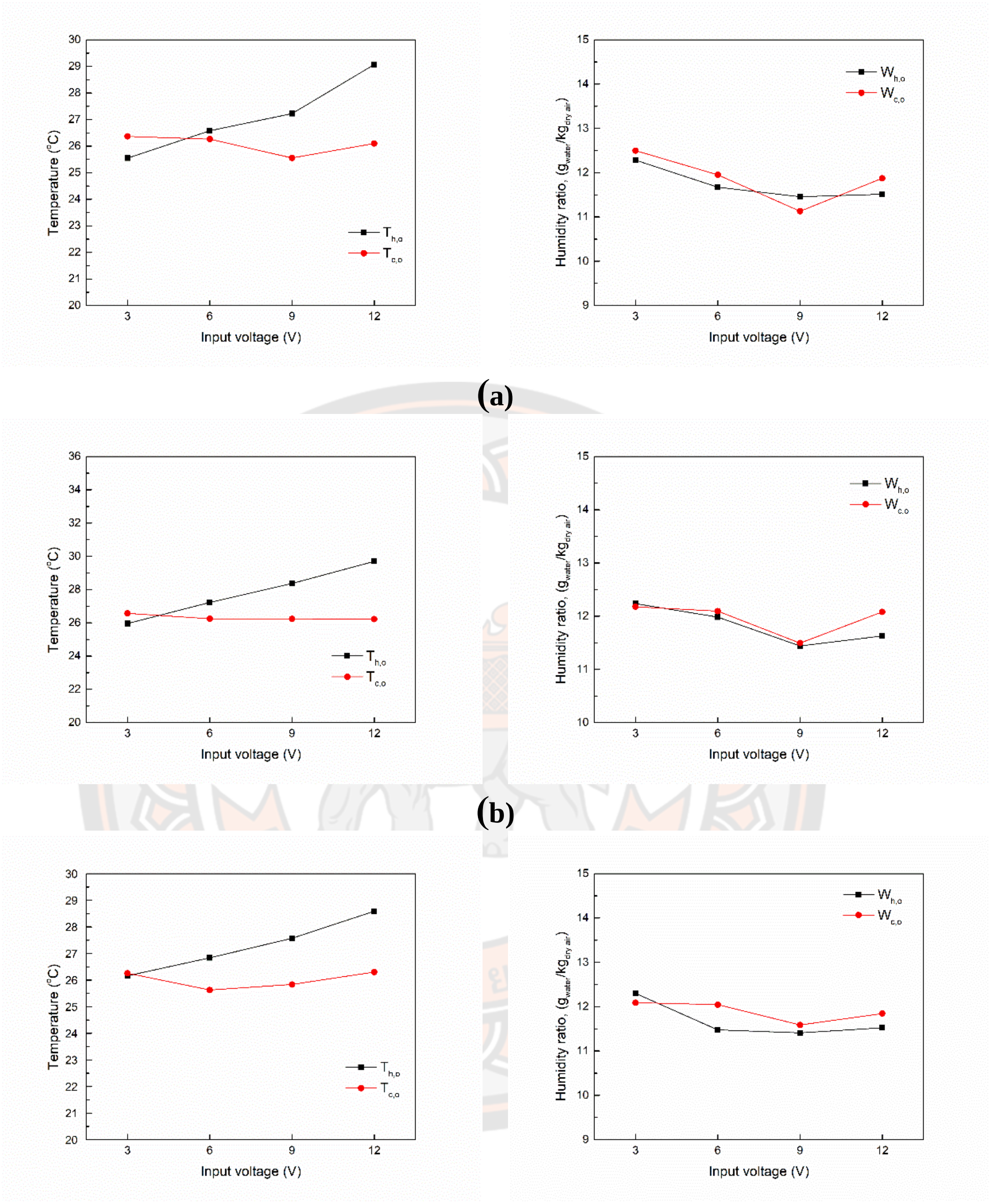

(a)

(b)

(c)

Figure 81 shows the effect of electrical voltage supply of TED (a) for cold side air flow rate (a) 0.04, (b) 0.06, and (c) 0.08 kg s^{-1}

Table 19 The values of the temperature (T), humidity ratio (W), and enthalpy (h) of the hot air outlet and cold air outlet of the TED

Cold side air flow rate (kg s^{-1})	Input voltage (V)	$T_{h,o}$ (ºC)	$W_{h,o}$ (g kg^{-1})	$h_{h,o}$ (kJ kg^{-1})	$T_{h,i}$ (ºC)	$W_{h,i}$ (g kg^{-1})	$h_{h,i}$ (kJ kg^{-1})	$T_{c,i}$ (ºC)	$W_{c,i}$ (g kg^{-1})	$h_{c,i}$ (kJ kg^{-1})	$T_{c,o}$ (ºC)	$W_{c,o}$ (g kg^{-1})	$h_{c,o}$ (kJ kg^{-1})
0.04	3	25.55	12.28	57.11	24.62	12.40	56.45	27.67	13.09	63.15	26.36	12.50	59.64
	6	26.58	11.67	56.61	24.95	12.02	55.30	27.85	12.91	61.07	26.26	11.95	57.00
	9	27.22	11.46	53.95	25.25	12.06	55.22	27.44	12.67	60.05	25.55	11.13	54.18
	12	29.07	11.52	57.89	25.18	12.07	54.66	28.25	12.91	61.48	26.10	11.87	58.69
0.06	3	25.96	12.23	56.13	25.03	11.97	55.76	28.03	12.93	62.60	26.57	12.18	58.40
	6	27.23	11.98	58.58	24.88	12.21	56.23	27.85	13.10	61.56	26.25	12.09	57.34
	9	28.36	11.44	59.91	24.83	12.25	56.27	27.86	12.98	60.78	26.24	11.49	56.70
	12	29.70	11.63	61.00	24.61	12.10	55.68	27.90	13.04	59.69	26.22	12.08	55.63
0.08	3	26.16	12.30	55.23	24.50	12.20	53.26	27.39	13.03	60.40	26.25	12.09	55.81
	6	26.84	11.48	56.38	24.78	12.07	54.49	27.57	13.02	59.55	25.63	12.05	54.16
	9	27.57	11.41	56.97	24.68	12.07	54.39	27.70	13.04	58.96	25.84	11.59	54.35
	12	28.59	11.52	57.28	24.47	12.03	53.57	28.11	13.01	58.67	26.30	11.84	54.47

According to **Figure 82** and **Table 20**, the cooling capacity (Q_c) increases with increasing electrical voltage and ranges between 17.82 and 100.78 W for an electrical voltage of 3 to 12 V at 0.06 kg s^{-1}. The Q_c increased as the electrical voltage increased and reached its maximum value of 100.78 W at the electrical voltage of 12 V. However, the COP decreased as the electrical voltage increased from 1.18 to 0.79. The difference in the COP between electrical voltages of 3 and 12 V is 67.18%, while the cooling capacity increased from 3 to 12 V or about 17.68%. The TED system's high COP usually corresponds to low Q_c, and high Q_c occurs with low COP. Therefore, the TED system optimization process is basically to find the best balance point for both.

Figure 82 depicts the COP ratio versus the electrical voltage. The COP ratio increases as the electrical voltage increases, implying that the TEC system's COP approaches the Carnot cooling cycle. When the electrical voltage was increased, the temperature on the cold side decreased, and the temperature difference between the hot and cold sides increased. As a result, the Carnot cooling cycle's coefficient of performance is reduced.

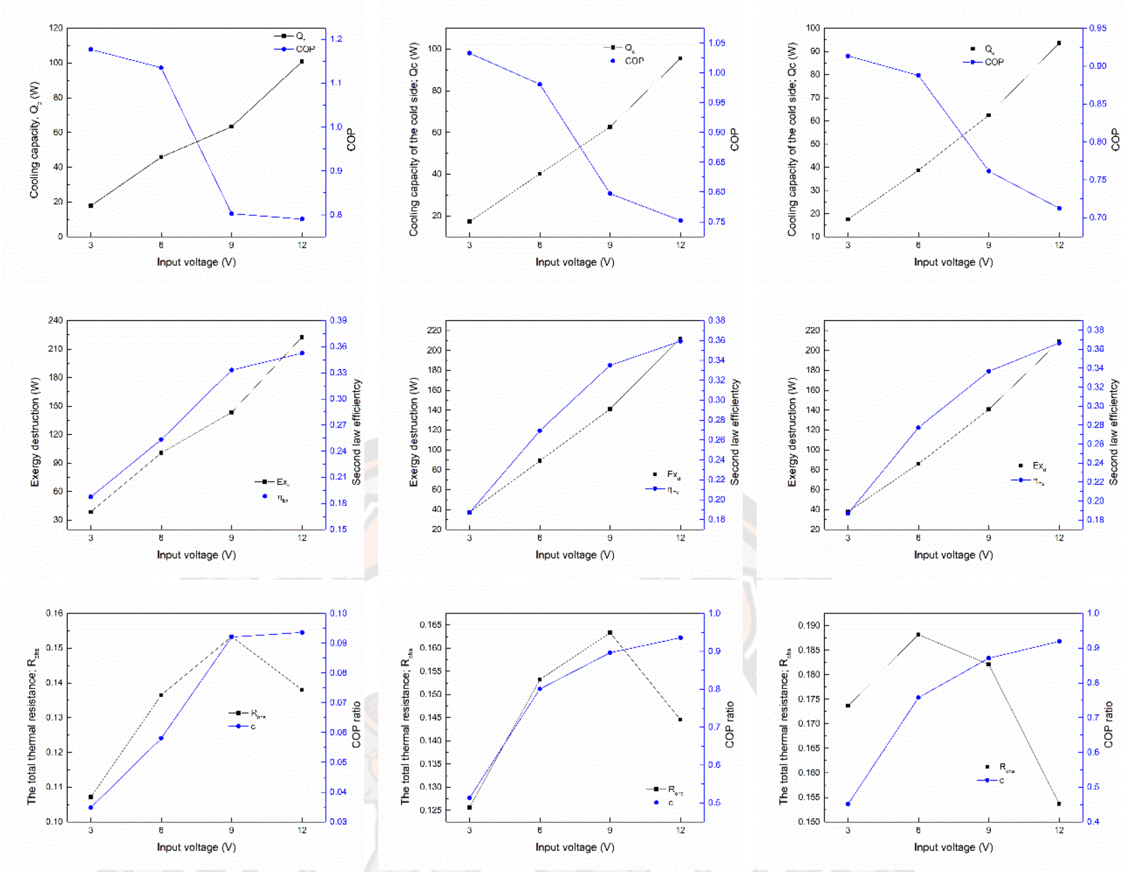

(a) (b) (c)

Figure 82 Shows the effect of electrical voltage supply of TED (a) cold side air flow rate: 0.04, (b) 0.06, and (c) 0.08 kg s^{-1}

Table 20 Performance of a TED under different cold side air flow rate

Cold side air flow rate (kg s^{-1})	Input voltage to TE (V)	Cooling capacity of the cold side (W)	COP	Ex_d	ηx_d	R_{ohs}	c
0.04	3	17.817	1.177	38.592	0.187	0.107	0.035
	6	45.865	1.135	100.665	0.253	0.136	0.058
	9	63.310	0.803	143.420	0.333	0.153	0.921
	12	100.784	0.790	222.728	0.353	0.138	0.964
0.06	3	17.317	1.033	37.403	0.187	0.126	0.513
	6	40.172	0.981	88.955	0.269	0.153	0.801
	9	62.748	0.797	141.216	0.335	0.163	0.896
	12	95.552	0.752	211.954	0.359	0.145	0.936
0.08	3	17.579	0.914	37.797	0.187	0.174	0.451
	6	38.658	0.888	85.949	0.277	0.188	0.757
	9	62.460	0.762	140.799	0.33663	0.18211	0.871
	12	93.588	0.713	208.885	0.36634	0.15369	0.920

Figure 83 and **Table 21** shows the moisture removal capacity 0.024, 0.038, 0.061, and 0.041 for cold side air flow rate 0.04 kg s^{-1}, 0.045, 0.060, 0.089, and 0.057 for cold side air flow rate 0.06 kg s^{-1}, and 0.074, 0.078, 0.115, and 0.093 for cold side air flow rate 0.08 kg s^{-1}. The highest moisture removal capacity (MRC) is 0.115 at voltages to thermoelectric module 12 V for cold side air flow rate 0.08 kg s^{-1}. The highest dehumidification effectiveness (E_{deh}) of cold side air flow rate 0.04, 0.06, and 0.08 kg s^{-1} was 0.122, 0.115, and 0.111 at voltages to thermoelectric module 9 V.

Table 21 Moisture removal capacity in the process (MRC) of TED under different cold side air flow rate and electrical voltage to TE

Cold side air flow rate (kg s^{-1})	**Input voltage to TE (V)**	**Moisture Removal Capacity (MRC)**	**Dehumidification effectiveness (E_{deh})**
0.04	3	0.024	0.046
	6	0.038	0.074
	9	0.061	0.122
	12	0.041	0.080
0.06	3	0.045	0.058
	6	0.060	0.076
	9	0.089	0.115
	12	0.057	0.074
0.08	3	0.074	0.072
	6	0.078	0.075
	9	0.115	0.111
	12	0.093	0.090

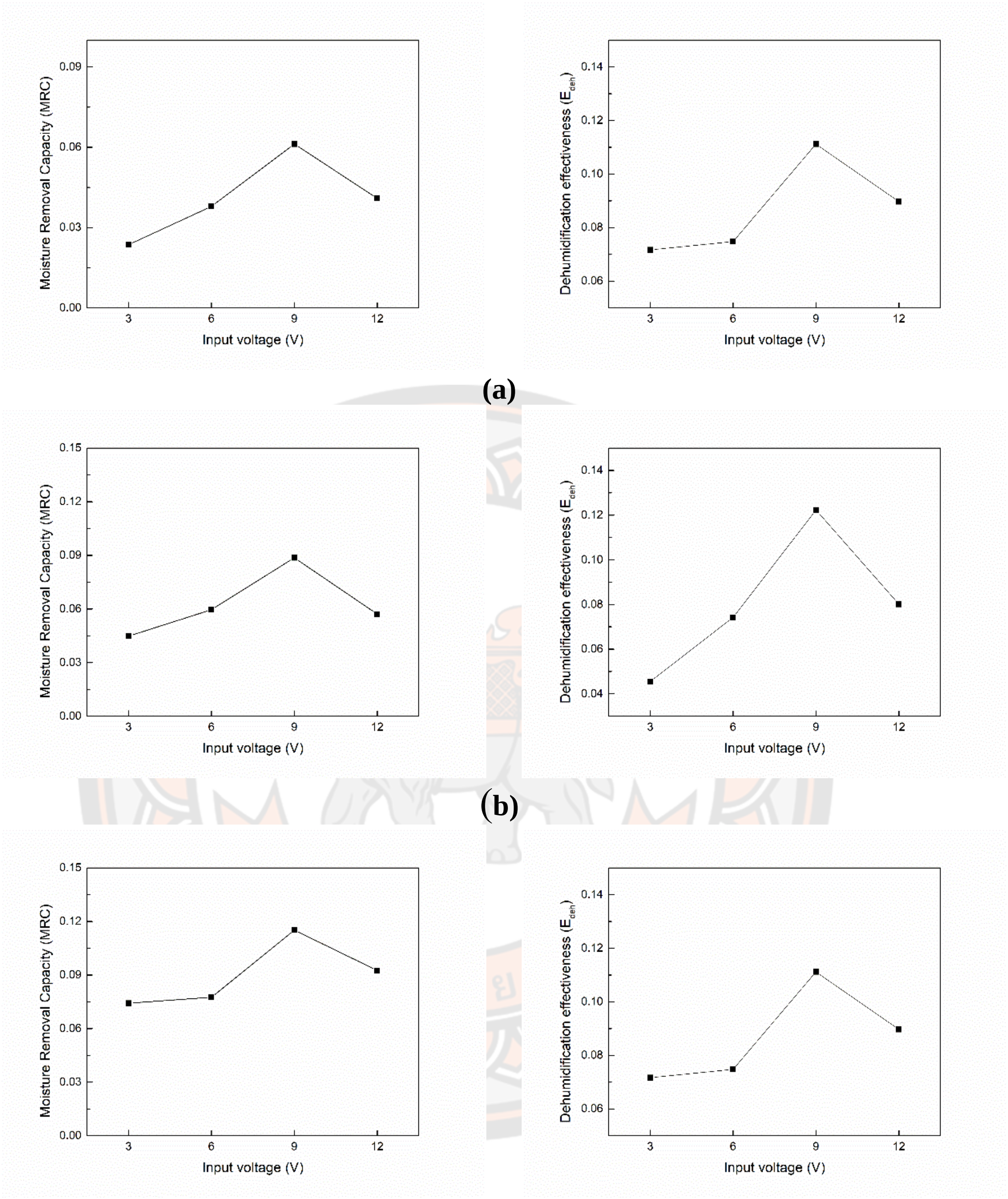

(a)

(b)

(c)

Figure 83 Shows the effect of electrical voltage supply of moisture removal capacity on TED (a) cold side air flow rate: 0.04, (b) 0.06, and (c) 0.08 kg s^{-1}

3. Effect of cold air flow rate

Figure 84 depicts the cold air flow rate through the heat sink on the cold sides of the TEMs. 3 different cold air flow rates (0.04, 0.06, and 0.08 kg s^{-1}) were used in the tests. As the air flow rate increased, the cold side temperatures of the TEMs increased slightly. Additionally, the Q_c was decreased. This was due to the fact that the COP decreased with increasing air flow rate, as shown in **Figure 84**. Consequently, this study does not want to use the highest air mass flow rate. This is because it did not improve heat transfer and it used more electricity to run the fan.

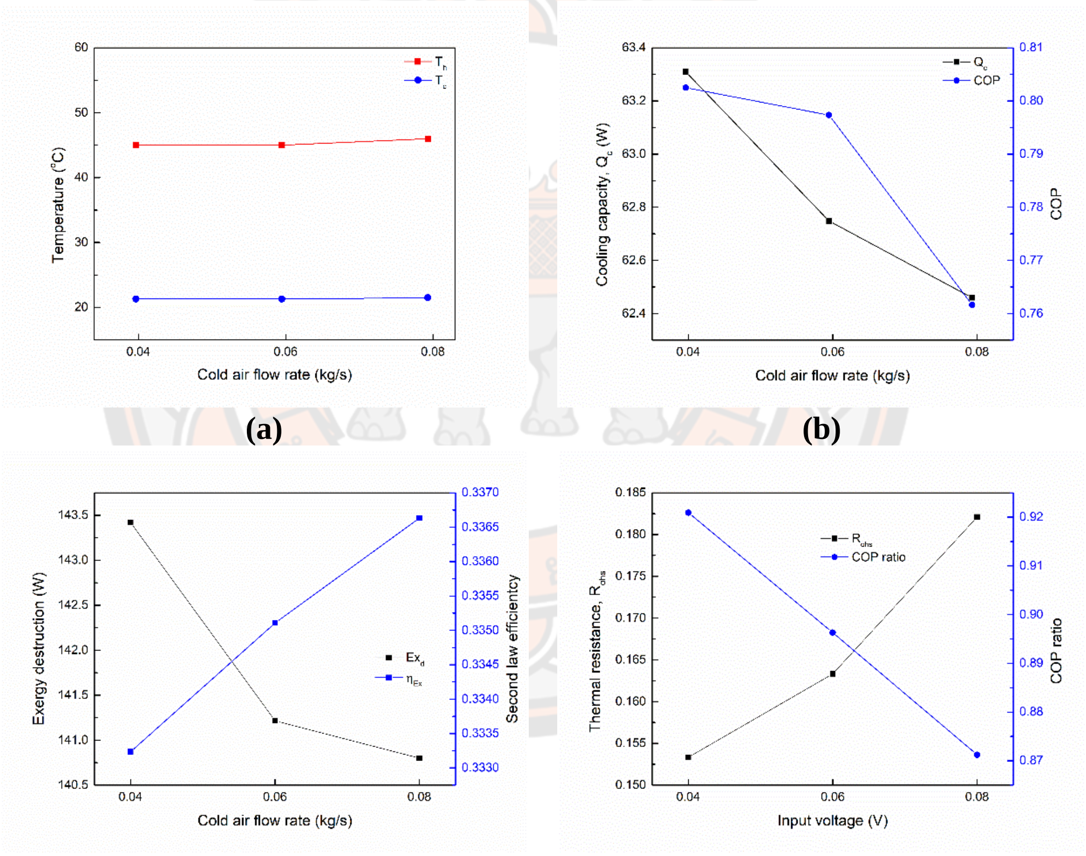

(a) **(b)**

(c) **(d)**

Figure 84 Effect of cold side air flow rate on the cold-side, hot-side temperatures (a), cooling capacity and COP (b), exergy destruction and second law efficiency (c), and R_{ohs} and c (d) of TED system (electric voltage 9 V)

Table 22 Performance of a TED under different cold side air flow rate

Cold side air flow rate (kg s^{-1})	T_h	T_c	Q_c	COP	Ex_d	ηx_d	R_{ohs}	c
0.04	45	21.3	63.31	0.80	143.42	0.333	0.153	0.921
0.06	45	21.3	62.75	0.80	141.22	0.335	0.163	0.896
0.08	46	21.5	62.46	0.76	140.80	0.337	0.182	0.871

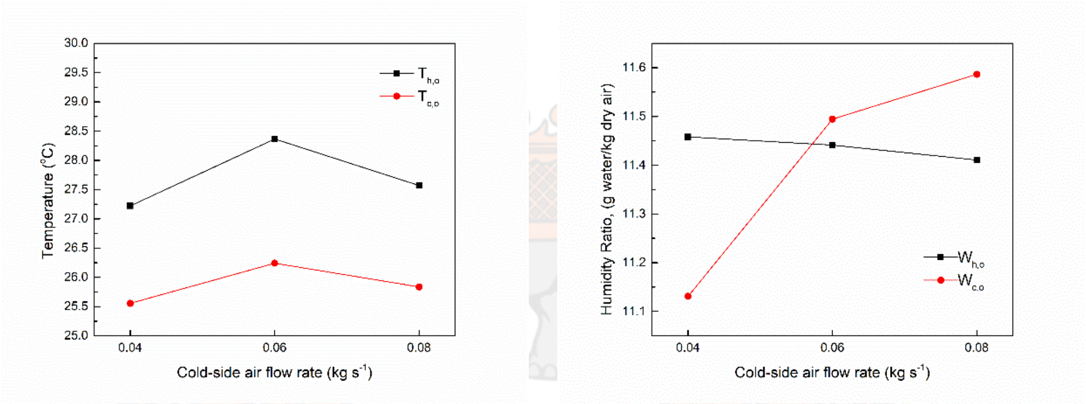

(a) **(b)**

Figure 85 Effect of cold side air flow rate on the cold-air, and hot-air temperatures (a) and humidity ratio of the hot air outlet and cold air outlet of the TED (electric voltage 9 V)

Table 23 The cold-air, and hot-air temperatures (a) and humidity ratio of the hot air outlet and cold air outlet of the TED (electric voltage 9 V)

Cold side air flow rate ($kg\ s^{-1}$)	W_{ho}	W_{co}	T_{ho}	T_{co}
0.04	11.458	11.131	27.221	25.554
0.06	11.441	11.494	28.365	26.242
0.08	11.411	11.586	27.570	25.834

Thermoelectric dehumidifier (TED) with composite desiccant coated heat sink

1. Effect of voltage supply

The TED with a composite desiccant (TED-CD) was built with a composite desiccant thickness of 1.5 mm. For a 60 minute test period, in this experiment, the measured data was divided into 4 conditions test exclude the effect of voltages to thermoelectric module. The measured parameters in this experiment include temperature, humidity ratio and flow rate of air inlet and air outlet. The effective of the system represented by the Thermal coefficient of performance (COP_{th}), Moisture removal capacity (MRC), Moisture removal regeneration ratio (MRR), Dehumidification effectiveness (E_{deh}), and regeneration effectiveness (E_{reg}). The results are shown in **Table 24** below.

Figures 86-89 show the relation between air humidity ratio and air temperature on various cycle times of hot air flow rate 0.0793 kg s^{-1} at cold air flow rate 0.03965 kg s^{-1}. For this experiment, the temperature of the cold air supplied was set at nearly 28 ^{o}C for dehumidification process and hot air supplied was nearly 25 ^{o}C for regeneration process. At the regeneration time, the humidity ratio of air was higher than air inlet humidity ratio because the moisture desorbed from silica gel, which coated on the heat sink and released to the air. When changed mode for dehumidification time the humidity ratio of the air outlet dropped to lower than air humidity inlet and slightly increased to equilibrium condition with nearly to air humidity inlet.

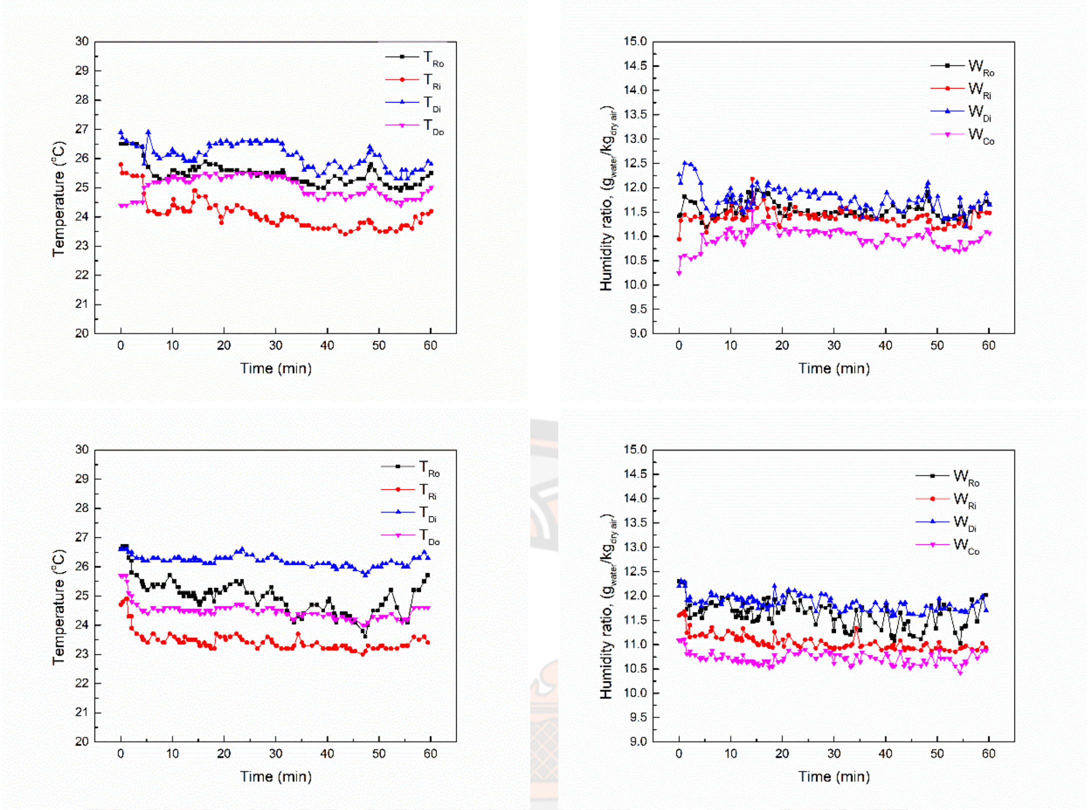

(a) **(b)**

Figure 86 Inlet and outlet temperature (a), and humidity ratio (b) of the TED-CD versus time (cold side air flow rate: 0.04 kg s^{-1}, electrical voltage: 3 V, and ambient temperature: ~ 28 ^{o}C)

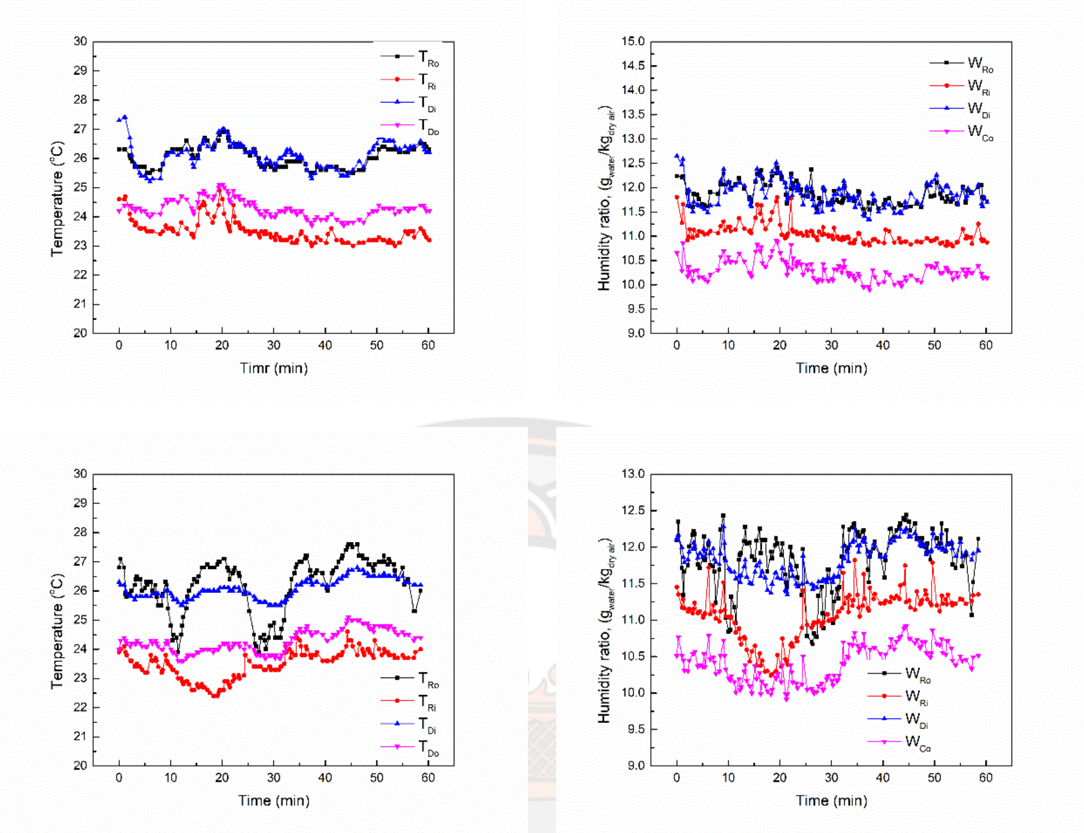

(a) **(b)**

Figure 87 Inlet and outlet temperature (a), and humidity ratio (b) of the TED-CD versus time (cold side air flow rate: 0.04 kg s^{-1}, electrical voltage: 6 V, and ambient temperature: ~ 28 ^{o}C)

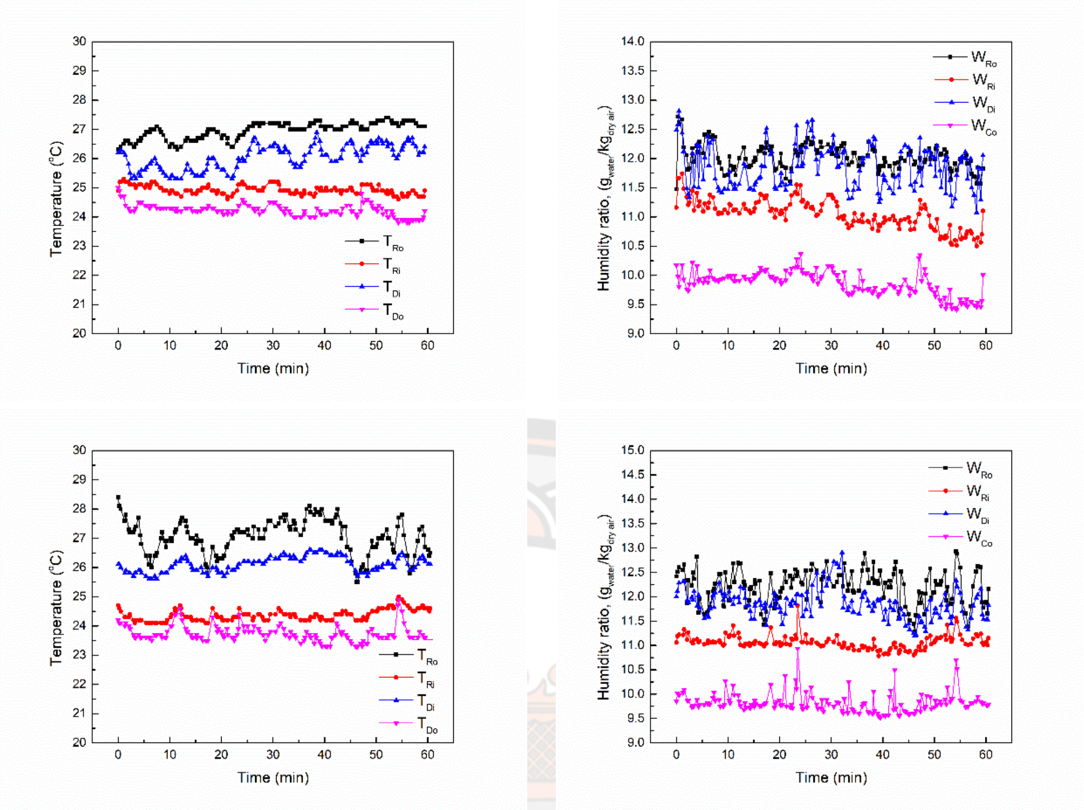

(a) **(b)**

Figure 88 Inlet and outlet temperature (a), and humidity ratio (b) of the TED-CD versus time (cold side air flow rate: 0.04 kg s^{-1}, electrical voltage: 9 V, and ambient temperature: ~ 28 ^{o}C)

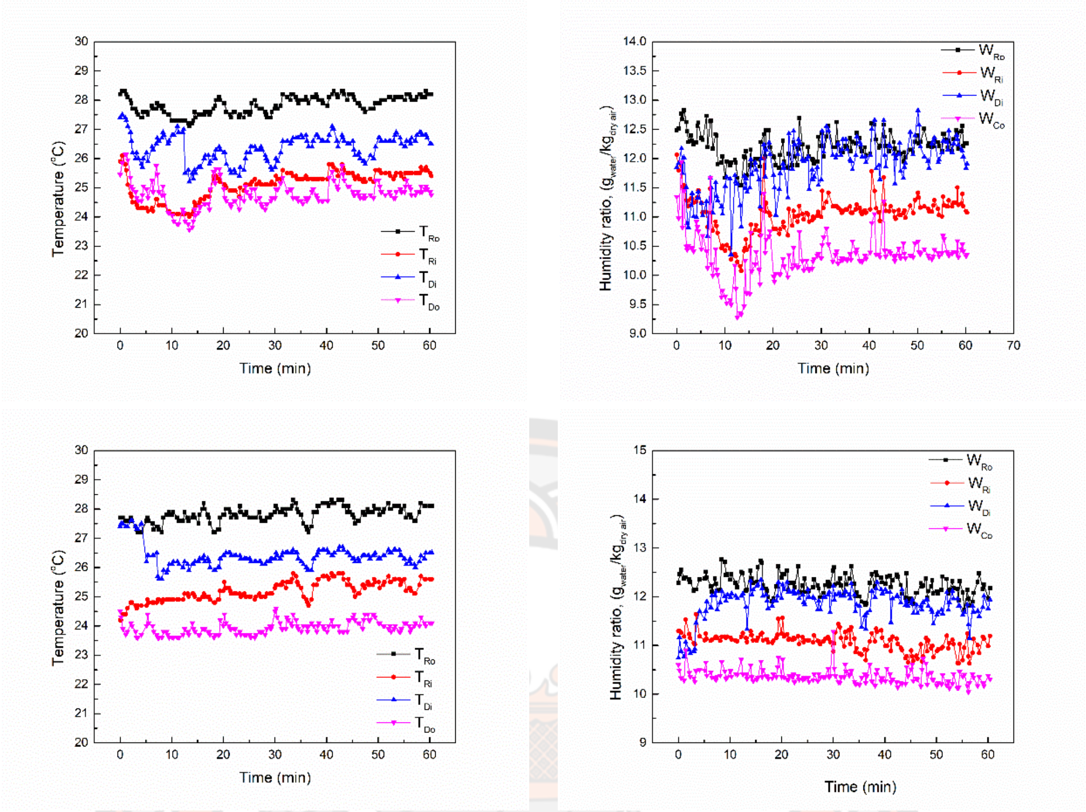

(a) **(b)**

Figure 89 Inlet and outlet temperature (a), and humidity ratio (b) of the TED-CD versus time (cold side air flow rate: 0.04 kg s^{-1}, electrical voltage: 12 V, and ambient temperature: ~ 28 °C)

Figures 90-94 compares the dehumidifying processes under different electrical voltages of the TEMs. It can be seen that the outlet air humidity ratio depends strongly on the electrical voltage of the TEMs. In this experiment, when the electrical voltage was 3, 6, 9, and 12 V, **Figures 90-94** are illustrate all of parameters which represent the performance of the system. **Figure 90** shows the outlet air temperature from 28.0 to 25.06, 24.30, 24.23, and 24.78 ^{o}C (dehumidification system-1) and 24.49, 24.27, 23.73, and 23.95 ^{o}C (dehumidification system-2) for input voltages 3, 6, 9, and 12 V. **Figure 91** shows the moisture adsorption from 11.85 to 10.98, 10.31, 9.86, and 10.34 g kg^{-1} (dehumidification system-1) and 10.72, 10.41, 9.83, and 10.37 g kg^{-1} (dehumidification system-2). And **Figure 91** shows the moisture desorption of the system those increased from 11.06 to 11.64, 11.87, 12.03, and 12.21 g kg^{-1} (regeneration system-1) and 11.62, 11.84, 12.03, and 12.25 g kg^{-1} (regeneration system-2).

The energy that will affect negatively on the air conditioner is made up of both exposed and latent heat. The difference between the input and output enthalpy of the dehumidification unit demonstrates this. The less load transmitted to the air conditioning system, the lower the enthalpy in the air can be reduced. According to the results of the experiments, when the power is increased at a potential difference of 9 V, we can reduce the enthalpy in the air as much as possible when compared to the enthalpy of the input air, as shown in **Figure 92**.

MRC of the system is highest at voltages to thermoelectric module 9 V. The values of parameter indices each of case are significantly different. MRC of the system is highest at voltages to thermoelectric module 9 V. **Figure 93** illustrates the effectiveness of dehumidification (E_{deh}) process are 0.07, 0.13, 0.17, and 0.13 (dehumidification system-1) and 0.10, 0.12, 0.17, and 0.12 (dehumidification system-1). The highest regeneration effectiveness (E_{reg}) is 0.09 at voltages to thermoelectric module 9 V for regeneration system-1 and 2. The COP of the system increases when increasing voltages to thermoelectric module from 0.97, 1.16, 2.33, and 1.25 (dehumidification-regeneration system-1) and 0.68, 1.52, 2.17, and 1.68 (dehumidification-regeneration system-2) because more moisture adsorbed and desorbed from the desiccant.

Lastly **Table 25**, the performance indices of system from each case seem to be not significantly different except voltages to thermoelectric module 3 V to 12 V and working phase of the dehumidification-regeneration system. The valves of performance average moisture adsorption, average moisture desorption, COP_{th}, MRC, MRR, E_{deh}, and E_{reg} are nearly same every working phase of the dehumidification-regeneration system in the same condition.

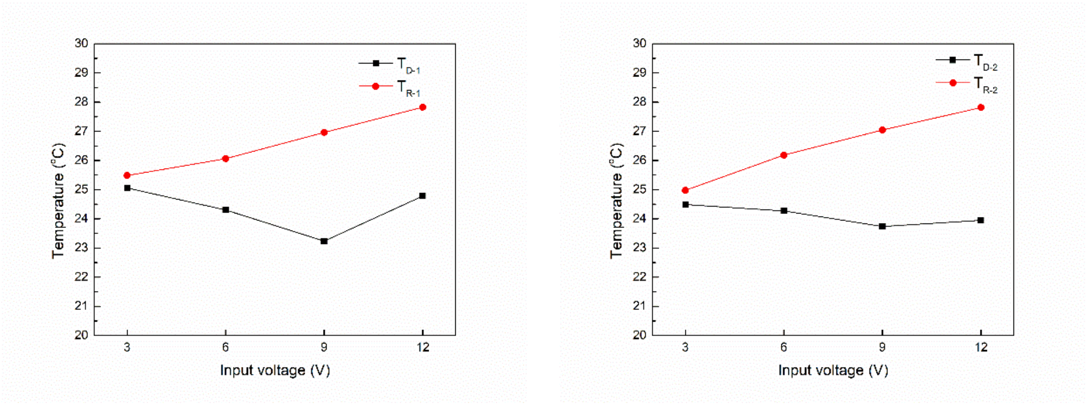

(a) **(b)**

Figure 90 Outlet temperature of dehumidification-regeneration system-1 (a), and dehumidification-regeneration system-2 (b) versus input voltage (cold side air flow rate: 0.04 kg s^{-1}, and ambient temperature: ~ 28 ^{o}C)

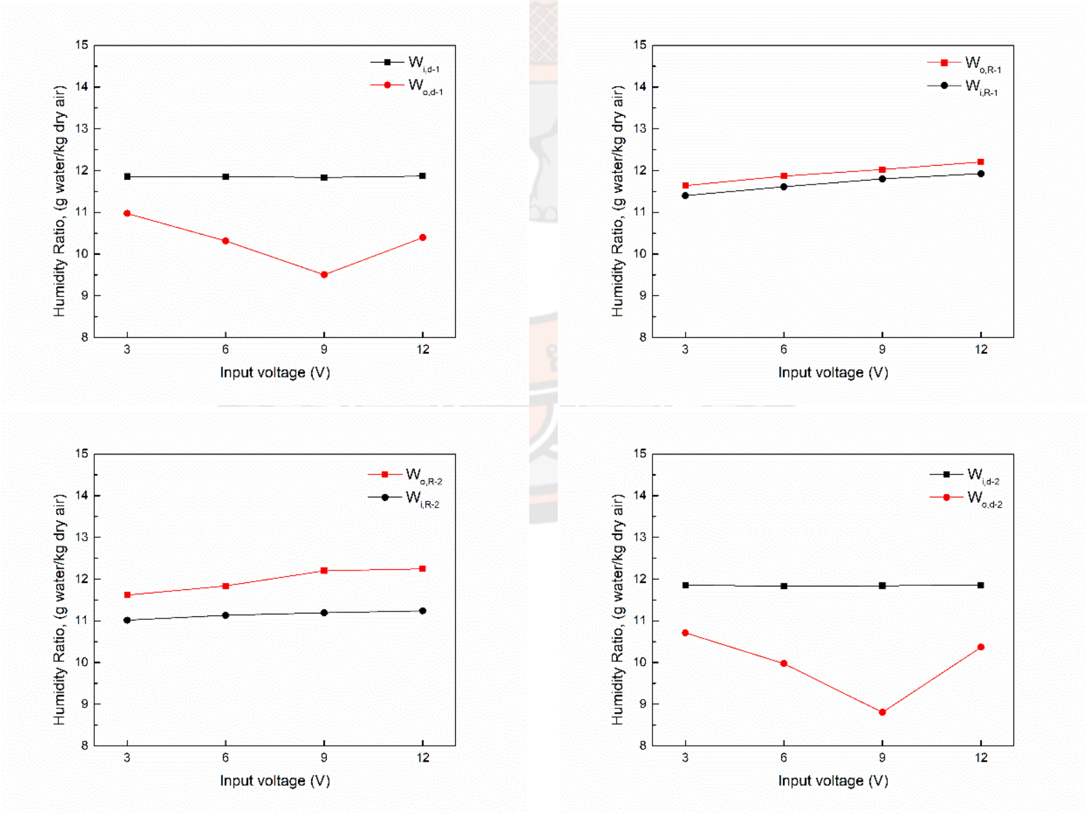

Figure 91 Humidity ratio of dehumidification-regeneration system-1 (a), and dehumidification-regeneration system-2 (b) versus input voltage (cold side air flow rate: 0.04 kg s^{-1}, and ambient temperature: ~ 28 ^{o}C)

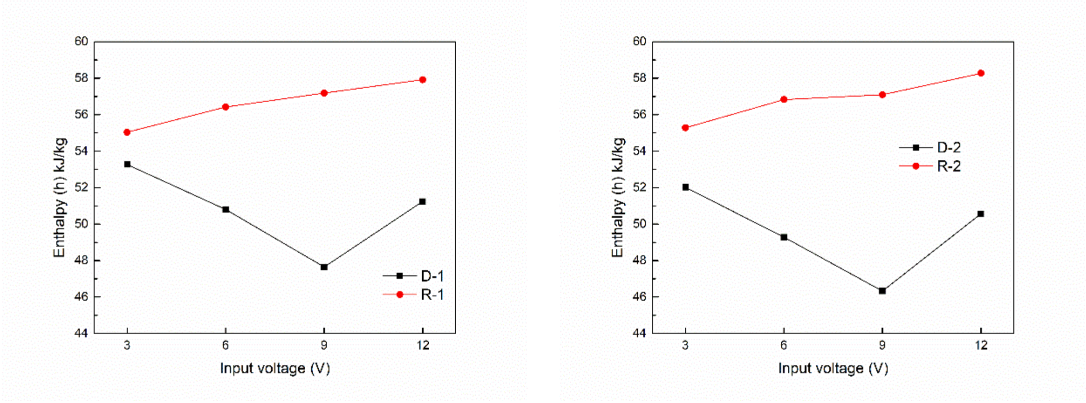

(a) (b)

Figure 92 Enthalpy of dehumidification-regeneration system-1 (a), and dehumidification-regeneration system-2 (b) (cold side air flow rate: 0.04 kg s^{-1}, and ambient temperature: ~ 28 ^{o}C)

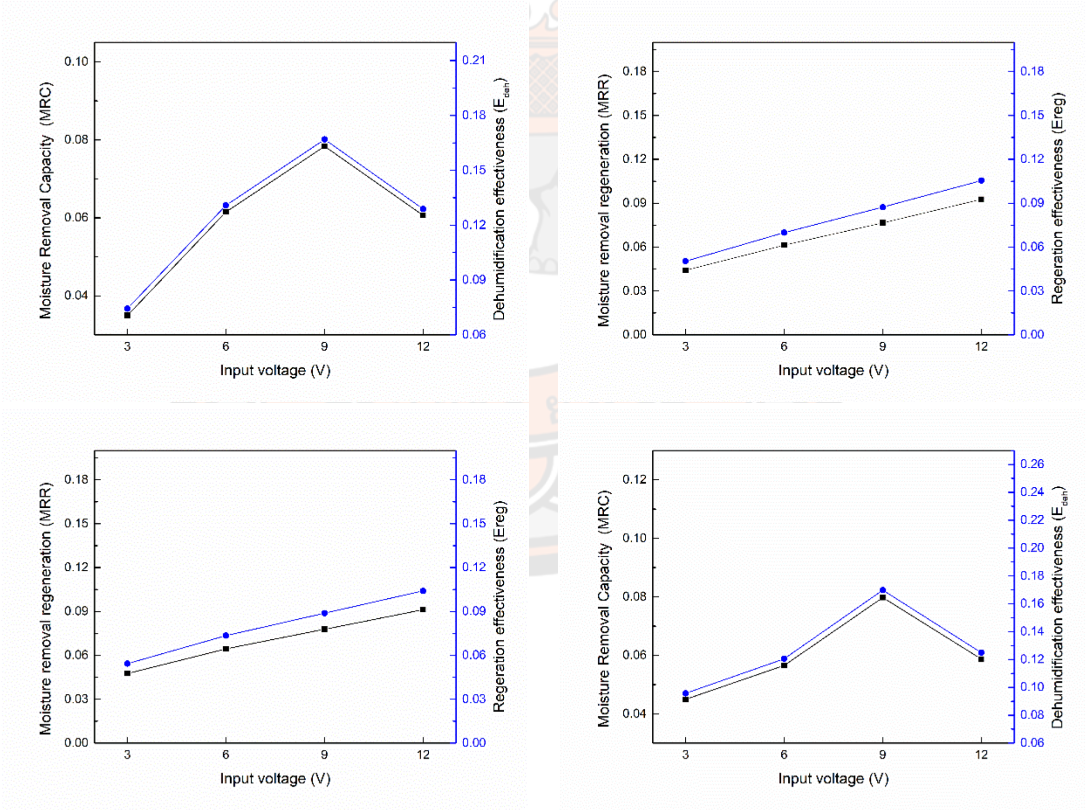

(a) (b)

Figure 93 MRR and E_{deh} (a), and MRC and E_{reg} (b) of the TED-CD versus input voltage (cold side air flow rate: 0.04 kg s^{-1}, and ambient temperature: ~ 28 ^{o}C

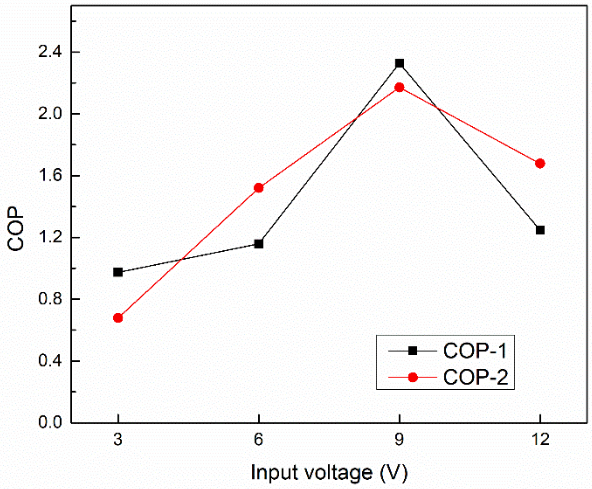

Figure 94 COP of the TED-CD versus input voltage (cold side air flow rate: 0.04 kg s^{-1}, and ambient temperature: ~ 28 ^{o}C)

Table 24 Performance of a TED with composite desiccant under different electrical voltage

Input voltage (V)	**Dehumidification system-1**								**Regeneration system-1**							**COP_{th}**
	T_{d-1i}	**h_{d-1i} (kJ kg^{-1})**	**W_{d-1i} (g kg^{-1})**	**T_{d-1o}**	**h_{d-1o} (kJ kg^{-1})**	**W_{d-1o} (g kg^{-1})**	**MRC**	**E_{deh}**	**T_{r-1o}**	**h_{r-1o} (kJ kg^{-1})**	**W_{r-1o} (g kg^{-1})**	**T_{r-1i}**	**h_{r-1i} (kJ kg^{-1})**	**W_{r-1i} (g kg^{-1})**	**MRR**	**E_{reg}**	
3	26.11	56.53	11.86	25.06	53.26	10.98	0.03	0.07	25.48	55.03	11.64	24.10	53.35	11.04	0.05	0.05	0.97
6	26.14	56.65	11.86	24.30	50.81	10.31	0.06	0.13	26.06	56.42	11.87	23.51	53.90	11.06	0.06	0.07	1.16
9	26.03	56.73	11.84	24.23	47.65	9.86	0.08	0.17	26.96	57.18	12.03	24.93	55.23	11.05	0.08	0.09	2.33
12	26.36	56.73	11.87	24.78	51.24	10.34	0.06	0.13	27.83	57.92	12.21	25.08	55.72	11.06	0.09	0.10	1.25
Input voltage (V)	**Dehumidification system-2**								**Regeneration system-2**							**COP_{th}**
	T_{d-2i}	**h_{d-2i} (kJ kg^{-1})**	**W_{d-2i} (g kg^{-1})**	**T_{d-1o}**	**h_{d-1o} (kJ kg^{-1})**	**W_{d-1o} (g kg^{-1})**	**MRC**	**E_{deh}**	**T_{r-2o}**	**h_{r-2o} (kJ kg^{-1})**	**W_{r-2o} (g kg^{-1})**	**T_{r-2i}**	**h_{r-2i} (kJ kg^{-1})**	**W_{r-2i} (g kg^{-1})**	**MRR**	**E_{reg}**	
3	26.20	55.28	11.85	24.49	52.01	10.72	0.04	0.10	24.98	55.28	11.62	23.46	52.87	11.06	0.04	0.05	0.68
6	26.05	56.83	11.83	24.27	49.28	10.41	0.06	0.12	26.18	56.83	11.84	23.50	54.35	11.06	0.06	0.07	1.52
9	26.09	57.10	11.84	23.73	46.33	9.83	0.08	0.17	27.05	57.10	12.03	24.36	54.62	11.06	0.08	0.09	2.17
12	26.34	57.27	11.85	23.95	50.57	10.37	0.06	0.12	27.81	58.27	12.25	25.19	55.97	11.08	0.09	0.11	1.68

2. Comparison of the TED with and without the composite desiccant-coated heat sink

To investigate the application of composite desiccants further, a TED with a composite desiccant (TED-CD) and without a composite desiccant (TED) heat sink was built with a composite desiccant thickness of 1.5 mm. For a 60-minute test period, **Figure 95(a)** and **95(b)** shows the inlet and outlet temperature and humidity ratio. The outlet humidity ratio decreased from 12.67 g kg^{-1} to 11.13 g kg^{-1} for the TED and 11.84 g kg^{-1} to 9.86 g kg^{-1} for the TED-CD, while the outlet temperature in the TED and TED-CD dropped by only about 0.5 to 2 ^{o}C.

Figure 96 and **Table 26** compares the dehumidifying processes under different electrical voltages of the TEMs. It can be seen that the outlet air humidity ratio depends strongly on the electrical voltage of the TEMs. In this experiment, when the electrical voltage was 3, 6, 9, and 12 V, the outlet air temperature decreased from 28 to 24.23 ^{o}C at 9 V of TED-CD. Meanwhile, when the electrical voltage increased, the outlet air temperature of TED also increased slightly. At 9 V, the minimum outlet air temperature of TED was 25.55 ^{o}C, as shown in **Figure 96(a)**. The outlet air humidity ratio (**Figure 96(b)**) for TED was 12.50, 11.95, 11.13, 11.87 g kg^{-1}, while it was 10.98, 10.31, 9.86, and 10.34g kg^{-1} for TED-CD. In contrast, for an electrical voltage of 12 V, the outlet air humidity ratio showed an increasing tendency. The outlet air humidity ratio was 11.87 g kg^{-1} for TED and 10.34 g kg^{-1} for TED-CD, respectively. As a result, the outlet air temperature tends to be the same as the humidity ratio.

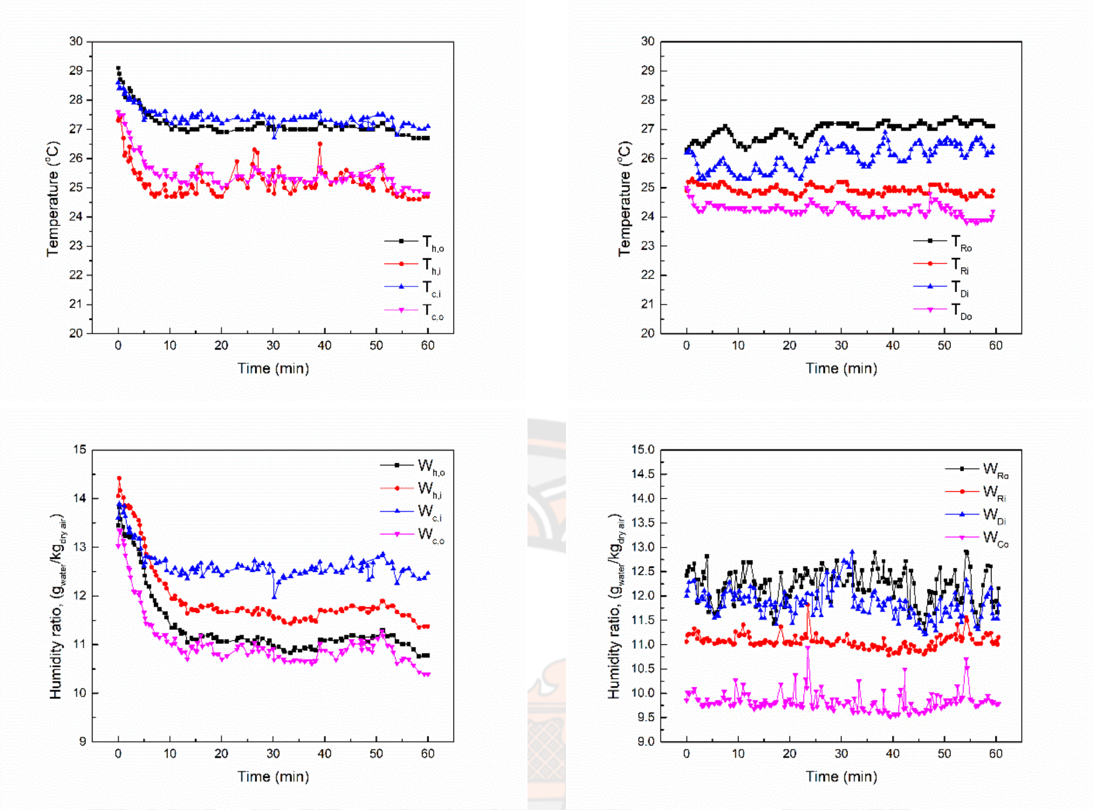

(a) (b)

Figure 95 Inlet and outlet temperature of the TED (a) and TED-CD (b), and humidity ratio of the TED (c) and TED-CD (d) versus time (cold side air flow rate: 0.04 kg s^{-1}, electrical voltage: 9 V, and ambient temperature~ 28 ^{o}C)

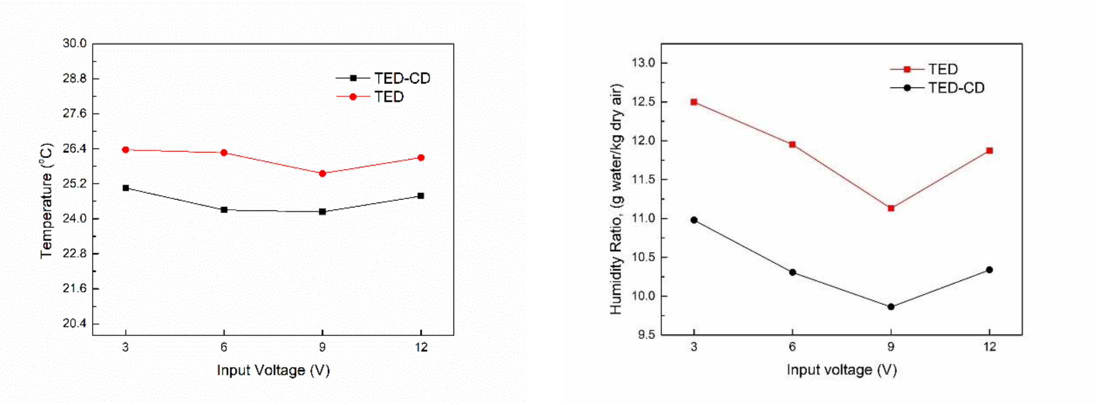

(a) **(b)**

Figure 96 The outlet air (a) temperature, and (b) humidity ratio of the TED and TED-CD versus input voltage (cold side air flow rate: 0.04 kg s^{-1} and ambient temperature: ~ 28 ^{o}C)

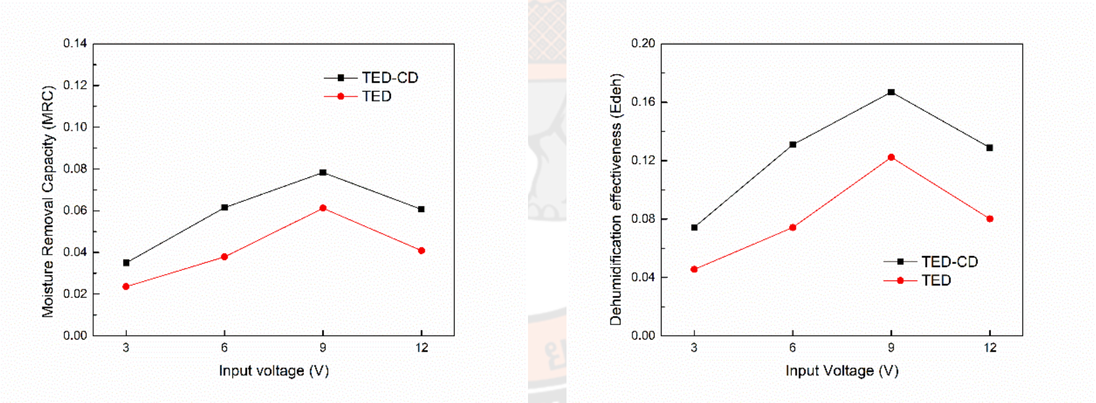

(a) **(b)**

Figure 97 MRC (a) and E_{deh} (b) of the TED and TED-CD versus input voltage (cold side air flow rate: 0.04 kg s^{-1} and ambient temperature: ~ 28 ^{o}C)

Table 25 Performance of a TED with and without composite desiccant under different electrical voltage

Input voltage (V)	TED-CD						TED					
	T (°C)	W_i (g kg^{-1})	W_o (g kg^{-1})	h_o (kJ kg^{-1})	MRC	E_{deh}	T (°C)	W_i (g kg^{-1})	W_o (g kg^{-1})	h_o (kJ kg^{-1})	MRC	E_{deh}
3	25.06	11.86	10.98	53.26	0.03	0.07	26.36	13.09	12.50	59.64	0.02	0.05
6	24.30	11.86	10.31	51.79	0.06	0.13	26.26	12.91	11.95	57.00	0.04	0.07
9	24.23	11.84	9.86	51.16	0.08	0.17	25.55	12.67	11.13	54.18	0.06	0.12
12	24.78	11.87	10.34	53.43	0.06	0.13	26.10	12.91	11.87	58.69	0.04	0.08

CHAPTER V

CONCLUSIONS AND RECOMMENDATIONS

In the overview of this research, the results can be summarized as follows.

5.1 Conclusions

A recyclable method for production of mesoporous silica nanostructure from bagasse ash of sugar cane industry

Mesoporous silica could be prepared using bagasse ash by the precipitation method. The mesoporous silica powder with nanoparticles, a spherical shape, and a narrow size distribution was used to determine the optimum preparation conditions. It was found that the desired mesoporous silica could be synthesized using 2.0 N NaOH and an aging time of 18 h under pH gelation 7. The yield of silica reached up to 91.73%. The specific surface area, pore volume, and pore size of the mesoporous silica are 525 m^{2} g^{-1}, 0.61 cm3 g^{-1}, and 15 nm, respectively. The obtained mesoporous silica particles were spherical-shaped nanoparticles with 50 nm to 100 nm in diameter. This study demonstrates that mesoporous silica produced from bagasse ash is an efficient adsorbent with a high adsorption capacity.

Development and characterization of composite desiccant-coated aluminum sheets (DCAS)

The maximum thermal conductivity of composite DCAS was 6.1 Wm^{-1} K^{-1}, which was more than double that of the SGCAS. Thermal conductivity analysis showed that all of the DCAS examined had good thermal conductivity. The average pore size of composite DCAS decreased slightly due to the complex nature of the LiCl that formed during the deposit on the silica surface. The dynamic sorption quantities and sorption rate coefficients of composite DCAS were greater than those of SGCAS. Composite DCAS had sorption rate coefficients that were approximately 1 time greater than SGCAS. This is because immersed LiCl particles blocked some of the silica’s narrow pores. The SEM image shows that, as the mass fraction of LiCl increased, the LiCl salt gradually occupied the microporosity of the silica pellet and was partially deposited on the grain's external surface. Moisture sorption isotherms showed that composite DCAS had a higher adsorption capacity than SGCAS, with a 20 to 30% higher water uptake. The outlet air humidity ratio of the DCHS reached a minimum of 10.23 g kg^{-1}, and the dehumidification capacity was 0.117 kg h^{-1} when the input electrical voltage was kept at 9 V. Furthermore, SG-L40-DCHS removed more moisture from the process air, which was approximately 1 time greater than SG-L0-DCHS.

Thermoelectric dehumidifier (TED) without and with composite desiccant coated heat sink

The cooling capacity increased as the electrical voltage increased and reached its maximum value of 100.78 W at 12 V. The COP varied between 1.18 and 0.79 depending on the voltage applied to the TEMs, ranging from 3 to 12 V. Additionally, as the electric voltage increased, the exergy increased. Low exergy resources should match the TEC system's low exergy demand. The operating parameters employed in this study were 9 V of electrical voltage applied to the TEMs and a cold-side air mass flow of 0.04 kg s^{-1}. The cooling capacity is 63.31 W with a coefficient of performance of 0.80 and a cold air temperature of 25.55 ^{o}C. The outlet air humidity ratio at 9 V reached 11.13 g kg^{-1} for TED and 9.86 g kg^{-1} for TED-CD. The dehumidification capacity of the TED-CD was higher than that of the TED at all the electrical voltages supplied to the TEMs (34.44%).

5.2 Recommendations for future research

1. Thermoelectric module service life and composite desiccant cracking during use are being investigated. Because the system has to switch from hot to cold, every hour.

2. Associated with the TED system, a combination of energy-saving air-conditioning system to achieve thermal comfort should be established.

3. The possibility of using a solar cell to drive the TED system is an interesting topic for further development.

REFERENCES

1. Shehadi M. Review of humidity control technologies in buildings. Journal of Building Engineering. 2018;19:539-51.

2. Shaikh PHN, Nursyarizal Bin Mohd & Nallagownden, Perumal & Elamvazuthi, Irraivan & Ibrahim, Taib. A review on optimized control systems for building energy and comfort management of smart sustainable buildings. Renewable and Sustainable Energy Reviews. 2014;34(C):409-29.

3. Okaeme CC, SM, JTW. A Comfort Zone Set-Based Approach for Coupled Temperature and

Humidity Control in Buildings. 2016 IEEE Int Conf Autom Sci Eng. 2016:456–61.

4. Cabrera P, Julià-Serdà G, de Castro FR, Caminero J, Barber D, Carrillo T. Reduction of house dust mite allergens after dehumidifier use. Journal of Allergy and Clinical Immunology. 1995;95(2):635-6.

5. Rafique MMG, P. & Bahaidarah, Haitham M.S. Liquid desiccant materials and dehumidifiers – A review. Renewable and Sustainable Energy Reviews. 2016;56(C):179-95.

6. Salikandi M, Ranjbar B, Shirkhan E, Shanmuga Priya S, Thirunavukkarasu I, Sudhakar K. Recent trends in liquid desiccant materials and cooling systems: Application, performance and regeneration characteristics. Journal of Building Engineering. 2021;33:101579.

7. Kim H, Rao SR, Kapustin EA, Zhao L, Yang S, Yaghi OM, et al. Adsorption-based atmospheric water harvesting device for arid climates. Nature Communications. 2018;9(1):1191.

8. Salek F, Moghaddam AN, Naserian MM. Thermodynamic analysis and improvement of a novel solar driven atmospheric water generator. Energy Conversion and Management. 2018;161:104-11.

9. Yang B, Yuan W, Gao F, Guo B. A review of membrane-based air dehumidification. Indoor and Built Environment. 2013;24(1):11-26.

10. Mohammad AT, Mat SB, Sulaiman MY, Sopian K, Al-abidi AA. Survey of liquid desiccant dehumidification system based on integrated vapor compression technology for building applications. Energy and Buildings. 2013;62:1-14.

11. Jani DB, Mishra M, Sahoo PK. A critical review on application of solar energy

as renewable regeneration heat source in solid desiccant – vapor compression hybrid cooling system. Journal of Building Engineering. 2018;18:107-24.

12. Rahman SMA, Hachicha AA, Ghenai C, Saidur R, Said Z. Performance and life cycle analysis of a novel portable solar thermoelectric refrigerator. Case Studies in Thermal Engineering. 2020;19:100599.

13. Zhao D, Tan G. A review of thermoelectric cooling: Materials, modeling and applications. Applied Thermal Engineering. 2014;66(1-2):15-24.

14. MohanKumar PJB, V.; Subramanian, A.; Bandla, A.; Thakor, N.; Ramakrishna, S.; Wei, H. Thermoelectric Materials—Strategies for Improving Device Performance and Its Medical Applications. Preprints. 2020:2020110090.

15. Dia Milani AA, Anthony Vassallo, Matteo Chiesa, Dhia Al Bakri. Evaluation of using thermoelectric coolers in a dehumidification system togenerate freshwater from ambient air. Chemical Engineering Science. 2011;66:2491-501.

16. Shourideh AH, Bou Ajram W, Al Lami J, Haggag S, Mansouri A. A comprehensive study of an atmospheric water generator using Peltier effect. Thermal Science and Engineering Progress. 2018;6:14-26.

17. dos Santos SM, Silva JFF, dos Santos GC, de Macedo PMT, Gavazza S. Integrating conventional and green roofs for mitigating thermal discomfort and water scarcity in urban areas. Journal of Cleaner Production. 2019;219:639-48.

18. Cerro C, editor Developing solutions for dealing with water and food scarcity: Atmospheric water generator and urban farm tower. 2018 Advances in Science and Engineering Technology International Conferences (ASET); 2018 6 Feb.-5 April 2018.

19. Yao H, Zhang P, Huang Y, Cheng H, Li C, Qu L. Highly Efficient Clean Water Production from Contaminated Air with a Wide Humidity Range. Advanced Materials. 2020;32(6):1905875.

20. Bagheri F. Performance investigation of atmospheric water harvesting systems. Water Resources and Industry. 2018;20:23-8.

21. Xi H, Luo L, Fraisse G. Development and applications of solar-based thermoelectric technologies. Renewable and Sustainable Energy Reviews. 2007;11(5):923-36.

22. Hermes CJL, Barbosa JR. Thermodynamic comparison of Peltier, Stirling, and vapor compression portable coolers. Applied Energy. 2012;91(1):51-8.

23. Pourkiaei SM, Ahmadi MH, Sadeghzadeh M, Moosavi S, Pourfayaz F, Chen L, et al. Thermoelectric cooler and thermoelectric generator devices: A review of present

and potential applications, modeling and materials. Energy. 2019;186:115849.

24. Riffat SB, Ma X. Thermoelectrics: a review of present and potential applications. Applied Thermal Engineering. 2003;23(8):913-35.

25. Sarbu I, Dorca A. A comprehensive review of solar thermoelectric cooling systems. International Journal of Energy Research. 2018;42(2):395-415.

26. Siddique ARM, Mahmud S, Heyst BV. A review of the state of the science on wearable thermoelectric power generators (TEGs) and their existing challenges. Renewable and Sustainable Energy Reviews. 2017;73:730-44.

27. Gao HB, Huang GH, Li HJ, Qu ZG, Zhang YJ. Development of stove-powered thermoelectric generators: A review. Applied Thermal Engineering. 2016;96:297-310.

28. Champier D. Thermoelectric generators: A review of applications. Energy Conversion and Management. 2017;140:167-81.

29. Omidi B, Rahbar N, Kargarsharifabad H, Rashidi S. Combination of a solar collector and thermoelectric cooling modules in a humidification–dehumidification desalination system-experimental investigation with energy, exergy, exergoeconomic and environmental analysis. Energy Conversion and Management. 2020;225:113440.

30. Irshad K, Almalawi A, Habib K, Zahir MH, Ali A, Islam S, et al. Experimental Study of a Thermoelectric Air Duct Dehumidification System for Tropical Climate. Heat Transfer Engineering. 2021;42(13-14):1159-71.

31. Tikhomirov DA, Trunov SS, Kuzmichev AV, Rastimeshin SA, Shepovalova OV. Energy-efficient thermoelectric unit for microclimate control on cattlebreeding premises. Energy Reports. 2020;6:293-305.

32. Koc C, Koc AB, Gok FC, Duran H. Sustainable Water Harvesting from the Atmosphere Using Solar-Powered Thermoelectric Modules. Pol J Environ Stud. 2020;29(2):1197-204.

33. He W, Yu P, Hu Z, Lv S, Qin M, Yu C. Experimental Study and Performance Analysis of a Portable Atmospheric Water Generator. Energies. 2020;13(1).

34. Kadhim TJ, Abbas AK, Kadhim HJ. Experimental study of atmospheric water collection powered by solar energy using the Peltier effect. IOP Conference Series: Materials Science and Engineering. 2020;671(1):012155.

35. Lertsatitthanakorn C, Rakkwamsuk P, Paromupatham P, Sathapornprasath K, Soponronnarit S. Experimental and Theoretical Study of a Thermoelectric Dehumidification System. Journal of Electronic Materials. 2020;49(5):2968-74.

36. Patel V, Patel R, Patel J. Theoretical and experimental investigation of bubble

column humidification and thermoelectric cooler dehumidification water desalination system. International Journal of Energy Research. 2020;44(2):890-901.

37. Im D-H, Kwon H-C, Kim K-J, Kim K-H. Study on the Design of a New Heatsink Cooling System for Thermoelectric Dehumidifier. International Journal of Precision Engineering and Manufacturing. 2020;21(1):75-80.

38. Nhut LM, Linh DTT, editors. Effects of the Relative Humidity on the Performance of Thermoelectric Freshwater Generator using Solar Power Source. 2020 5th International Conference on Green Technology and Sustainable Development (GTSD); 2020 27-28 Nov. 2020.

39. T-H L. The Analysis of the Effects of Design Parameters on the Energy Efficiency and Performance of TEM Dehumidifiers. ransactions of the Korea Society of Geothermal Energy Engineers [Internet]. 2020;16(3):1-7.

40. Atuonwu JC, Jin X, van Straten G, Deventer Antonius HCv, van Boxtel JB. Reducing energy consumption in food drying: Opportunities in desiccant adsorption and other dehumidification strategies. Procedia Food Science. 2011;1:1799-805.

41. Huang S-M, Zhang L-Z. Researches and trends in membrane-based liquid desiccant air dehumidification. Renewable and Sustainable Energy Reviews. 2013;28:425-40.

42. Jia CX, Dai YJ, Wu JY, Wang RZ. Use of compound desiccant to develop high performance desiccant cooling system. International Journal of Refrigeration. 2007;30(2):345-53.

43. Aristov YI, Restuccia G, Cacciola G, Parmon VN. A family of new working materials for solid sorption air conditioning systems. Applied Thermal Engineering. 2002;22(2):191-204.

44. Cortés FB, Chejne F, Carrasco-Marín F, Pérez-Cadenas AF, Moreno-Castilla C. Water sorption on silica- and zeolite-supported hygroscopic salts for cooling system applications. Energy Conversion and Management. 2012;53(1):219-23.

45. Li X, Li H, Huo S, Li Z. Dynamics and isotherms of water vapor sorption on mesoporous silica gels modified by different salts. Kinetics and Catalysis. 2010;51(5):754-61.

46. Simonova IA, Freni A, Restuccia G, Aristov YI. Water sorption on composite “silica modified by calcium nitrate”. Microporous and Mesoporous Materials. 2009;122(1):223-8.

47. Aristov YI, Sapienza A, Ovoshchnikov DS, Freni A, Restuccia G. Reallocation of adsorption and desorption times for optimisation of cooling cycles. International

Journal of Refrigeration. 2012;35(3):525-31.

48. Ge TS, Li Y, Wang RZ, Dai YJ. Experimental study on a two-stage rotary desiccant cooling system. International Journal of Refrigeration. 2009;32(3):498-508.

49. Jeong J, Yamaguchi S, Saito K, Kawai S. Performance analysis of desiccant dehumidification systems driven by low-grade heat source. International Journal of Refrigeration. 2011;34(4):928-45.

50. Hu LM, Ge TS, Jiang Y, Wang RZ. Performance study on composite desiccant material coated fin-tube heat exchangers. International Journal of Heat and Mass Transfer. 2015;90:109-20.

51. Chua KJ. Heat and mass transfer of composite desiccants for energy efficient air dehumidification: Modelling and experiment. Applied Thermal Engineering. 2015:703-16.

52. Shaw EW. Thermal Comfort: analysis and applications in environmental engineering, by P. O. Fanger. 244 pp. DANISH TECHNICAL PRESS. Copenhagen, Denmark, 1970. Danish Kr. 76, 50. The Journal of the Royal Society for the Promotion of Health. 1972;92:164 -

53. Moderate thermal environments — Determination of the PMV and PPD indices and specification of the conditions for thermal comfort [Internet]. International Organization for Standardization. 1994. Available from: https://infostore.saiglobal.com/en-us/Standards/ISO-7730-1994-584774_SAIG_ISO_ISO_1339102/.

54. American Society of Heating RaA-CE. 1992 ASHRAE handbook

heating, ventilating, and air-conditioning systems and equipmen: Atlanta, GA. : ASHRAE; 1992.

55. American Society of Heating RaA-CE. 2001 ASHRAE handbook : fundamentals.: Atlanta, GA. : ASHRAE; 2001.

56. Fountain M, Huizenga C. A thermal comfort prediction tool. Indoor Environmental Quality (IEQ). 1996;38(9).

57. Kumar S, Singh MK, Mathur A, Mathur S, Mathur J. Thermal performance and comfort potential estimation in low-rise high thermal mass naturally ventilated office buildings in India: An experimental study. Journal of Building Engineering. 2018;20:569-84.

58. Zhao Z, Houchati M, Beitelmal A. An Energy Efficiency Assessment of the Thermal Comfort in an Office building. Energy Procedia. 2017;134:885-93.

59. Maykot JK, Rupp RF, Ghisi E. Assessment of gender on requirements for thermal comfort in office buildings located in the Brazilian humid subtropical climate. Energy and Buildings. 2018;158:1170-83.

60. Antoniadou P, Papadopoulos AM. Occupants’ thermal comfort: State of the art and the prospects of personalized assessment in office buildings. Energy and Buildings. 2017;153:136-49.

61. Cho H-J, Jeong J-W. Evaluation of thermal comfort in an office building served by a liquid desiccant-assisted evaporative cooling air-conditioning system. Energy and Buildings. 2018;172:361-70.

62. He Y, Li N, Zhang W, Peng J. Overall and local thermal sensation & comfort in air-conditioned dormitory with hot-humid climate. Building and Environment. 2016;101:102-9.

63. Rupp RF, Kim J, de Dear R, Ghisi E. Associations of occupant demographics, thermal history and obesity variables with their thermal comfort in air-conditioned and mixed-mode ventilation office buildings. Building and Environment. 2018;135:1-9.

64. Teli D, Jentsch MF, James PAB. The role of a building's thermal properties on pupils' thermal comfort in junior school classrooms as determined in field studies. Building and Environment. 2014;82:640-54.

65. Wong NH, Tan E, Gabriela O, Jusuf SK. Indoor Thermal Comfort Assessment of Industrial Buildings in Singapore. Procedia Engineering. 2016;169:158-65.

66. Pinto NdM, Xavier AAdP, Hatakeyama K. Thermal Comfort in Industrial Environment: Conditions and Parameters. Procedia Manufacturing. 2015;3:4999-5006.

67. Mohamed Kamar H, Kamsah NB, Ghaleb FA, Idrus Alhamid M. Enhancement of thermal comfort in a large space building. Alexandria Engineering Journal. 2019;58(1):49-65.

68. Aghniaey S, Lawrence TM. The impact of increased cooling setpoint temperature during demand response events on occupant thermal comfort in commercial buildings: A review. Energy and Buildings. 2018;173:19-27.

69. Putra JCP. A Study of Thermal Comfort and Occupant Satisfaction in Office Room. Procedia Engineering. 2017;170:240-7.

70. Soebarto V, Bennetts H. Thermal comfort and occupant responses during summer in a low to middle income housing development in South Australia. Building and Environment. 2014;75:19-29.

71. Indraganti M, Boussaa D. Comfort temperature and occupant adaptive behavior

in offices in Qatar during summer. Energy and Buildings. 2017;150:23-36.

72. López-Pérez LA, Flores-Prieto JJ, Ríos-Rojas C. Adaptive thermal comfort model for educational buildings in a hot-humid climate. Building and Environment. 2019;150:181-94.

73. Pomfret L, Hashemi A. Thermal Comfort in Zero Energy Buildings. Energy Procedia. 2017;134:825-34.

74. Ribé O, Ruiz R, Quera M, Cadafalch J. Analysis of the sensible and total ventilation energy recovery potential in different climate conditions. Application to the Spanish case. Applied Thermal Engineering. 2019;149:854-61.

75. Pantelic J, Rysanek A, Miller C, Peng Y, Teitelbaum E, Meggers F, et al. Comparing the indoor environmental quality of a displacement ventilation and passive chilled beam application to conventional air-conditioning in the Tropics. Building and Environment. 2018;130:128-42.

76. Perez-Lombard L, Ortiz J, Maestre IR. The map of energy flow in HVAC systems. Applied Energy. 2011;88(12):5020-31.

77. Murray P, Rysanek AM, Pantelic J, Mast M, Schlueter A. On Decentralized Air-conditioning for Hot and Humid Climates: Performance Characterization of a Small Capacity Dedicated Outdoor Air System with Built-in Sensible and Latent Energy Recovery Wheels. Energy Procedia. 2015;78:3471-6.

78. Anjomshoaa A, Salmanzadeh M. Finding a criterion for the pressure loss of energy recovery exchangers in HVAC systems from thermodynamic and economic points of view. Energy and Buildings. 2018;166:426-37.

79. Yang Q, Zhu J, Xu X, Lu J. Simultaneous control of indoor air temperature and humidity for a chilled water based air conditioning system using neural networks. Energy and Buildings. 2016;110:159-69.

80. Busch JF. A tale of two populations: thermal comfort in air-conditioned and naturally ventilated offices in Thailand. Energy and Buildings. 1992;18(3):235-49.

81. Kitchai Jitkhajornwanich ACP, Albert Malama, Steve Sharples. Thermal Comfort in Transitional Spaces in the Cool Season of Bangkok. ASHRAE Transactions. 1998;104:1181-93.

82. Khedari J, Yamtraipat N, Pratintong N, Hirunlabh J. Thailand ventilation comfort chart. Energy and Buildings. 2000;32(3):245-9.

83. Srivajana W. Effects of air velocity on thermal comfort in hot and humid climates. Thammasat Int J Sc TEch. 2003;8:45-54.

84. Tantasavasdi C, Srebric J, Chen Q. Natural ventilation design for houses in Thailand. Energy and Buildings. 2001;33(8):815-24.

85. American Society of Heating RaA-CE. 1993 ASHRAE Handbook:Fundamentals

Atlanta, GA. : ASHRAE; 1993.

86. Yin Y, Zhang X, Wang G, Luo L. Experimental study on a new internally cooled/heated dehumidifier/regenerator of liquid desiccant systems. International Journal of Refrigeration. 2008;31(5):857-66.

87. Arora CP. Refrigeration and Air Conditioning: Tata McGraw-Hill Education; 2000.

88. Khan AY. Cooling and dehumidification performance analysis of internally-cooled liquid desiccant absorbers. Applied Thermal Engineering. 1998;18(5):265-81.

89. Davanagere BS, Sherif SA, Goswami DY. A feasibility study of a solar desiccant air-conditioning system—Part II: Transient simulation and economics. International Journal of Energy Research. 1999;23(2):103-16.

90. Warwicker B. Desiccant materials for moisture control in buildings. Materials for Energy Efficiency and Thermal Comfort in Buildings2010. 365-83 p.

91. Sarbu I, Sebarchievici C. Review of solar refrigeration and cooling systems. Energy and Buildings. 2013;67:286-97.

92. Liu XH, Jiang Y, Chang XM, Yi XQ. Experimental investigation of the heat and mass transfer between air and liquid desiccant in a cross-flow regenerator. Renewable Energy. 2007;32(10):1623-36.

93. Abdalla KN, Ahmed AM. Experimental Investigation of Moisture Removal Rate and Dehumidification Effectiveness of an Internally Cooled Liquid Desiccant Air Dehumidifier. UNIVERSITY of KHARTOUM ENGINEERING JOURNAL (UofKEJ). 2011;1(1):25-31.

94. Jia CX, Dai YJ, Wu JY, Wang RZ. Experimental comparison of two honeycombed desiccant wheels fabricated with silica gel and composite desiccant material. Energy Conversion and Management. 2006;47(15):2523-34.

95. Ge TS, Dai YJ, Wang RZ, Peng ZZ. Experimental comparison and analysis on silica gel and polymer coated fin-tube heat exchangers. Energy. 2010;35(7):2893-900.

96. Ge TS, Dai YJ, Wang RZ. Performance study of silica gel coated fin-tube heat exchanger cooling system based on a developed mathematical model. Energy Conversion and Management. 2011;52(6):2329-38.

97. Ge TS, Dai YJ, Li Y, Wang RZ. Simulation investigation on solar powered desiccant coated heat exchanger cooling system. Applied Energy. 2012;93:532-40.

98. Zhao Y, Ge TS, Dai YJ, Wang RZ. Experimental investigation on a desiccant dehumidification unit using fin-tube heat exchanger with silica gel coating. Applied Thermal Engineering. 2014;63(1):52-8.

99. Jiang Y, Ge TS, Wang RZ, Hu LM. Experimental investigation and analysis of composite silica-gel coated fin-tube heat exchangers. International Journal of Refrigeration. 2015;51:169-79.

100. Techajunta S, Chirarattananon S, Exell RHB. Experiments in a solar simulator on solid desiccant regeneration and air dehumidification for air conditioning in a tropical humid climate. Renewable Energy. 1999;17(4):549-68.

101. Gandhidasan P, Al-Farayedhi AA, Al-Mubarak AA. Dehydration of natural gas using solid desiccants. Energy. 2001;26(9):855-68.

102. Hamed AM. Theoretical and experimental study on the transient adsorption characteristics of a vertical packed porous bed. Renewable Energy. 2002;27(4):525-41.

103. Hamed AM. Theoretical and experimental study on the transient adsorption characteristics of a vertical packed porous bed. Renewable Energy. 2002;27:525-41.

104. Awad MM, Ramzy K A, Hamed AM, Bekheit MM. Theoretical and experimental investigation on the radial flow desiccant dehumidification bed. Applied Thermal Engineering. 2008;28(1):75-85.

105. Ahmed MH, Kattab NM, Fouad M. Evaluation and optimization of solar desiccant wheel performance. Renewable Energy. 2005;30(3):305-25.

106. Hamed AM, Abd El Rahman WR, El-Emam SH. Experimental study of the transient adsorption/desorption characteristics of silica gel particles in fluidized bed. Energy. 2010;35(6):2468-83.

107. Rowe DM. CRC Handbook of Thermoelectrics: CRC Press; 1995.

108. Altenkirch E. Über den nutzeffekt der thermosäule. Physikalische Zeitschrift. 1909;10(560):12.

109. Twaha S, Zhu J, Yan Y, Li B. A comprehensive review of thermoelectric technology: Materials, applications, modelling and performance improvement. Renewable and Sustainable Energy Reviews. 2016;65:698-726.

110. Tritt TM. Thermoelectric Phenomena, Materials, and Applications. Annual Review of Materials Research. 2011;41(1):433-48.

111. Tsai H-L, Lin J-M. Model Building and Simulation of Thermoelectric Module Using Matlab/Simulink. Journal of Electronic Materials. 2010;39(9):2105-11.

112. Dubey N, Leclerc M. Conducting polymers: Efficient thermoelectric materials. Journal of Polymer Science Part B: Polymer Physics. 2011;49(7):467-75.

113. A. F. Ioffe LSSb, E. K. Iordanishvili, T. S. Stavitskaya. Semiconductor Thermoelements and Thermoelectric Cooling. Physics Today. 1995;12(5):42.

114. Vián JG, Astrain D, Domínguez M. Numerical modelling and a design of a thermoelectric dehumidifier. Applied Thermal Engineering. 2002;22(4):407-22.

115. Udomsakdigool C, Hirunlabh J, Khedari J, Zeghmati B. Design Optimization of a New Hot Heat Sink with a Rectangular Fin Array for Thermoelectric Dehumidifiers. Heat Transfer Engineering. 2007;28(7):645-55.

116. Huajun W, Chengying Q, editors. Experimental study of operation performance of a low power thermoelectric cooling dehumidifier2010.

117. Atta RM. Solar Water Condensation Using Thermoelectric Coolers. International Journal of Water Resources and Arid Environments. 2011;1(2):142-5.

118. Jradi M, Ghaddar N, Ghali K. Experimental and theoretical study of an integrated thermoelectric–photovoltaic system for air dehumidification and fresh water production. International Journal of Energy Research. 2012;36(9):963-74.

119. Yıldırım C, Soylu SK, Atmaca İ, Solmuş İ. Experimental investigation of a portable desalination unit configured by a thermoelectric cooler. Energy Conversion and Management. 2014;85:140-5.

120. Joshi VP, Joshi VS, Kothari HA, Mahajan MD, Chaudhari MB, Sant KD. Experimental Investigations on a Portable Fresh Water Generator Using a Thermoelectric Cooler. Energy Procedia. 2017;109:161-6.

121. Liu S, He W, Hu D, Lv S, Chen D, Wu X, et al. Experimental analysis of a portable atmospheric water generator by thermoelectric cooling method. Energy Procedia. 2017;142:1609-14.

122. Yao Y, Sun Y, Sun D, Sang C, Sun M, Shen L, et al. Optimization design and experimental study of thermoelectric dehumidifier. Applied Thermal Engineering. 2017;123:820-9.

123. Tang J, Gong G, Su H, Wu F, Herman C. Performance evaluation of a novel method of frost prevention and retardation for air source heat pumps using the orthogonal experiment design method. Applied Energy. 2016;169:696-708.

124. Su L, Zhang J, Wang C, Zhang Y, Li Z, Song Y, et al. Identifying main factors

of capacity fading in lithium ion cells using orthogonal design of experiments. Applied Energy. 2016;163:201-10.

125. Amer M, Wang C-C. Review of defrosting methods. Renewable and Sustainable Energy Reviews. 2017;73:53-74.

126. B.J. Li DL, L.J. Hua, Y.D. Tu, H.M. Hu, R.Z. Wang. Design and experimental study of a desiccant thermoelectric dehumidifier. 2017;1:1-5.

127. Uttasilp C, Patcharaprakiti N, Somsak T, Thongpron J. Optimal solar energy on thermoelectric cooler of water generator in case study on flood crisis. Japanese Journal of Applied Physics. 2018;57(8S3):08RH5.

128. Kim J, Park K, Lee D-G, Chang YS, Kim H-Y. Optimal cold sink temperature for thermoelectric dehumidifiers. Journal of Mechanical Science and Technology. 2018;32(2):885-95.

129. Chen K, Gwilliam SB. An analysis of the heat transfer rate and efficiency of TE (thermoelectric) cooling systems. International Journal of Energy Research. 1996;20(5):399-417.

130. S. B. Riffat, Ma X. Improving the coefficient of performance of thermoelectric

cooling systems: a review. INTERNATIONAL JOURNAL OF ENERGY RESEARCH. 2004;28:753-68.

131. Kundu B. Approximate analytic solution for performances of wet fins with a polynomial relationship between humidity ratio and temperature. International Journal of Thermal Sciences. 2009;48(11):2108-18.

132. Rakkwamsuk P, Paromupatham P, Sathapornprasath K, Lertsatitthanakorn C, Soponronnarit S. An experimental investigation on the performance of a thermoelectric dehumidification system. Journal of Mechanical Engineering and Sciences. 2018;12(4):4117-26.

133. Sharqawy MH, Zubair SM. Efficiency and Optimization of a Straight Rectangular Fin with Combined Heat and Mass Transfer. Heat Transfer Engineering. 2008;29(12):1018-26.

134. Kiliç A, Onat K. The optimum shape for converting rectangular fins when condensation occurs. Wärme - und Stoffübertragung. 1981;15(2):125-33.

135. Coney JER, Kazeminejad H, Sheppard CGW. Dehumidification of Air on a Vertical Rectangular Fin: A Numerical Study. Proceedings of the Institution of Mechanical Engineers, Part C: Journal of Mechanical Engineering Science. 1989;203:165 - 75.

136. Chanchira Channoy SM, Chantana Punlek, Surapong Chirarattananon. Preparation and Characterization of Silica Gel from Bagasse Ash. Advanced Materials Research. 2018;1145:44-8.

137. Ribeiro DV, Morelli MR. Effect of Calcination Temperature on the Pozzolanic Activity of Brazilian Sugar Cane Bagasse Ash (SCBA). Materials Research. 2014;17(4):974-81.

138. Ma X, Zhou B, Gao W, Qu Y, Wang L, Wang Z, et al. A recyclable method for production of pure silica from rice hull ash. Powder Technology. 2012;217:497-501.

139. Zheng X, Ge TS, Jiang Y, Wang RZ. Experimental study on silica gel-LiCl composite desiccants for desiccant coated heat exchanger. International Journal of Refrigeration. 2015;51:24-32.

140. Glueckauf E. Theory of chromatography. Part 10N Formulæ for diffusion into spheres and their application to chromatography. Transactions of The Faraday Society. 1955;51:1540-51.

141. Brunauer S, Emmett PH, Teller E. ADSORPTION OF GASES IN MULTIMOLECULAR LAYERS. Journal of the American Chemical Society. 1938;60:309-19.

142. Timmermann EO. Multilayer sorption parameters: BET or GAB values? Colloids and Surfaces A: Physicochemical and Engineering Aspects. 2003;220(1):235-60.

143. Carter BP, Galloway MT, Campbell GS, Carter AH. The critical water activity from dynamic dewpoint isotherms as an indicator of crispness in low moisture cookies. Journal of Food Measurement and Characterization. 2015;9(3):463-70.

144. Arthur E, Tuller M, Moldrup P, de Jonge LW. Evaluation of theoretical and empirical water vapor sorption isotherm models for soils. Water Resources Research. 2016;52(1):190-205.

145. Webb RL, Gilley, M. D., Zarnescu, V. . Advanced heat exchange technology for thermoelectric cooling devices. Journal of Electronic PackagingJournal of Electronic Packaging. 1998;120(1):98.

146. Rowe DM, Min G. Design theory of thermoelectric modules for electrical power generation. IEE Proceedings - Science, Measurement and Technology [Internet]. 1996; 143(6):[351-6 pp.]. Available from: https://digital-library.theiet.org/content/journals/10.1049/ip-smt_19960714.

147. Ioffe AF, Stil bans LS, Iordanishvili EK, Stavitskaya TS, Gelbtuch A, Vineyard GH, editors. Semiconductor Thermoelements and Thermoelectric Cooling1957.

148. Goldsmid HJ. Electronic Refrigeration: Pion Limited; 1986.

149. Knight RW, Goodling JS, Hall DJ. Optimal Thermal Design of Forced Convection Heat Sinks-Analytical. Journal of Electronic Packaging. 1991;113(3):313-21.

150. P.G.. BRJaL. Thermoelectric Power Generator Design and Selection from TE Cooling Module Specifications. 16th International Conference on Thermoelectrics1997. p. 551-4.

151. Incropera FPD, D.P. Fundamentals of Heat and Mass Transfer. New York: Jonh Wiley & Son; 1990.

152. Zhang HY, Mui YC, Tarin M. Analysis of thermoelectric cooler performance for high power electronic packages. Applied Thermal Engineering. 2010;30(6):561-8.

153. Chein R, Huang G. Thermoelectric cooler application in electronic cooling. Applied Thermal Engineering. 2004;24(14):2207-17.

154. Karami Rad M, Rezania A, Omid M, Rajabipour A, Rosendahl L. Study on material properties effect for maximization of thermoelectric power generation. Renewable Energy. 2019;138:236-42.

155. Nada SA, Elattar HF, Fouda A. Experimental study for hybrid humidification–dehumidification water desalination and air conditioning system. Desalination. 2015;363:112-25.

156. Riffat SB, Ma X. Optimum selection (design) of thermoelectric modules for large capacity heat pump applications. International Journal of Energy Research. 2004;28(14):1231-42.

157. Bejan A. Entropy generation minimization: The new thermodynamics of finite-size devices and finite-time processes. Journal of Applied Physics. 1996;79(3):1191-218.

158. Rowe DM, Min G. Evaluation of thermoelectric modules for power generation. Journal of Power Sources. 1998;73(2):193-8.

159. He W, Zhou J, Chen C, Ji J. Experimental study and performance analysis of a thermoelectric cooling and heating system driven by a photovoltaic/thermal system in summer and winter operation modes. Energy Conversion and Management. 2014;84:41-9.

160. Intani K, Latif S, Kabir AKMR, Müller J. Effect of self-purging pyrolysis on yield of biochar from maize cobs, husks and leaves. Bioresource Technology. 2016;218:541-51.

161. RK I. colloid and surface properties and biochemistry. New York: Wiley; 1979.

162. Pathak U, Kumari S, Kumar A, Mandal T. Process parametric optimization toward augmentation of silica yield using Taguchi technique and artificial neural network approach. Energy, Ecology and Environment. 2020;5(4):294-312.

163. Della VP, Kühn I, Hotza D. Rice husk ash as an alternate source for active silica production. Materials Letters. 2002;57(4):818-21.

164. Kalapathy U, Proctor A, Shultz J. A simple method for production of pure silica from rice hull ash. Bioresource Technology. 2000;73(3):257-62.

165. Muljani S, Setyawan H, Wibawa G, Altway A. A facile method for the production of high-surface-area mesoporous silica gels from geothermal sludge. Advanced Powder Technology. 2014;25(5):1593-9.

166. ALOthman ZA. A Review: Fundamental Aspects of Silicate Mesoporous Materials. Materials. 2012;5(12):2874-902.

167. Lowell S, Shields JE, Thomas MA, Thommes M. Characterization of Porous Solids and Powders: Surface Area, Pore Size and Density: Springer, Dordrecht; 2000. 350 p.

168. Galarneau A, Villemot F, Rodriguez J, Fajula F, Coasne B. Validity of the t-plot method to assess microporosity in hierarchical micro/mesoporous materials. Langmuir. 2014;30(44):13266-74.

169. Hegde ND, Venkateswara Rao A. Organic modification of TEOS based silica aerogels using hexadecyltrimethoxysilane as a hydrophobic reagent. Applied Surface Science. 2006;253(3):1566-72.

170. Alba MD, Luan Z, Klinowski J. Titanosilicate Mesoporous Molecular Sieve MCM-41: Synthesis and Characterization. The Journal of Physical Chemistry. 1996;100(6):2178-82.

171. Vasconcelos RFSLL. Preparation of silica by sol-gel method using formamide. Materials Research 2001;4(3).

172. Chen Q, Li X, Zhang Y, Qian Y. Ferroelectric Properties of Porous Silicon. Advanced Materials. 2002;14(2):134-7.

173. Zhang YN, Wang RZ, Li TX. Thermochemical characterizations of high-stable activated alumina/LiCl composites with multistage sorption process for thermal storage. Energy. 2018;156:240-9.

174. Gordeeva LG, Glaznev IS, Savchenko EV, Malakhov VV, Aristov YI. Impact of phase composition on water adsorption on inorganic hybrids “salt/silica”. Journal of

Colloid and Interface Science. 2006;301(2):685-91.

175. Gong LX, Wang RZ, Xia ZZ, Chen CJ. Adsorption Equilibrium of Water on a Composite Adsorbent Employing Lithium Chloride in Silica Gel. Journal of Chemical & Engineering Data. 2010;55(8):2920-3.

176. Zheng X, Ge TS, Wang RZ, Hu LM. Performance study of composite silica gels with different pore sizes and different impregnating hygroscopic salts. Chemical Engineering Science. 2014;120:1-9.

177. Yu N, Wang RZ, Lu ZS, Wang LW. Development and characterization of silica gel–LiCl composite sorbents for thermal energy storage. Chemical Engineering Science. 2014;111:73-84.

178. Frazzica A, Brancato V, Caprì A, Cannilla C, Gordeeva LG, Aristov YI. Development of “salt in porous matrix” composites based on LiCl for sorption thermal energy storage. Energy. 2020;208:118338.

179. Rouquerol J, Avnir D, Fairbridge CW, Everett DH, Haynes JM, Pernicone N, et al. Recommendations for the characterization of porous solids (Technical Report). Pure and Applied Chemistry. 1994;66(8):1739-58.

180. Kruk M, Jaroniec M. Gas adsorption characterization of ordered organic-inorganic nanocomposite materials. Chemistry of Materials. 2001;13:3169-83.

181. Huo Q-s, Margolese, I. D, Stucky GD. Surfactant Control of Phases in the Synthesis of Mesoporous Silica-Based Materials. Chemistry of Materials. 1996;8:1147-60.

182. Kruk M, Jaroniec M, Sayari A. Application of Large Pore MCM-41 Molecular Sieves To Improve Pore Size Analysis Using Nitrogen Adsorption Measurements. Langmuir. 1997;13(23):6267-73.

183. Zheng X, Wang R. Microstructure and sorption performance of consolidated composites impregnated with LiCl. International Journal of Refrigeration. 2019;98:452-8.

184. Oulkadi D, Desobry S, Mustin C, Desobry-Banon S. Water sorption in hybrid silica gels containing colloidal nontronite. Journal of Sol-Gel Science and Technology. 2012;64(3):653-60.